AFOSR-TR-~~96~~ 97

0062

REPORT DOCUMENTATION PAGE

Public reporting burden for this collection of information is estimated to average 1 hour per response, including gathering and maintaining the data needed, and completing and reviewing the collection of information. Send collection of information, including suggestions for reducing this burden, to Washington Headquarters Services, Davis Highway, Suite 1204, Arlington, VA 22202-4302, and to the Office of Management and Budget, Paperwork Reduction Project (0704-0188), Washington, DC 20503.

1. AGENCY USE ONLY *(Leave blank)*

2. REPORT DATE

3. REPORT TYPE AND DATES COVERED
FINAL REPORT 01 Mar 93 - 30 Jun 96

4. TITLE AND SUBTITLE
FABRY-PEROT MODULATORS AS WAVELENGTH SENSITIVE, SWITCHABLE DETECTOR ARRAYS AND THEIR INTEGRATION INTO SMART PIXELS

5. FUNDING NUMBERS
61102F
2305/DS

6. AUTHOR(S)
Professor Coldren

7. PERFORMING ORGANIZATION NAME(S) AND ADDRESS(ES)
Dept of Materials and Electricla and Computer Engineering
University of California, Santa Barbara
Santa Barbara, CA 93106-9560

8. PERFORMING ORGANIZATION REPORT NUMBER

9. SPONSORING/MONITORING AGENCY NAME(S) AND ADDRESS(ES)
AFOSR/NE
110 Duncan Avenue Suite B115
Bolling AFB DC 20332-8080

10. SPONSORING/MONITORING AGENCY REPORT NUMBER
F49620-93-1-0183

11. SUPPLEMENTARY NOTES

12a. DISTRIBUTION/AVAILABILITY STATEMENT
APPROVED FOR PUBLIC RELEASE: DISTRIBUTION UNLIMITED

12b. DISTRIBUTION CODE

The work of the past three years has focused on VCSSEL-based free-space interconnects which appear to offer significant advantages for smart pixel applications. Today's vertical cavity lasers (VCLs) are the choice for short distance optical links, computer interconnects, and smart pixels. Their low threshold currents, relatively low power consumption, and low operating vovltage, make them compatible with simple drive circuits. High modulation bandwidth can be achieved without additional pre-bias circuitry. VCLs with a record 3 dB bandwidth of 15.3 GHz at only 2.1 mA of bias current have been reported from UCSB. The small diameter devices have peak output powers suitable for optical interconnect applications. Much of the recent improvement can be attributed to the introduction of a thin dielectric aperture, formed by lateral wet oxidation of high Al content AlGaAs compounds, in the laser cavity. The aperture provides good lateral current confinement and reduced optical losses, resulting in more efficient, smaller size devices with very low threshold currents. s Another advantage of small diameter VCLs are their highly divergent beams. The beams reaching the back side of the substrate fill integrated microlens enabling high numerical aperture focusing or collimation into low diffraction beams. With these integrated omponents, coupling into fibers and collimation for frree-space systems can be realized with no external optics. We have developed a technology for fabrication of refractive microlens in 'GaAs and in InP for integration with VCLs and with detectors, respectively. We considered the application of VCLs in a free-space optical system to board-to-board interconnects that would provide a high speed, low power option to back plane data buses.

17. SEC... OF REPORT	**OF THIS PAGE**	**OF ABSTRACT**	**...ABSTRACT**
UNCLASSIFIED	UNCLASSIFIED	UNCLASSIFIED	

19970128 183

DTIC QUALITY INSPECTED 1

Title: VCSEL-based Free-Space Interconnects
Program name: Fabry-Perot Modulars as Wavelength Selective, Switchable Detector Arrays and Their Integration into Smart Pixels

AFOSR #F49620-93-1-0183 - FINAL REPORT
6/1/93 - 5/31/96
by

L.A. Coldren: Principal Investigator
A.C. Gossard and S.I. Long: Co-Principal Investigators
D.A. Louderback, E.M. Strzelecka
and B.J. Thibeault: Students
K. Bertilsson: Researcher

ECE Technical Report #96-26

Department of Electrical & Computer Engineering

University of California at Santa Barbara

October 30, 1996

Table of Contents

A. INTRODUCTION

This is the final report for AFOSR # F496209310183. The program was initially focused on Fabry-Perot modulators for smart pixels. However, the work of the past three years has focused more on VCSEL-based free-space interconnects which appear to offer significant advantages for this application. Although record performance of asymmetric Fabry-Perot modulators (low voltage, low loss, high contrast and high speed) has been demonstrated [1-2], they place much higher demands on alignment and wavelength tolerances of a free-space optical system while they still require the presence of efficient, wavelength-controlled light sources. Our goal was to demonstrate and characterize free-space links using vertical-cavity surface-emitting laser (VCSEL or VCL) arrays, monolithically integrated with microlenses, together with photodiode arrays, also integrated with microlenses. Links with integrated microlenses are attractive since no additional external optics are required. Besides demonstrating high efficiency and high speed, it is also essential to determine the alignment tolerances and crosstalk levels for such free-space link arrays.

Vertical-cavity laser performance has improved dramatically in the last couple of years. Today's VCLs are indeed the choice for short distance optical links, computer interconnects, and smart pixels [3-7]. They are already being introduced commercially by a number of companies (e.g. Motorola, Honeywell, Hewlett-Packard). Their low threshold currents (< 300 μA for ~ 4 μm diameter devices), relatively low power consumption, and low operating voltage (< 2 V), make them compatible with simple drive circuits. High modulation bandwidth can be achieved without additional pre-bias circuitry. VCLs with a record 3 dB bandwidth of 15.3 GHz at only 2.1 mA of bias current have been reported from UCSB [8]. Arrays of our substrate-emitting VCLs can be easily flip-chip bonded onto drive circuits and/or transmission lines allowing us to fully utilize the available modulation bandwidth. The small diameter devices (~ 3 μm) have peak output powers of > 1 mW, suitable for optical interconnect applications. Much of the recent improvement can be attributed to the introduction of a thin dielectric aperture, formed by lateral wet oxidation of high Al content AlGaAs compounds, in the laser cavity. The aperture provides good lateral current confinement and reduced optical losses, resulting in more efficient, smaller size devices with very low threshold currents. Progress in growth and processing techniques [9], better theoretical understanding of the device and scaling of its properties with size [10], together with the introduction of the thin aperture [11], have all contributed to the improved performance of VCLs at UCSB.

Another advantage of small diameter VCLs are their highly divergent beams. The beams reaching the back side of the substrate fill integrated microlenses enabling high numerical aperture (NA) focusing or collimation into low diffraction beams. With these integrated components, coupling into fibers and collimation for free-space systems can be realized with no external optics.

We have developed a technology for fabrication of refractive microlenses in GaAs and in InP for integration with VCLs and with detectors, respectively [12]. These integrated components are used in a free-space optical link to study their performance. In an attempt to reduce channel spacing in interconnects, we have also fabricated wavelength-encoded VCL arrays with a pitch as small as 30 μm and investigated their thermal and optical properties.

We consider the application of VCLs in a free-space optical system for board-to-board interconnects that would provide a high speed, low power option to back plane data buses, as shown in Fig. A.1. The free-space optical link performance has been analyzed with respect to its mechanical and dimensional tolerances based on the scalar diffraction theory. The beams can be traced as they propagate from the laser to the detector through the substrates, microlenses and the free space in between the boards, resulting in evaluation of insertion losses and crosstalk. A computer program was written in ANSI C to simulate optical interconnects. This program is interfaced with HSPICE to allow analysis of the laser driver and/or receiver circuit including the laser and detector parasitics. Signals can be traced as they propagate through the link, providing information on the link and the influence of its components on the received signals.

The lensed components (VCLs and detectors) were used in an optical link to confirm the simulated results. Linear arrays of devices were flip-chip bonded and then wire bonded to connectorized boards with transmission lines, and mounted on translation stages for testing the mechanical tolerances. Beam shapes, alignment tolerances, and bit error rates at 3 Gbit/s of the optical link have been measured.

Sections B and C deal with VCL's CW and high speed characteristics. We show that much of the improvement is due to the introduction of a thin and/or tapered oxide aperture. **Section D** describes the technology for the formation of semiconductor refractive microlenses. Integration of microlenses on the back side of VCL and detector substrates results in components that are used for an optical link demonstration. We have also fabricated multiwavelength VCL arrays on a single wafer by controlled cavity length adjustment and MBE regrowth. Their characteristics and results of integration with microlenses for system applications are presented in **Section E**. Simulation results and driver circuit designs are presented in **Sections F, G, H**, and in the **Appendix**. Experimental setup of the optical link and its performance are presented in **Sections I and J**.

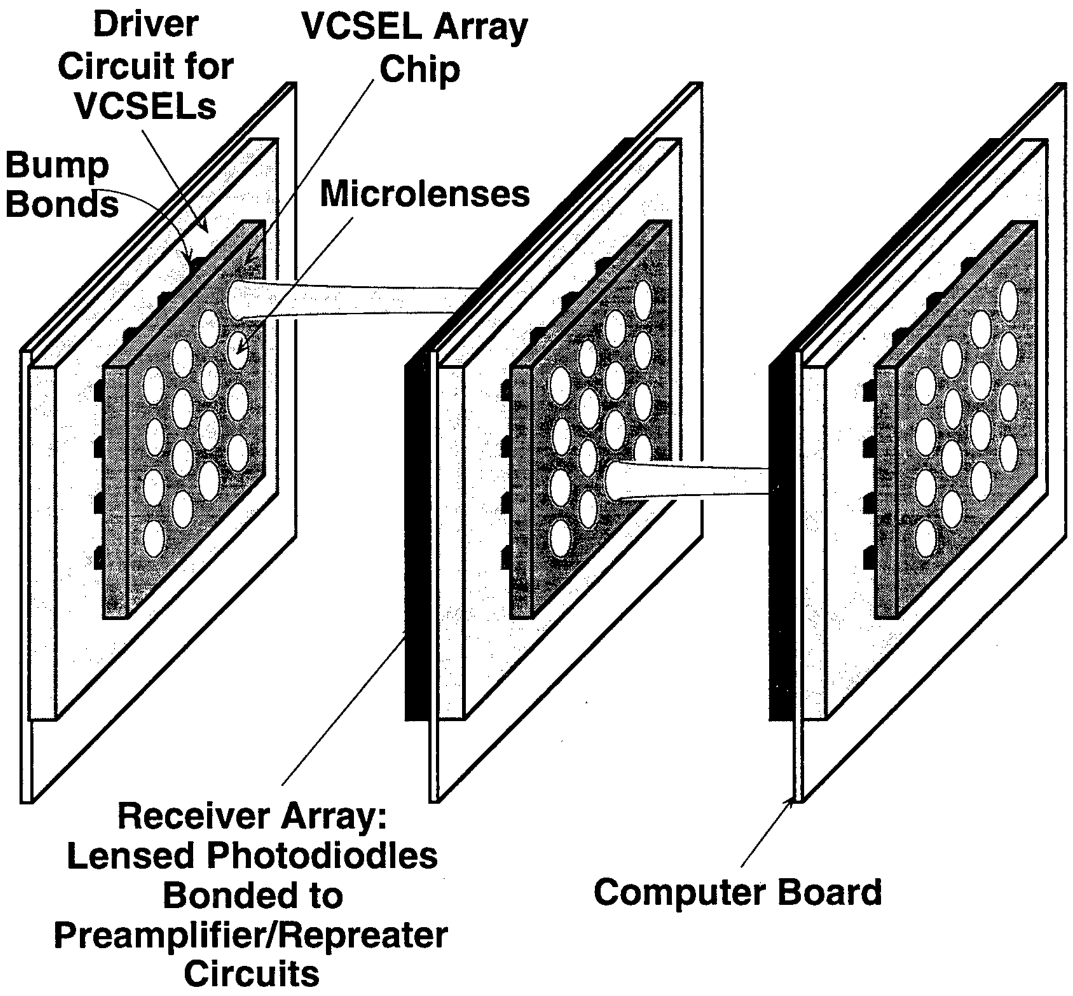

Figure A.1: Schematic of an array of free-space optical links for board-to-board interconnects.

REFERENCES TO SECTION A

1. C. C. Barron, C. J. Mahon, B. J. Thibeault, and L. A. Coldren, “Design, fabrication and characterization of high-speed asymmetric Fabry-Perot modulators for optical interconnect applications,” *Opt. and Quan. Electronics*, vol.25, pp.5885-5898 (1993)
2 C. C. Barron, C. J. Mahon, B. J. Thibeault, G. Wang, W. Jiang, L. A. Coldren, and J. E. Bowers, "Millimeter-wave asymmetric Fabry-Perot modulators," *IEEE J. of Quan. Electron.*, 31, pp.1484-1493 (1995)
3 E. M. Strzelecka, G. B. Thompson, G. D. Robinson, M. G. Peters, B. J. Thibeault, M. Mondry, V. Jayaraman, F. H. Peters, and L. A. Coldren, “Monolithic integration of refractive lenses with vertical cavity lasers and detectors for optical interconnections,” (Optoelectronic Packaging, San Jose, CA, USA, 1-2 Feb. 1996) SPIE, vol.2691, pp.43-53 (1996)

4. D. B. Schwartz, C. K. Y. Chun, B. M. Foley, D. H. Hartman, M. Lebby, H. C. Lee, Shieh Chan Long, S. M. Kuo, S. G. Shook, and B. Webb, "A low-cost high-performance optical interconnect," IEEE Trans. on Components, Packaging and Manufacturing, Part B: Advanced Packaging, 19, pp. 532-539 (1996)
5. M. Lebby, C. A. Gaw, W. Jiang, P. A. Kiely, Shieh Chan Long, P. R. Claisse, J. Ramdani, D. H. Hartman, D. B. Schwartz, and J. Grula, "Use of VCSEL arrays for parallel optical interconnects," (Fabrication, Testing, and Reliability of Semiconductor Lasers, San Jose, CA 1996) SPIE vol. 2683, pp. 81-91 (1996)
6. W. S. Ishak, K. H. Hahn, B. L. Booth, C. Muheller, A. A. J. Levi, and R. Craig, "Optical interconnects: The POLO project," (Optoelectronic Interconnects III, San Jose, CA 1995) SPIE vol. 2400, pp. 214-221 (1995)
7. J. A. Neff, "Thermal considerations of free-space optical interconnects using VCSEL-based smart pixel arrays," (Optoelectronic Packaging, San Jose, CA 1996) SPIE vol. 2691, pp. 150-161 (1996)
8. B.J. Thibeault, K. Bertilsson, E. R. Hegblom, P. D. Floyd, and L. A. Coldren, "High-Speed Characteristics of Low-Optical Loss Oxide-Apertured Vertical-Cavity Lasers," to be published in *IEEE Photon. Technol. Lett.*
9. J. Ko, M. J. Mondry, D. B. Young, S. Y. Hu, L. A. Coldren, and A. C. Gossard, "Threshold reduction by rapid thermal annealing in MBE-grown AlInGaAs multiquantum well lasers on GaAs," *Elec. Lett.*, 32, 351-352 (1996)
10. E. R. Hegblom, E.R.; D. I. Babic, D.I.; B. J. Thibeault, B.J.; and L. A. Coldren, "Estimation of scattering losses in dielectrically apertured vertical cavity lasers," *Appl. Phys. Lett.*, 25 vol.68, 1757-1759 (1996)
11. B. J. Thibeault, E. R. Hegblom, P. D. Floyd, R. Naone, Y. Akulova, and L. A. Coldren, "Reduced optical scattering loss in vertical-cavity lasers using a thin (300 AA) oxide aperture," *IEEE Photon. Technol. Lett.*, vol.8, pp. 593-595 (1996)
12. E. M. Strzelecka, G. D. Robinson, L. A. Coldren, and E. L. Hu, "Fabrication of refractive microlenses in semiconductors by mask shape transfer in reactive ion etching," to be published in *Microelectronic Engineering*

B. OXIDE APERTURED VCL STRUCTURE: GROWTH, APERTURE FORMATION, AND LASER CHARACTERISTICS

B.1 GROWTH AND PROCESSING

Over the past couple of years great progress has been made in vertical-cavity lasers (VCLs) through the use of dielectric apertures to confine the current and reduce the optical losses [1-7]. Selective lateral wet oxidation of high Al content AlGaAs compounds has proven to be the most desirable technology for forming the apertures. Threshold currents below 100 μA [2-3], power conversion efficiencies of 50% [4], and device sizes as small as 2 μm (square) [5] had been realized with these structures. However, as device sizes are reduced below about 4 μm in diameter, external differential efficiencies have still dropped for these structures. Modeling of the aperture as a uniform waveguide accurately predicts the dispersion relation and modal structure for larger sizes [6], but gives no insight into the size-dependent optical loss mechanism responsible for the lower efficiency at smaller sizes. Our recent calculations on optical scattering losses in all-epitaxial VCLs with abrupt dielectric apertures, as illustrated in Fig. B.1.1a, show that even for a perfectly "smooth" aperture edge, light is scattered away from the device and lost [9,10]. Figure B.1.1b schematically shows effective optical cavities with either an ideal lens or abrupt aperture as a focusing element (the mirrors include both wavelength and angular dependence) . The mode experiences a spatially dependent phase shift as it passes through the cavity. As is well known, for the ideal lens the phase shift perfectly focuses the mode, providing a lossless resonator. For the "smooth" abrupt aperture, the abrupt phase discontinuity produced in the wavefront also focuses the light, but in addition leads to scattered light which excites higher order modes or is radiated out of the device. This loss becomes appreciable as the device diameter is reduced. By reducing the thickness (and phase discontinuity) of the aperture, the optical scattering loss is predicted to decrease. As one might expect, the ideal aperture has a laterally parabolic phase shift like an ideal lens. Our experiments have shown reduced optical loss in an all-epitaxial VCL with a 300 Å thick oxide aperture, in agreement with the prediction.

The laser structure used is shown in Fig. B.1.1a. A p-type intra-cavity contact is used in this structure to avoid current pumping through the p-type mirror. Growth is done in a Varian Gen II solid-source MBE machine on a (100) GaAs n-type substrate. The growth was done at 600°C (530°C for the active region) under a high As_2 overpressure. The bottom distributed Bragg reflector (DBR) is composed of 18.5 periods GaAs/AlAs and the interfaces are linearly graded over 180 Å using a variable duty cycle digital alloy. The interfaces are Si-doped at $5x10^{18}$ cm^{-3} and the rest of the mirror is Si-doped at $1x10^{18}$ cm^{-3}. The active region is centered in a one-wavelength long cavity and is composed of three 80 Å $Ga_{0.82}In_{0.18}As$ quantum wells (QWs) separated by 80 Å GaAs barriers and 100 Å GaAs spacer layers. The remainder of the cavity consists of $Al_{0.3}Ga_{0.7}As$ doped with $1x10^{18}$ cm^{-3} Be or Si and 500 Å doping offsets from the active region. The first top mirror period consists of the oxidation layer and p-type contact layer. The first mirror layer is Be-doped at the same levels as the bottom mirror and consists of a 200 Å AlAs oxidation layer clad by $Al_{0.9}Ga_{0.1}As$ and 180 Å linear digital alloy gradings to form one-quarter wavelength in total thickness. The contact layer is a three-quarter wavelength GaAs layer Be-doped at $2x10^{18}$ cm^{-3}. The remaining structure consists of a 22 period undoped $Al_{0.9}Ga_{0.1}As$/GaAs DBR and phase-matching layer to gold. $Al_{0.9}Ga_{0.1}As$ was chosen as a compromise between high oxidation selectivity of AlAs [11] and high index difference in the DBR.

Processing is relatively simple. A two-level mask of SiO_2/Si is first deposited to serve as a Cl_2 reactive ion etch mask. This mask gives a double-mesa structure in one step [12]. The etch is stopped when the contact layer is reached on the inner mesa. The outer mesa exposes the oxidation layer. Lateral oxidation is carried out at 450°C in a flowing, water-saturated nitrogen ambient. The oxidation selectivity of the 200 Å AlAs layer over the $Al_{0.9}Ga_{0.1}As$ is quite high. In 15 minutes, the oxidation distance is 10 μm for the AlAs and 1 μm for the $Al_{0.9}Ga_{0.1}As$. The blow-up in Fig. B.1.1a shows a cross sectional transmission electron microscope (TEM) picture of the oxidized aperture. As seen in the picture, the oxidized layer appears thicker than the original AlAs layer and a slight taper exists near the end. This is most-likely due to a slight oxidation of the $Al_{0.9}Ga_{0.1}As$ on either side of the aperture. The resulting aperture thickness is about 300 Å. After oxidation, the surface is passivated with SiN and a circular window is opened up for the evaporation of a p-type Cr/Au/Zn/Au ohmic contact. The contact is annealed and thick gold is plated over the pillar to facilitate heat-sinking [13] and future flip-chip bonding. A broad-area back-side Ti/Au contact and SiO antireflective coating are deposited to finish the process.

B.2 DEVICE RESULTS AND DISCUSSION

Figure B.2.1 shows the DC output power curves for four aperture diameters (determined by lateral mode spacing as in [6]). The external differential efficiency at threshold is also labeled and the inset shows the lasing spectra for the 2.3 μm device at maximum power. The broad-area laser threshold current density for the 3 QW structure is about 1200 A/cm^2, which is almost double the best reported number (715 A/cm^2) for a similar structure [4] due to a higher background optical loss and non-radiative carrier recombination in the active layer. However, a low threshold current of 250 μA (near state-of-the-art for a 3 QW structure) is still obtained for a 2.3 μm diameter device since no additional scattering losses are added by the aperture. Due to the low threshold currents and the intra-cavity p-type contact layer, threshold voltages are about 1.85 Volts and maximum wall-plug efficiencies are at 18% for all but the smallest devices. Series resistance is higher than expected due to a poor p-type contact resistance and limits the maximum efficiency. The 2.3 μm and 3 μm devices have greater than 30 dB of side-mode suppression (see inset in Fig. B.2) over the entire operating range and output more than 1.6 mW of single-mode power. However, devices larger than 4.5 μm all have multiple-lateral modes at and above threshold, indicating very low mode-selective loss for the larger devices. The striking feature of these devices is the small reduction in differential efficiency as the size is reduced. All devices larger than 4.5 μm have a differential efficiency of 0.53 As the device size is reduced further, the differential efficiency only decreases by 10% for a 3 μm device and 20% for a 2.3 μm device. This indicates a very small increase in optical losses.

By looking at the differential efficiency, η_{ext}, the optical loss, L (percent of light lost per pass) through the cavity can be determined as follows [14]:

$$L(d) = T\left(\eta_{inj} / \eta_{ext}(d) - 1\right)$$

where d is the device diameter, T is the optical transmission out the cavity and η_{inj} is the injection efficiency (assumed to be 0.8 from measurements in broad-area in-plane lasers). The scattering loss (excess loss) due to the abrupt aperture is found by subtracting the loss found for larger devices which have no size-related scattering loss. In this way, the size-independent optical losses associated with material absorption and free-carriers (doping) are removed from the measurement. By using a numerical beam propagation simulation, developed by E. Hegblom et al., the minimum (theoretical) optical scattering loss is also calculated for different abrupt aperture thicknesses [9,10]. The optical mode is calculated by propagating a field many times around the laser cavity and adjusting the gain until a self-consistent solution is reached. A spatially dependent phase shift is applied to the wavefront upon each pass to simulate the aperture and the angular reflectivity spectrum of the DBR is used to simulate the mirrors. Based on the complete one-dimensional simulation, an approximate model was formed to predict the results in two dimensions. The optical scattering loss is taken to be the increase in modal gain relative to the broad area structure.

Figure B.3 shows a plot of the measured differential efficiency and calculated scattering loss (for all-epitaxial structures) versus device size for several aperture thickness placed in the center of the first quarter-wave layer of the DBR. Measured results for this work (300 Å aperture) and previous work (800 Å aperture) [15] are plotted for comparison with each other and theory. The 800 Å aperture devices have the same epitaxial structure as the 300 Å aperture devices except that the oxidation layer is a one-quarter wave thick AlAs layer and the upper mirror is doped p-type with an average doping level of 1×10^{18} cm^{-3}. The theoretical curves represent the minimum optical loss that can be expected for the abrupt apertures and the 800 Å aperture device is assumed to have the minimum scattering loss for a 9 μm device due to a lack of larger device sizes for this sample.

In this way, a fair comparison is made between structures. The differential efficiency for larger devices (>8 μm) is lower for the 800 Å aperture, which is expected due to the extra p-type doping (free-carrier loss) in the upper DBR. The measured scattering loss falls above the theoretical predictions in both cases. However, the measured scattering loss for the 300 Å aperture is significantly lower than the 800 Å aperture case and falls well below the theoretical minimum for the thicker apertures. For 2.3 μm devices, the differential efficiency drops by 50% for the 800 Å device and by only 20% for the 300 Å device. Thus, the benefits of a thinner oxide aperture are clearly demonstrated. More study is needed to understand the reason for higher loss than theory.

In summary, we have fabricated and tested dielectrically apertured VCLs with thin 300 Å oxide apertures. The optical scattering loss from the 300 Å apertures was quantified and found to be significantly less than the loss from 800 Å apertures. The optical loss reduction for smaller device sizes resulted in 2.3 μm single-mode devices with differential efficiencies of 0.43 and 1.2 mW of DC power. This differential efficiency is at 80% of the broad-area device. The theory indicates that the use of thinner or tapered apertures should result in even lower scattering loss, enabling a further VCL size reduction.

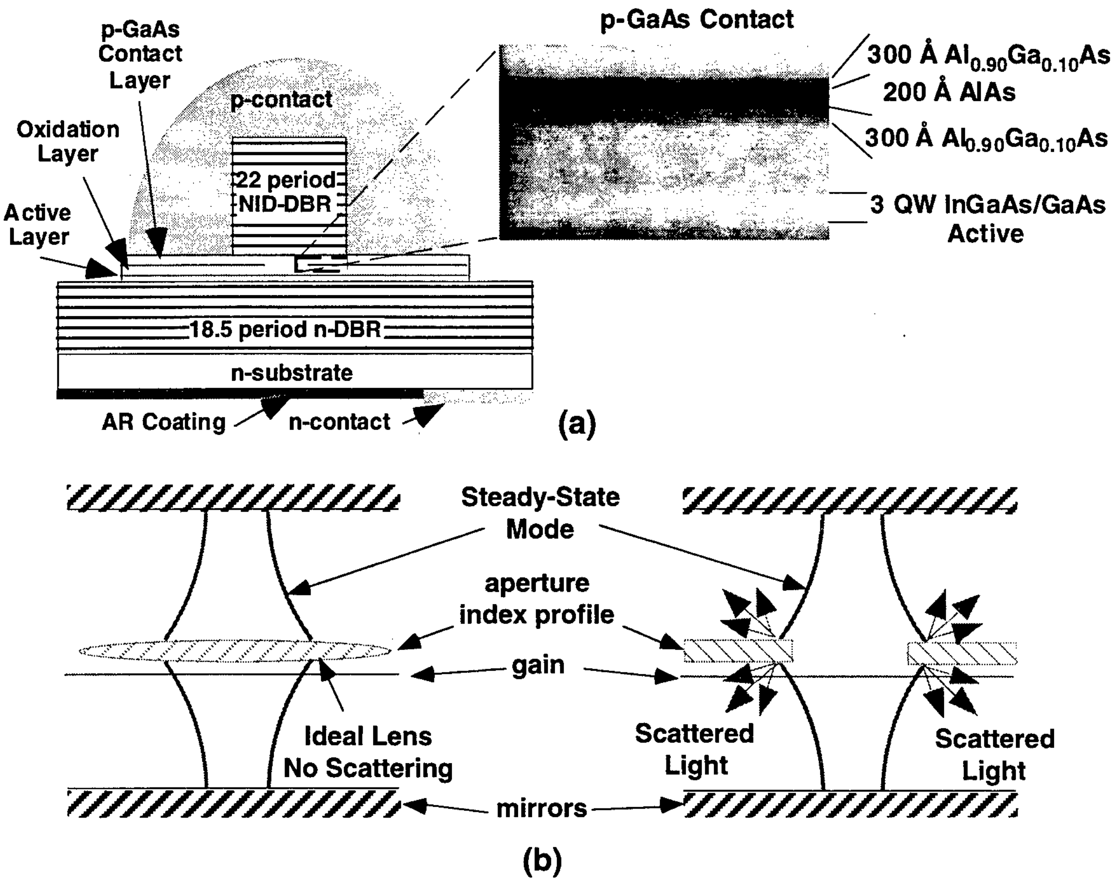

Figure B.1.1: (a) Schematic of all-epitaxial bottom emission vertical-cavity laser. The p-type contact is made in the first 3/4 wavelength GaAs mirror layer to avoid pumping current through a p-type mirror and allows the top mirror to be undoped. Oxidation proceeds from the outer mesa. The blow-up shows a transmission electron micrograph ((200) dark field) of the oxidized AlAs layer. The oxide (~300 Å) is thicker than the AlAs layer (200 Å) and has a small taper due to slight oxidation of the cladding $Al_{0.9}Ga_{0.1}As$.
(b) Illustration of optical cavity for structure in (a) with either an ideal perfect lens or an abrupt aperture. Scattering loss as a result of the phase discontinuity produced by the abrupt aperture is indicated.

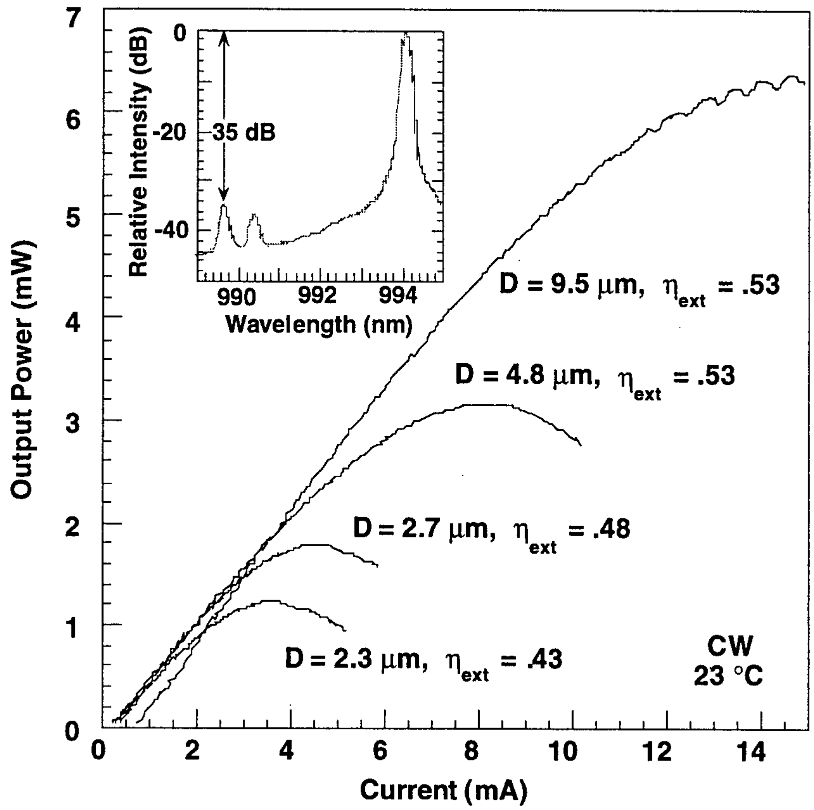

Figure B.2.1: Continuous wave (CW) output power curves for various aperture diameters. The inset shows the lasing spectra of the 2.3 μm device at peak power. Threshold currents are as low as 250 μA and threshold voltages are near 1.8 V. The differential efficiency at threshold decreases only slightly as the device is scaled and is at 80% of the broad area value for the 2.3 μm device. The two smallest devices are purely single-mode (<30 dB side-mode suppression) over the entire operating range, while all larger devices operate with multiple lateral modes.

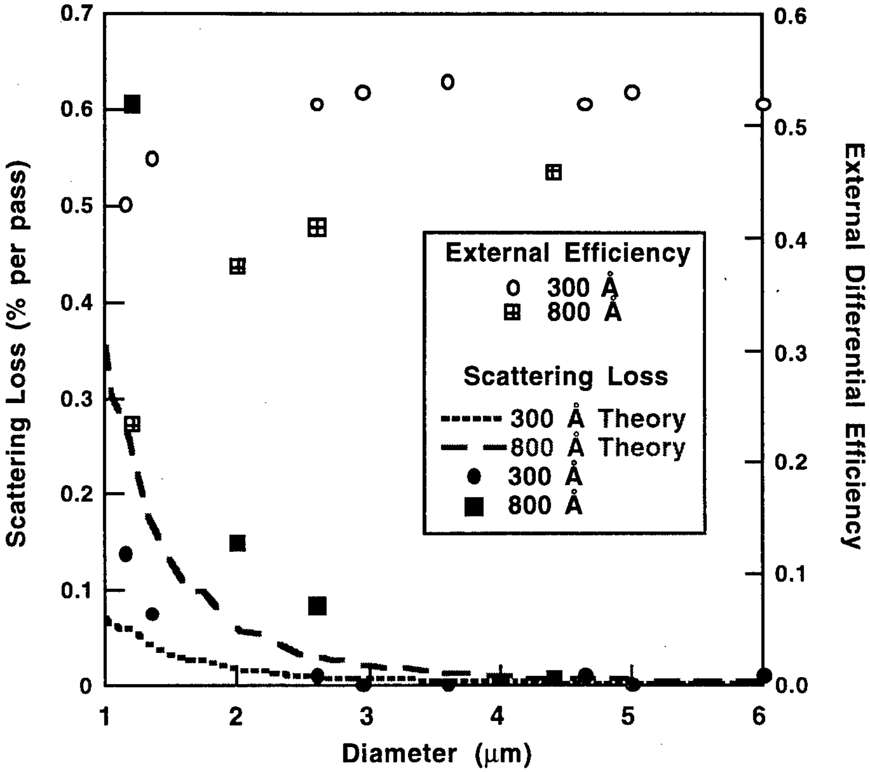

Figure B.2.2: Measured external differential efficiency and comparison of optical scattering loss between 300 Å apertures (this work), 800 Å apertures [13], and theory [7,8]. The theoretical curves give the limits for the minimum achievable loss. The transmission, *T*, is .007 for this structure. The 300 Å aperture data is lower than both the measured and theoretical values for the thicker oxide, verifying the significant scattering loss reduction.

REFERENCES TO SECTION B

1. J. W. Scott, B. J. Thibeault, D. B. Young, and L. A. Coldren, "High Efficiency Sub-Milliamp Vertical Cavity Lasers With Intra-Cavity Contacts", *IEEE Photonics Technology Letters,* **6** (6), pp. 678-680, 1994.
2. D. G. Deppe, D. L. Huffaker, J. Shin, and Q. Deng, "Very-Low-Threshold Index-Confined Planar Microcavity Lasers," *IEEE Photonics Technology Letters*, **7** (9), pp. 965-967, 1995.
3. Y. Hayashi, T. Mukaihara, N. Hatori, N. Ohnoki, A. Matsutani, F. Koyama, and K. Iga, "Record Low-Threshold Index-Guided InGaAs/GaAlAs Vertical-Cavity Surface-Emitting Laser with A Native Oxide Confinement Structure,"*Electronics Letters*, **31** (7), pp. 560-561, 1995.
4. K. L. Lear, K. D. Choquette, R. P. Schneider, Jr., S. P. Kilcoyne, and K. M. Geib, "Selectively Oxidised Vertical Cavity Surface Emitting Lasers with 50 % Power Conversion Efficiency,"*Electronics Letters*, **31** (3), pp. 208-209, 1995.
5. D. L. Huffaker, D. G. Deppe, and K. Kumar, "Native-oxide defined ring contact for low threshold vertical-cavity lasers," *Applied Physics Letters*, **65** (1), pp. 97-99, 1994.
6. K. L. Lear, K. D. Choquette, R. P. Schneider, Jr., and S. P. Kilcoyne, "Modal Analysis of a Small Surface Emitting Laser with a Selectively Oxidized Waveguide," *Applied Physics Letters*, **66** (20), pp. 2616-2618, 1995.
7. P. D. Floyd, B. J. Thibeault, E. R. Hegblom, J. Ko, L. A. Coldren, and J. L. Merz, "Comparison of optical losses in dielectric-apertured vertical-cavity lasers," *IEEE Photonics Technology Letters*, **8** (5), 1996.
8. J. M. Dallesasse, N. Holonyak, Jr., A. R. Snugg, T. A. Richard, and N. El-Zein, "Hydrolization Oxidation of AlxGa1-xAs-AlAs-GaAs Quantum Well Heterostructures and Superlattices," *Applied Physics Letters*, **57** (26), pp. 2844-2846, 1990.
9. E. R. Hegblom, D. I. Babic, B. J. Thibeault, J. Ko, R. Naone, and L. A. Coldren, "Estimation of Optical Scattering Losses in Dielectric Apertured Vertical Cavity Lasers," *submitted to Applied Physics Letters*, 1995.
10. B. J. Thibeault, E. R. Hegblom, P. D. Floyd, Y. Akulova, R. L. Naone, and L. A. Coldren "Reduced Optical Scattering Loss in Vertical-Cavity Lasers with Thin or Tapered Oxide Apertures," *IEEE LEOS '95*, PD 2.1, San Francisco, CA (October 30 - November 2, 1995).
11. K. D. Choquette, R. P. Schneider, Jr., K. L. Lear, and K. M. Geib, "Low Threshold Voltage Vertical-Cavity Lasers Fabricated by Selective Oxidation," *Electronics Letters*, **30** (24), pp. 2043-2044, 1994.
12. B. J. Thibeault, J. W. Scott, M. G. Peters, F. H. Peters, D. B. Young, and L. A. Coldren, "Integrable InGaAs/GaAs Vertical-Cavity Surface-Emitting Lasers," *Electronics Letters,* **29** (25), pp. 2197-2198, 1993.
13. T. Wipiejewski, D. B. Young, M. G. Peters, B. J. Thibeault, and L. A. Coldren, "Improved Performance of Vertical-Cavity Surface-Emitting Diodes with Au-Plated Heat Spreading Layer," *Electronics Letters*, **31** (4), pp. 279-280, 1995.
14. B. J. Thibeault, T. A. Strand, T. Wipiejewski, M. G. Peters, D. B. Young, S. W. Corzine, L. A. Coldren, and J. W. Scott, "Evaluating the Effects of Optical and Carrier Losses in Etched Post Vertical Cavity Lasers," *Journal of Applied Physics*, **78** (10), 1995.
15. P. D. Floyd, B. J. Thibeault, L. A. Coldren, and J. L. Merz, "Reduced Threshold Bottom Emitting Vertical Cavity Lasers by AlAs Oxidation," *LEOS - 95* , paper SCL14.2, pp. 414-415, 1995.

C. HIGH SPEED MODULATION CHARACTERISTICS OF VCLS

In this section, we characterize the high-speed modulation properties of thin-oxide-apertured vertical-cavity lasers. The modulation response scales with device diameter due to the negligible optical scattering loss present in these devices. A small diameter laser of 3.1 μm has a maximum 3 dB bandwidth of 15.3 GHz at bias of only 2.1 mA. Modelling indicates a no-parasitic bandwidth of 18.2 GHz at this current level, with an intrinsic 3 dB bandwidth limit of 45 GHz due to gain compression. The present devices are limited by parasitic capacitance across the thin oxide layer.

Vertical-cavity lasers (VCLs) are very desirable for many high-speed applications due to their small modal volume, which promises very low threshold currents and high speeds at low current levels. Due to a greatly reduced optical scattering loss, VCLs using AlAs-oxide defined dielectric apertures have lead to small diameters <3μm [1-3]. With the small modal volume, threshold currents <150 μA [3-5] and record modulation speeds >16 GHz [6] at 4.5 mA of current have been achieved . However, VCLs have been unable to reach modulation bandwidths over 20 GHz. In this section, we characterize the modulation characteristics of very low-scattering loss VCLs that use thin oxide apertures [2].

Figure C.1 shows a schematic of the final processed structure used in this study. The laser was grown by solid-source molecular beam epitaxy (MBE) at a temperature of 600°C (530°C for the active region) under a high As_2 overpressure. The layer structure consists of a 21 period $Al_{0.9}Ga_{0.1}As/GaAs$ ($\lambda/4$ / $\lambda/4$ in thickness) distributed Bragg reflector (DBR), a $3\lambda/4$ thick p-type GaAs contact layer doped at 2×10^{18} cm^{-3}, a 200 Å thick AlAs oxidation layer embedded in a $\lambda/4$ thick $Al_{0.9}Ga_{0.1}As$ layer, a 3 quantum well (QW) $In_{0.17}Ga_{0.83}As/GaAs$ (80 Å/80 Å) active region centered in a 1λ thick $Al_{0.3}Ga_{0.7}As$ cavity, and a 18.5 period AlAs/GaAs n-type DBR with 180 Å linear digital alloy gradings doped at 1×10^{18} cm^{-3} in the bulk and 5×10^{18} cm^{-3} at the interfaces. The processing details are available in ref. [2]. The key distinguishing feature is the use of the very thin oxide layer for reduced optical scattering losses.

To do the high-speed testing, Indium is first evaporated onto the tops of the gold-plated pillars. Then the devices are flip-chip bonded to Indium bumps on the ends of 50Ω coplanar transmission lines patterned on SI GaAs. Figure C.2 shows the DC performance of the devices after bonding. The devices perform slightly better than the unbonded lasers in ref. [2] due to slightly improved heat-sinking. The devices have threshold currents as low as 300 μA for a 3.1 μm diameter device and have a constant differential efficiency of 55% for all sizes, indicating the negligible optical scattering loss [2]. Threshold voltages are 1.75 V- 1.9 V for all devices. The nearly constant wall-plug efficiency of ~17% is limited by series resistance. Laser sizes (indicated by effective diameters) are determined from the measured lateral mode spacing of the device [7].

The modulation response (S21) is measured with an HP 8510C network analyzer. The input signal is composed of a DC bias and a 0 dBm microwave signal generated with an HP 8340B sweeper. The light signal is focused by the integrated back-side microlens on the laser into a multimode fiber. The light is detected by a New Focus 1435 photoreceiver and is amplified by a 15 dB New Focus 1422 amplifier. The final output is measured with an HP 8514A S-parameter test set. Figure C.3 shows the smoothed response of the 3.1 μm diameter VCL at several bias current levels. A maximum bandwidth of 15.2 GHz at only 2.1 mA of current is demonstrated. This is the highest bandwidth reported at this low of a current level, demonstrating the benefit of the small modal volume in VCLs. The maximum bandwidth did not increase with further bias.

From the slope of the 3 dB frequency versus $(I - I_{th})^{1/2}$ we can determine the modulation current efficiency factor (MCEF) which is related to the fundamental device properties as follows:

$$MCEF = \frac{f_{3dB}}{\sqrt{I - I_{th}}} = \frac{1.55}{2\pi}\sqrt{\zeta \frac{g' v_g \eta_i}{q V_{opt}}} \qquad (1)$$

where ζ is the standing wave enhancement factor, g' is the differential gain in cm^2, v_g is the group velocity, η_i is the internal quantum efficiency, q is the electronic charge , and V_{opt} is the modal volume (area x effective cavity length, L_{cav}). The MCEF scales inversely with device diameter giving 14 GHz/mA$^{1/2}$, 8.7 GHz/mA$^{1/2}$, and 5.7 GHz/mA$^{1/2}$ for the 3.1 μm, 5.2 μm, and 8.8 μm devices respectively. For $\zeta = 1.83$, $v_g = 8.57\text{x}10^9$ cm/s, $\eta_i = 0.8$, and $L_{cav} = 1.7$ μm, we obtain $g' = 5.61\text{x}10^{-16}$ cm^2, which agrees well with the literature [8-9]. The linear scaling indicates that the differential gain is not reduced due to increased optical loss as the device size is reduced. For higher biases in all devices, the data deviates from linearity due to response peak broadening and suppression. This suppression can be due to gain compression caused by spatial or spectral hole burning at high cavity photon densities, by device heating which can cause increases in threshold current and decreases in differential gain, or by parasitic capacitance.

In order to determine which mechanism limits performance in the VCLs, the modulation response at each bias point was fit with a three parameter fit [10] :

$$|H(f)|^2 = \frac{1}{\left(1+(f/f_o)^2\right)} \frac{1}{\left(1+(f/f_r)^2\right)+(\gamma/2\pi f_r)^2(f/f_r)^2} \qquad (2)$$

where f_o is the parasitic cut-off frequency, f_r is the relaxation resonance frequency, and γ is the damping frequency. For the 3.1 µm diameter VCL, a value of f_o of 10 GHz gave the best fit over all bias levels. Estimates of the capacitance across the thin 300 Å oxide layer indicate that the parasitic limit is due to this capacitance. If this parasitic limit is removed, the modulation bandwidth at 2.1 mA should be 18.2 GHz. The values of f_r and γ both vary with device bias and give the necessary information to determine the intrinsic limits to device performance (neglecting device heating).

Figure C.4 shows the linear plots of f_r^2 and γ versus output power. From these plots the differential gain, g', and gain compression parameter, ε, are determined [10].

$$g' = \frac{4\pi^2 \eta_{opt} h\nu V_{opt}}{v_g} \frac{df_r^2}{dP_{out}} \tag{3}$$

$$\varepsilon = \left[\frac{1}{4\pi^2 \tau_p} K - 1 \right] \frac{g'}{\Gamma g}, K \equiv \frac{d\gamma}{df_r^2} \tag{4}$$

where $\eta_{opt} = 0.69$ is the optical efficiency of the cavity, $h\nu$ is the photon energy, τ_p is the photon lifetime (gv_g^{-1}), $g = 1200\ \text{cm}^{-1}$ is the material gain, and $\Gamma = 0.026$ is the overall confinement factor. Values of g' = $5.86\text{x}10^{-16}\ \text{cm}^2$ (within 5 % of previous calculation) and $\varepsilon = 0.59\text{x}10^{-17}\ \text{cm}^3$ (slightly smaller than reported for in-plane lasers [9]) are obtained. The ultimate intrinsic 3 dB bandwidth limit, neglecting heating, is obtained from the K-factor [10] :

$$f_{3dB,\max} = \frac{2\pi\sqrt{2}}{K} \tag{5}$$

For K = 0.194 ns, the maximum bandwidth obtainable is 45 GHz. To obtain higher bandwidths, it is necessary to reduce the parasitic capacitance, which occurs across the thin oxide aperture used in the present devices. However, using thicker oxides will result in higher optical losses, which will decrease the differential gain in the device. To address both problems simultaneously, tapered apertures are proposed to provide a thick oxide layer under the contact layer while providing a more lens-like aperture for the optical mode, keeping the optical loss low [11].

In summary, we have demonstrated a 3 dB bandwidth of 15.2 GHz at only 2.1 mA of current, the highest bandwidth reported at this low of a current. Due to low optical scattering loss, the high frequency performance scales with device size. At present, parasitic capacitance limits the maximum bandwidth, but measurements indicate a maximum potential 3 dB bandwidth of 45 GHz.

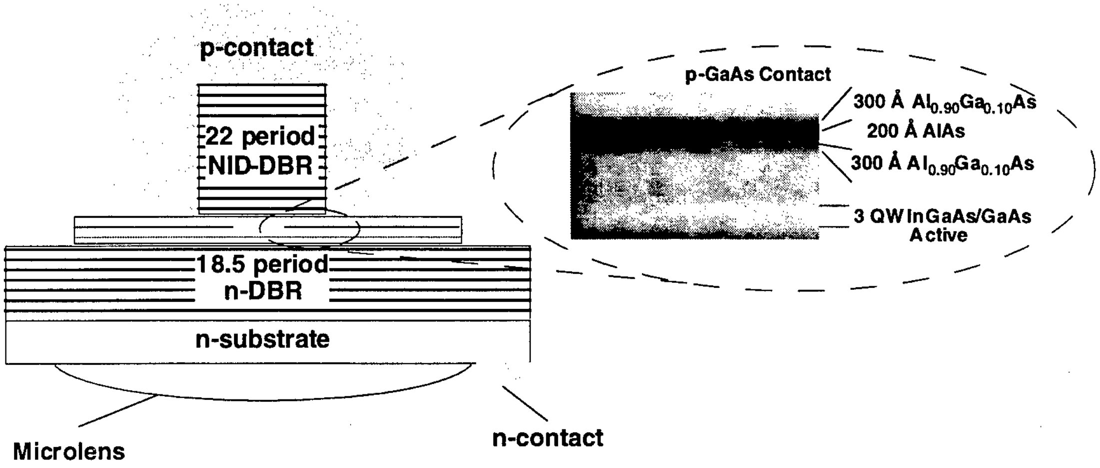

Figure C.1: Device Schematic. A p-type intra-cavity contact is used to avoid driving current through the p-type mirror. Gold is plated over the whole device to improve heat-sinking and ease stress induced by flip-chip bonding.

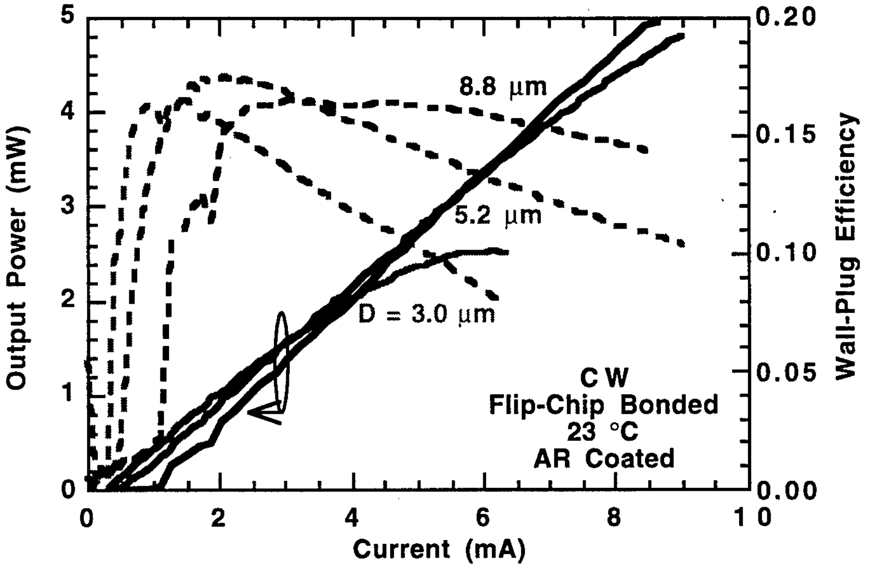

Figure C.2: Continuous wave (CW) output power and wall-plug efficiency curves for three device sizes. The threshold voltages are 1.75 - 1.9 V and the wall-plug efficiency is limited by series resistance. The 3.1 μm VCL has a threshold current of 300 μA.

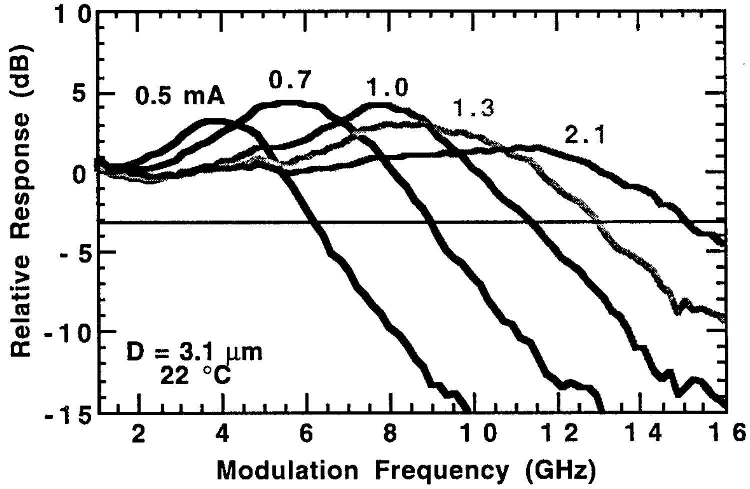

Figure C.3: Small-signal modulation response of 3.1 μm VCL at various bias currents. 15.3 GHz is obtained for only 2.1 mA of current. The peak response broadening and suppression indicates a damping mechanism.

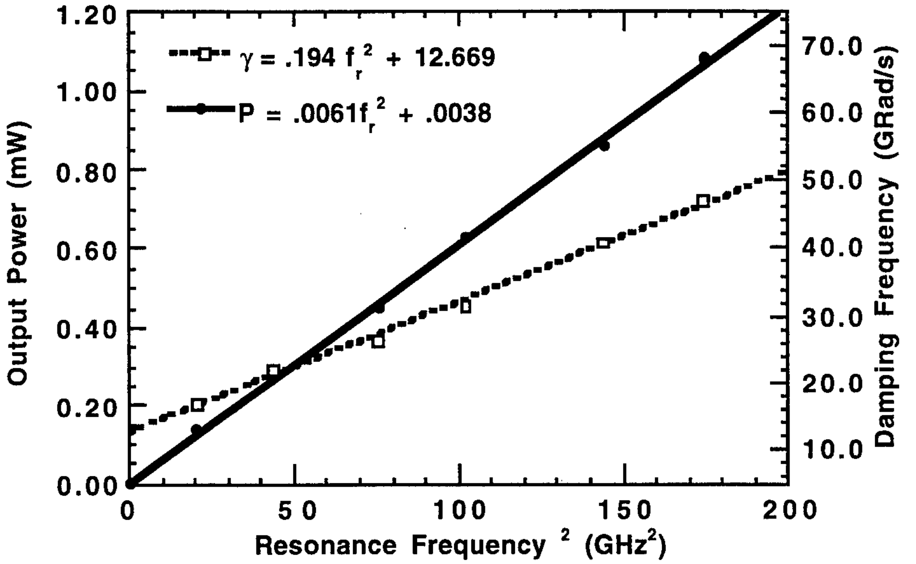

Figure C.4: Damping frequency, γ, and output power, P, as function of resonance frequency squared, f_r^2. The intrinsic parameters g' and ε are determined from these graphs. From this data, the intrinsic bandwidth limit, neglecting heating, is 45 GHz.

REFERENCES TO SECTION C

1. K. D. Choquette, H. Q. Hou, K. L. Lear, H. C. Chui, K. M. Geib, A. Mar, and B. E. Hammons, "Self-pulsing oxide-confined vertical-cavity lasers with ultralow operating current," *Electronics Letters*, **32** (5), pp. 459-450 (1996).
2. B. J. Thibeault, E. R. Hegblom, P. D. Floyd, R. Naone, Y. Akulova, and L. A. Coldren, "Reduced Optical Scattering Loss in Vertical-Cavity Lasers Using a Thin (300Å) Oxide Aperture," *IEEE Photonics Technology Letters*, **8** (5), pp. 593-595 (1996).
3. D. L. Huffaker, J. Shin, and D. G. Deppe, "Low threshold half-wave vertical-cavity lasers," *Electronics Letters*, **30** (23), pp. 1946-1947, 1994.
4. K. D. Choquette, K. L. Lear, R. P. Schneider, Jr., K. M. Geib, and H. C. Chui, "Selectively Oxidized Vertical-Cavity Lasers," *IEEE LEOS '95 Proceedings*, paper SCL 14.1, pp. 412-413 (1995)
5. Y. Hayashi, T. Mukaihara, N. Hatori, N. Ohnoki, A. Matsutani, F. Koyama, and K. Iga, "Record low-threshold index-guided InGaAs/GaAlAs vertical-cavity surface-emitting laser with a native oxide confinement structure," *Electronics Letters*, **31** (7), pp. 560-561 (1995).
6. K. L. Lear, A. Mar, K. D. Choquette, S. P. Kilcoyne, R. P. Schneider, Jr., and K. M. Geib, "High frequency modulation of oxide-confined vertical cavity surface emitting lasers," *Electronics Letters*, **32** (5), pp. 457-458 (1996).
7. K. L. Lear, K. D. Choquette, R. P. Schneider, Jr., and S. P. Kilcoyne, "Modal analysis of a small surface emitting laser with a selectively oxidized waveguide," *Applied Physics Letters*, **66** (20), pp. 2616-2618 (1995).
8. J. W. Scott, B. J. Thibeault, C. J. Mahon, and L. A. Coldren, "High modulation efficiency of intracavity contacted vertical cavity lasers," *Applied Physics Letters*, **65** (12), pp. 1483-1484 (1994).
9. R. Nagarajan, T. Fukushima, J. E. Bowers, R. S. Geels, and L. A. Coldren, "Single quantum well strained InGaAs/GaAs lasers with large modulation bandwidth and low damping," *Electronics Letters*, **27** (12), pp. 1058-1059 (1991).
10. L. A. Coldren, and S. W. Corzine, *Diode Lasers and Photonic Integrated Circuits*, John Wiley and Sons, Inc., New York, pp. 201-204 (1995).
11. E. R. Hegblom, D. I. Babic, B. J. Thibeault, and L. A. Coldren, "Estimation of scattering losses in dielectrically apertured vertical cavity lasers," *Applied Physics Letters*, **68** (13), pp. 1757-1758 (1996).

D. INTEGRATION WITH MICROLENSES

D.1 LENS DESIGN AND FABRICATION

Wafer-level integration of optoelectronic devices with microlenses results in components that can be used directly in systems, without the need of aligning external optics. Combinations of VCLs, LEDs, or detectors, with microlenses have applications in optical fibre systems, free-space optical computer interconnections [1], displays, printers, etc. Refractive lenses, etched in the back side of the substrate, have several advantages over diffractive lenses. Besides the simple and manufacturable fabrication technology, the lens optical efficiency is primarily limited by the absorption of the substrate, which is nominally transparent. Furthermore, these lenses are far less sensitive to wavelength variations. We have developed a process for fabricating refractive microlenses in GaAs and InP with the ability to control the radius of curvature (ROC) within ±10%, suitable for many practical applications. The process requires formation of a lens-shaped mask which is then transferred into the substrate by reactive ion etching (RIE) [2]. Microlenses can be formed from deposited materials, such as photoresist [3] or polyimide [4], on the surface of the substrate. However, by taking the process one step further and etching the lens in the substrate, we eliminate a refractive index discontinuity at the lens-substrate interface and reduce the lens thickness, since semiconductor materials have a high refractive index. In our microlens fabrication the lens-like shape of patterned, reflowed photoresist is transferred into the semiconductor by anisotropic dry etching. We chose reactive ion etching over etching with inert ions [5] to achieve faster etch rates and a controllable ratio of the etch rate in the semiconductor to that in the erodable mask material. The latter allows precise control of the lens shape by adjusting the etch rate ratio during mask transfer.

D.1.1 Lens mask formation

The microlens fabrication process is illustrated in Fig. D.1.1. Formation of a lens-shaped mask is the first part of the fabrication process. Since the lens ROC is primarily controlled by the shape of the erodable resist mask, the initial mask material thickness and diameter are of most importance. The polyimide PMGI (polydimethylgluteimide), used as an erodable mask, is spin-coated on the substrate and patterned into circles of desired lens diameter. This is done by patterning a thin layer of conventional photoresist and then exposing the PMGI to deep UV light and developing. PMGI can also be patterned in O_2 plasma or RIE, which prevents undercutting and loss of its volume. Conventional Novolak photoresist is removed with acetone. In case thick layers are needed, several layers of PMGI are coated and baked at 200°C on a hot plate after each spin. The initial thickness of PMGI is roughly set by the spin speed and then adjusted by *in-situ* controlled etchback in O_2 RIE, after patterning. The semiconductor in the field is etched to form a pedestal, prior to reflow of the mask. The edge of the pedestal, typically 0.1 to 0.5 μm, creates surface tension that prevents the PMGI from spreading during reflow, and results in preserving the lithographically defined diameter. Dry etching preserves better the edge of the circle. However, wet etching, though in some cases crystallographic, may also be applied for a shallow pedestal etch without much distortion of the lens shape, especially in case of large diameter lenses (> 100 μm).

Next, the patterned PMGI cylinders are reflowed into lenses. The reflowed PMGI shape depends on the time and temperature of reflow as well as on the feature's aspect ratio. PMGI melts just below 300°C, and after ~30 minutes forms a round mound. The reflowed shape is well fitted by a paraboloid whose volume and diameter remain the same as the original cylinder before reflow, resulting in the peak height after reflow being twice the cylinder height. This is valid for height to diameter ratios greater than 0.015. Very thin layers of PMGI remain planar in the central region and deform only around the perimeter due to surface tension, as shown in Fig.D.1.2. Hence, to achieve semiconductor surfaces with very large ROC, a thicker mask should be chosen and the pattern transfer in subsequent RIE done with a small semiconductor to mask etch rate ratio.

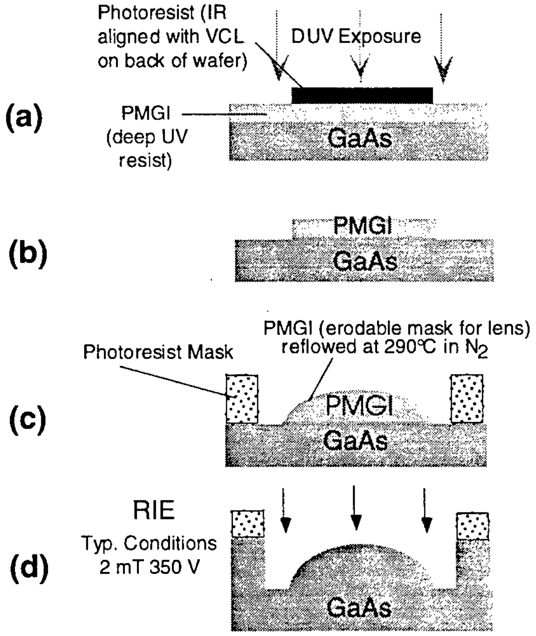

Figure D.1.1: Process flow of refractive microlens fabrication.

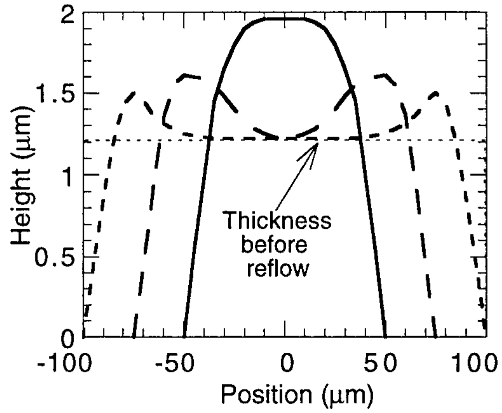

Figure D.1.2: Surface profilometer scans of PMGI after reflow at 290°C for 20 min. for three different diameters and aspect ratios.

D.1.2 Transfer of mask to substrate

The lens-like shape of the mask is transferred to a semiconductor substrate in RIE. The final lens shape strongly depends on the ratio of etch rate in the semiconductor to that in the PMGI. Two *in-situ* optical monitors in our RIE reactor allow us to control the etch rate ratio thereby achieving a desired curvature of the surface and correcting for aberrations. PMGI etch rate is monitored by measuring the intensity of 632.8 nm HeNe laser light reflecting from a sample coated with a known initial thickness of the material. Due to interference between the top reflection and the reflection from the PMGI-substrate boundary, the signal exhibits periodic variations as the PMGI surface etches, with a period proportional to the etch rate, material's refractive index, and incidence angle. Etch rate of bulk semiconductors is monitored by measuring a diffracted beam from the surface patterned with parallel lines. As the exposed semiconductor etches, the diffracted signal exhibits periodic variations with a period proportional to the etch rate and incidence angle. The lines are masked with nickel and sputtered aluminum oxide which has a much smaller etch rate than the semiconductors. The *in-situ* monitors allow us to adjust the etch rate ratio of the mask and semiconductor materials in the begining of the etch to achieve the desired final lens curvature.

D.1.3 Microlenses in GaAs

The etch rate of GaAs increases with pressure, due to the increasing chemical nature of the process, whereas the PMGI etch rate remains fairly constant, as shown in Fig. D.1.3. The bias voltage proportionately increases the etch rate of both materials. The etch rate of GaAs is about 1.5 to 3 times faster than PMGI. Under typical conditions (2 mT and 350 V bias), the etch rates of GaAs and PMGI are 220, and 110 nm/min, respectively. At pressures higher than 7 mT the GaAs etch rate further increases but the semiconductor undercuts and the etch becomes crystallographic due to ion scattering and an abundance of reactive species. The initial mask is made thinner than the final GaAs microlens, as illustrated by profilometer scans shown in Fig. D.1.4.

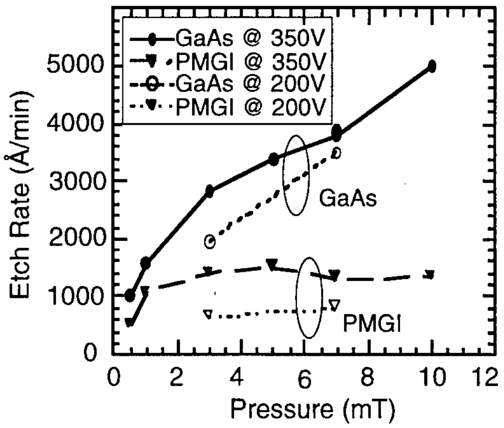

Figure D.1.3: Etch rates of GaAs and PMGI as a function of pressure and bias voltage in Cl_2 RIE.

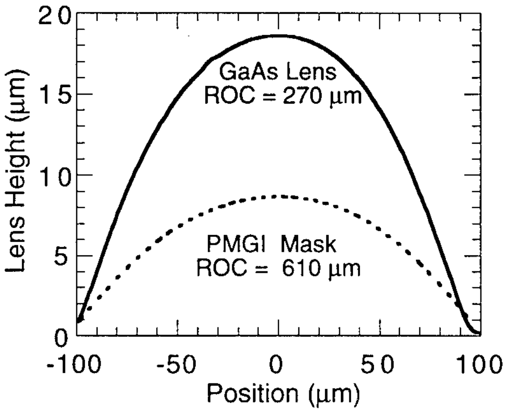

Figure D.1.4: Surface profilometer scans of the lens-shaped mask before RIE and the GaAs lens after transfer of the pattern in Cl_2 RIE.

D.2 INTEGRATION OF LASERS WITH MICROLENSES

The microlenses are integrated with VCLs, as shown in Fig. D.2.1. For integration with devices, the microlens is recessed into the semiconductor wafer, as shown in Fig. D.2.2, for ease of handling, lens surface protection, and contact metallization. This is achieved by protecting some areas of the surface with thick photoresist, patterned after lens mask formation, prior to RIE, as illustrated in Fig. D.1.1. The lenses are aligned to the laser features in a IR mask aligner. It was found that it is best to fabricate the microlenses in the early stage of the VCL process, before definition of the VCL pillars. This prevents the VCL pillar from beeing torn off during processing on the back side. Though the VCLs can be protected with wax, small diameter devices as well as devices with the oxide layer are very fragile.

As an example, microlens requirements for collimation of a VCL beam exiting through a 500 μm substrate are ROC ≈ 360 μm (focal length ~142 μm in air). The lens diameter requirements depend on the original divergence of the laser. To ensure minimum diffraction from the lens perimeter, for this application, we typically produce lenses of diameters between 100 and 200 μm. Because the distance between the lens and the laser is fixed by the substrate thickness (~ 500 μm), the output beam divergence depends not only on the lens focal length but also on the initial laser diameter. The far-field beam divergence angles were measured for several types of single-mode laser and lens combinations. The half-angles of $1/e^2$ of beam intensity were measured by laterally scanning a small aperture across the beam and confirmed by angularly scanning a single mode fiber. A summary of these results is shown in Table 1. The first four cases are of etched post VCLs. The output beams can be either collimated or focused down depending on the lens focal length. The first case is of the beam focusing at about 100 μm outside the lens and diverging even stronger than the original beam. The last case shows that for very small diameter lasers, achieved by using dielectrically apertured structures [6], the beam can be collimated down to 1° half-angle, due to the initial (without lens) strong divergence of ~13°, which allows the beam to fill the lens.

Table 1

Far-field half-angles of VCSELs integrated with refractive microlenses

Laser characteristics		Lens characteristics			Output beam
laser dia. (μm)	laser beam half-angle in air (no lens)	Lens diameter (μm)	Peak height (μm)	focal length in air (μm)	half-angle in air with lens
7	6.5°	100	8.8	60	12.3°
7	6.5°	150	8.8	125	2.2°
7	6.5°	200	8.8	225	1.9°
6	8.1°	200	17.4	117	1.1°
3.1	13°	200	13.8	151	1°

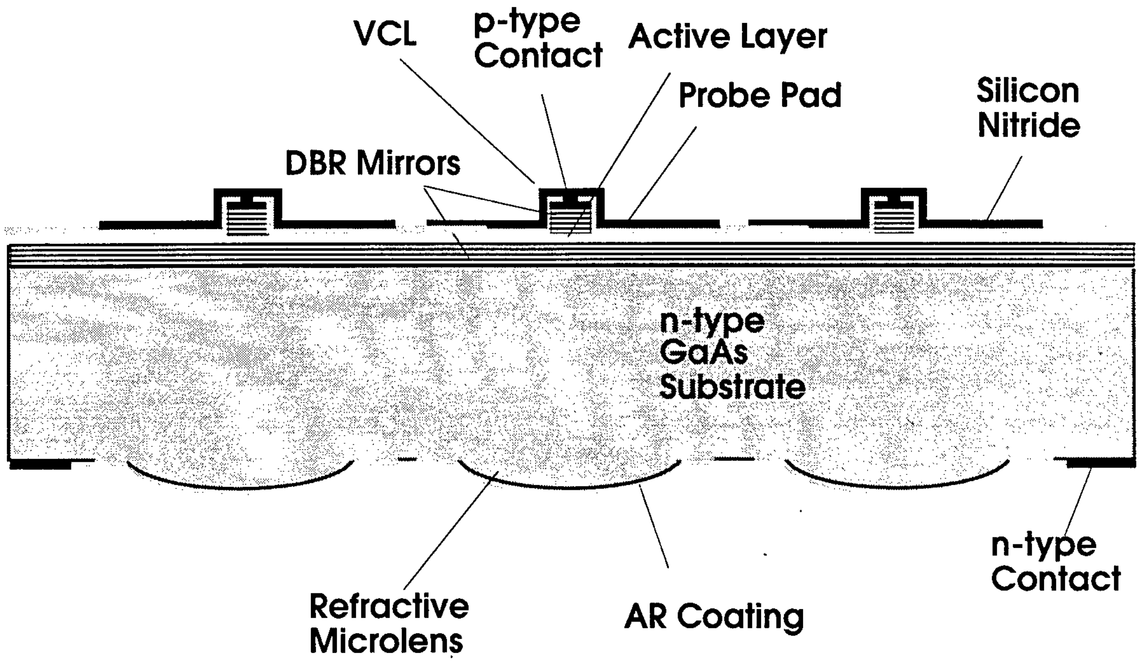

Figure D.2.2: Schematic of a VCL array integrated with microlenses.

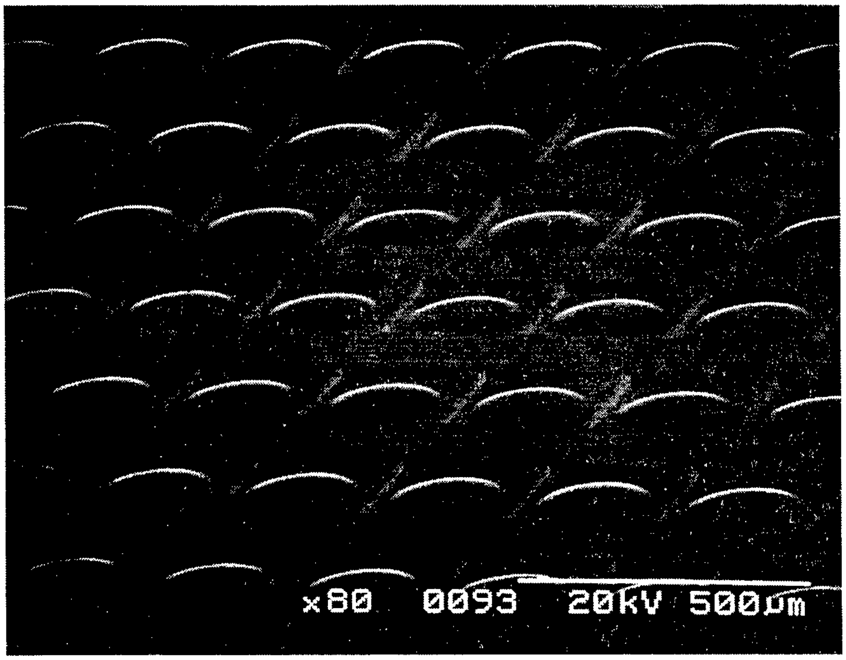

Figure D.2.3: Scanning electron microscope image of GaAs microlenses recessed in the substrate.

D.3 INTEGRATION OF DETECTORS WITH MICROLENSES

Detectors used for the free-space optical interconnect demonstration are double-pass Schottky diodes. A 5000Å thick NID InGaAs absorption layer is grown lattice matched on an InP n-type substrate. A 900Å thick linearly graded superlatticethat ends with 300Å thick InAlAs and a cap InGaAs (later removed) is grown on top of the absorption layer. The Schottky metal, which also serves as a reflector, is deposited by e-beam evaporation on the InAlAs layer. Our first efforts in microlens integration with InP substrates required wafer fusion of a GaAs substrate to the back side of the InP substrate. The microlenses were fabricated with the well controlled process in GaAs. We have successfully fabricated lensed devices in the wafer bonded material. The device arrays were diced and flip-chip bonded on submounts, as shown in Fig. D.3.1.

Further efforts were made to develop a monolithic fabrication of microlenses in InP. The process required increased etch rates and improving reproducibility of InP RIE. InP etches very slowly in Cl_2 at room temperature due to low volatility of indium chloride reaction products. Under similar RIE conditions as for GaAs, the InP etch rate is only 40 nm/min while the PMGI etch rate is ~110 nm/min. This requires very thick mask layers and long etch times to from microlenses. Furthermore, the smothness of the etched surface is not well controlled. In a different RIE reactor (PlasmaTherm SR-700), we have used BCl_3/Cl_2 chemistry to etch InP microlenses. The pressure was kept low (~2 mT) to improve the volatility of the reaction products, and the gas composition was varied to increase the etch rate of InP relative to PMGI. At lower RF powers (200 - 350 W) the InP to PMGI etch rate ratio can be varied from 0.6 to 1.4 by changing the flow rate ratio of BCl_3 to Cl_2 from 1 to 4. The etch rates are in the 100 nm/min range. By increasing RF power to 465 W (900 V bias), at flow rate ratio of BCl_3 to Cl_2 equal to 3, the etch rate of InP increased to 182 nm/min while the PMGI etch rate increased to 150 nm/min. With these conditions, microlenses were etched in InP substrates with high quality, optically smooth surfaces. The higher power provides enough energy to reactively etch InP without the need to heat the substrate. In the same conditions, conventional Novolak photoresist erodes at a rate ~ 80 nm/min, allowing the lens to be recessed for integration with devices, as shown in Fig. D.3.2.

In summary, we have developed a process for fabrication of refractive microlenses in GaAs and InP, which relies on transfer of a lens-shaped erodable mask by RIE. The ability to control the ratio of the etch rate in the semiconductor to that in the erodable mask material allows greater flexibility of the resulting radius of curvature of the microlens. Integration of microlenses with VCLs and with back illuminated photodiodes for focusing onto the detector [1] has resulted in components that we subsequently used in a free-space optical interconnect demonstration.

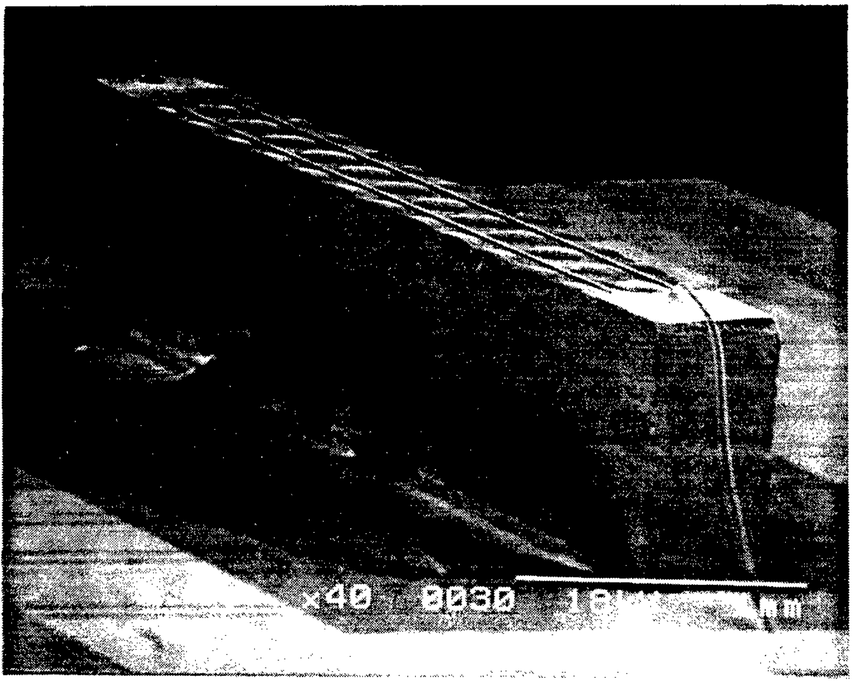

Figure D.3.1: Scanning electron microscope image of a lensed detector array flip-chip bonded to transmission lines. The microlenses are etched in a GaAs wafer which was fused to the InP substrate prior to processing.

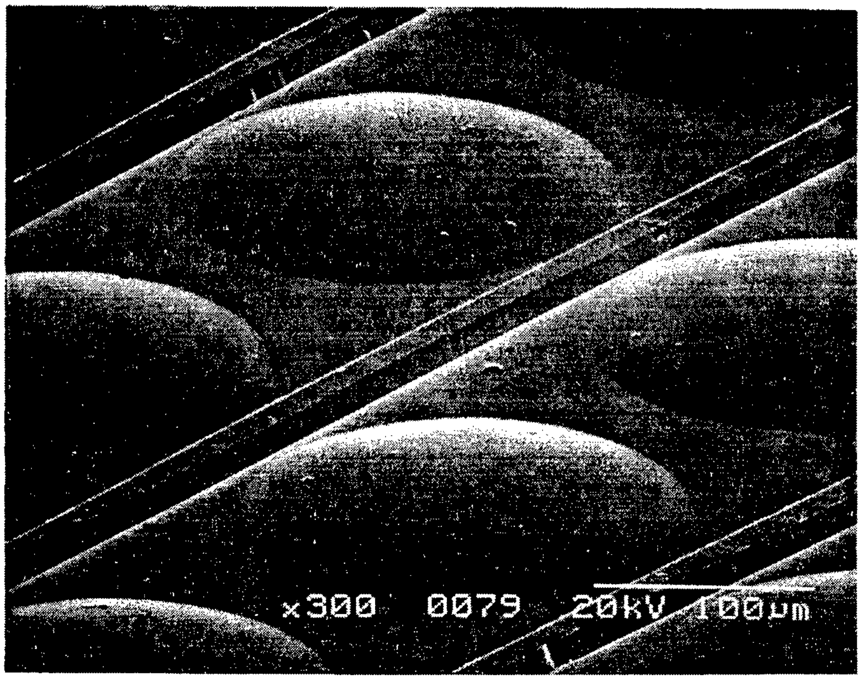

Figure D.3.2: Scanning electron microscope image of an InP microlens etched in Cl_2/BCl_3 RIE.

REFERENCES TO SECTION D

1. E. M. Strzelecka, G. B. Thompson, G. D. Robinson, M. G. Peters, B. J. Thibeault, M. Mondry, V. Jayaraman, F. H. Peters, and L. A. Coldren, SPIE, vol. 2691, pp. 43-53 (1996)
2. E. M. Strzelecka, G. D. Robinson, M. G. Peters, F. H. Peters, and L. A. Coldren, *Electron. Lett.*, 31, pp. 724-725 (1995)
3. Z. D. Popovic, R. A. Sprague, and G. A. N. Connel, *Appl. Opt.*, 21, pp. 1281-1284 (1988)
4. O. Blum, S. P. Kilcoyne, M. E. Warren, T. C. Du, K. L. Lear, R. P. Schneider, Jr., R. F. Carson, G. Robinson, and F. H. Peters, *Electron. Lett.*, 31, pp. 44-45 (1995)
5 H. Sankur, E. Motamedi, R. Hall, W. J. Gunning, and M. Khoshnevisan, SPIE, vol. 2383, pp. 179-83 (1996)
6. B. J. Thibeault, E. R. Hegblom, P. D. Floyd, R. Naone, Y. Akulova, and L. A. Coldren, *IEEE Photon. Technol. Lett.*, vol. 6, pp. 593-595 (1996)

E. MULTIWAVELENGTH LASER ARRAYS WITH MICROLENSES

Dense optical interconnections over short free-space distances are needed to provide high-speed low-noise board-to-backplane data bus connections. This application is shown conceptually in Fig. E.1, where the free-space distance within the connector would be on the order of ~0.1 mm. With each device having its own collimating or focusing lens, as shown in Figs. E.1.a and b, the pitch of the device array can be no less than ~ 100 to 150 μm to prevent diffraction losses. A system which uses "collimated beams" set up between the transmitter and receiver (Fig. E.1.a) is very flexible as far as the overall interconnect length is concerned (we show for our board-to-board simulations that the length could vary between 0 and ~ 10 mm), and is not very sensitive to lateral variations, advantageous for board-to-board interconnects. However, to increase the interconnect density in a short distance interconnect, another system is proposed, where several devices share a single microlens, as shown in Fig. E.1.c. The mechanical stability is provided by the connector housing. With the same lens diameter as for individual microlenses, the area of a 16 channel connector would be reduced by a factor of 16. VCL arrays with pitch as small as 30 μm have been fabricated to study the effects of reduced pitch. In this system, the pitch is determined not only by optical considerations but also by the device properties such as electrical and thermal crosstalk [1]. Increased crosstalk due the smaller device spacing can be prevented with a combination of multiple-wavelength lasers and wavelength selective detectors can be applied in a system. This section describes a technique of fabricating multiple-wavelength VCLs on a single chip.

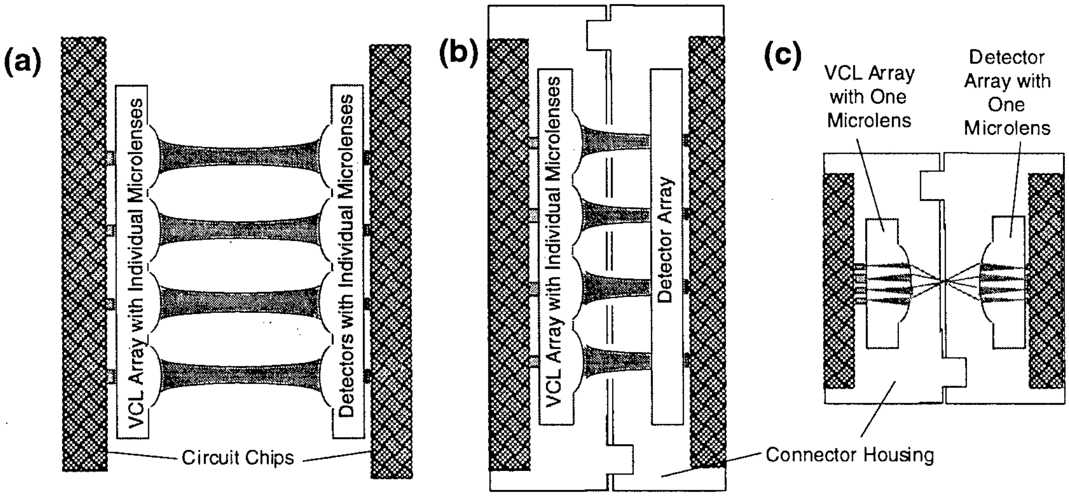

Figure E.1: Optical interconnects with lensed components (a) Lensed VCL and lensed detector arrays with collimated beams. Flexible interconnect length (0 to ~ 10 mm), applicable to board-to-board free-space interconnects. (b) Lensed VCL array with beams focusing on a detector array. Short interconnect length (0 to ~ 200 μm), applicable to optical data bus connectors (c) Closely spaced VCL and detector arrays. Interconnect length is short (0 to ~ 200 μm), applicable to optical data bus connectors.

E.1. MULTI-WAVELENGTH VERTICAL-CAVITY LASERS

The ability to fabricate lasers of different wavelength on the same chip [2-6] offers opportunities of applying VCLs in wavelength-multiplexed systems to increase data rate or to reduce crosstalk. Recently, a new method for fabricating arrays of multiple-wavelength VCSELs has been demonstrated [4-6]. It relies on adjusting the cavity mode for each laser by trimming their cavity lengths. This is accomplished by selective anodic oxidation and etchback of a GaAs spacer layer in various regions of the wafer. The laser structure is shown in Fig. E.1.1. The bottom n-type mirror consists of 15.5 periods of n-type AlAs/GaAs quarter-wave layers. The cavity contains three strained InGaAs 80Å wide quantum wells separated by 100 Å GaAs barriers. The top DBR mirror, made of p-type AlGaAs/GaAs quarter-wave layers, consists of 2 mirror periods grown above the active region, a 3/4 λ GaAs spacer layer with adjusted thickness, and 28 more DBR periods MBE regrown after the spacer layer adjustment. Precise thickness adjustment was possible by anodic oxidation of thin layers of GaAs in a solution of tartaric acid by applying a fixed bias. The oxide was subsequently etched off. With a binary coding scheme 8 different cavity lengths are achieved in three lithography-oxidation-etching steps. By applying oxidation voltages of 16.4, 11, and 8.2 V, GaAs thicknesses of 170Å, 85Å, and 43Å, respectively were removed. MBE regrowth began with a $\lambda/4$ thick GaAs layer followed by the top DBR mirror.

Individual lasers are defined by Cl_2 reactive ion etching (RIE), resulting in index guided structures that exhibit single mode behavior for 7 μm diameters. A finished device array with gold-plated probe pads is shown in Fig. E.1.2. Closely spaced arrays (30 μm pitch) of 8 lasers were produced, with total wavelength span of 17 nm centered around 978 nm. Minimum threshold currents of 720 μA and maximum power outputs 0.46 mW were achieved. An example of a VCL array characteristics is shown in Fig. E.1.3. Due to growth nonuniformity across the wafer the spactral characteristics of the array shown in Fig. E.1.3.a is centered around 955 nm. The spectral characteristics reveal single mode operation with MSR > 20 dB in the entire range of operating currents. The threshold currents are relatively uniform (~ 1 mA) for devices lasing at different wavelengths, except for devices with cavity modes near the edge of the gain spectrum. Similarly, differential efficiency is uniform, but drops nead the edge of the gain spectrum, as shown in Fig. E.1.3.c for another array.

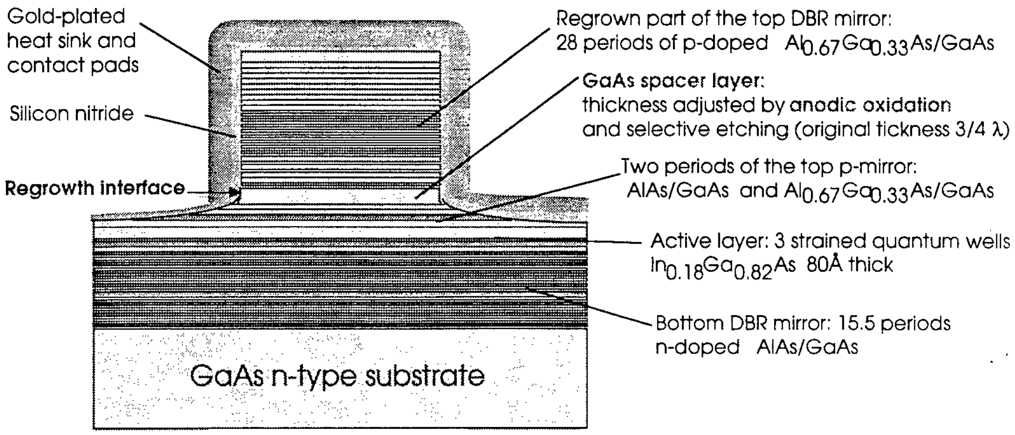

Figure E.1.1: VCL structure with adjustable cavity length.

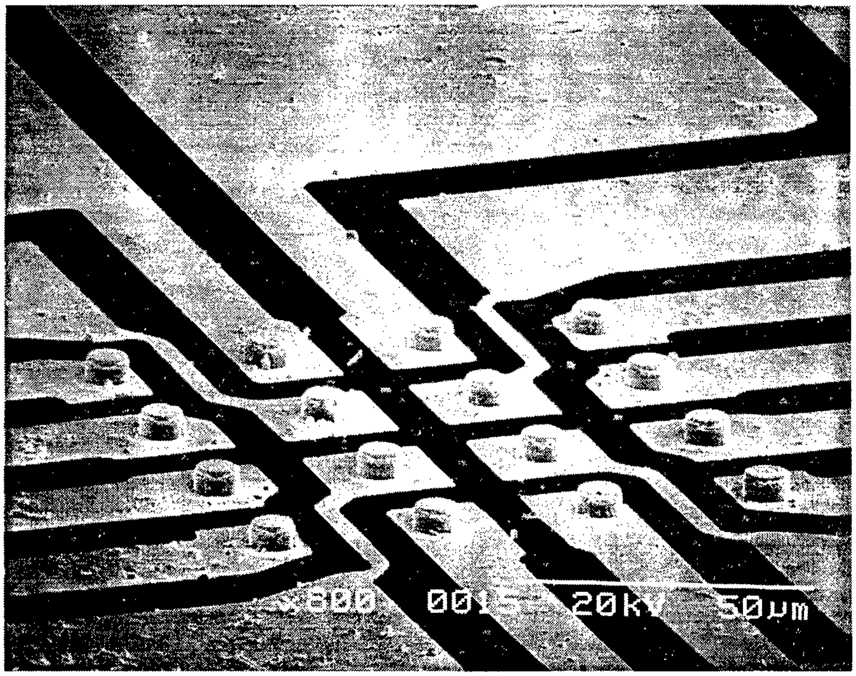

Figure E.1.2: Scanning electron micrograph of a 4x4 VCL array with 30 μm pitch.

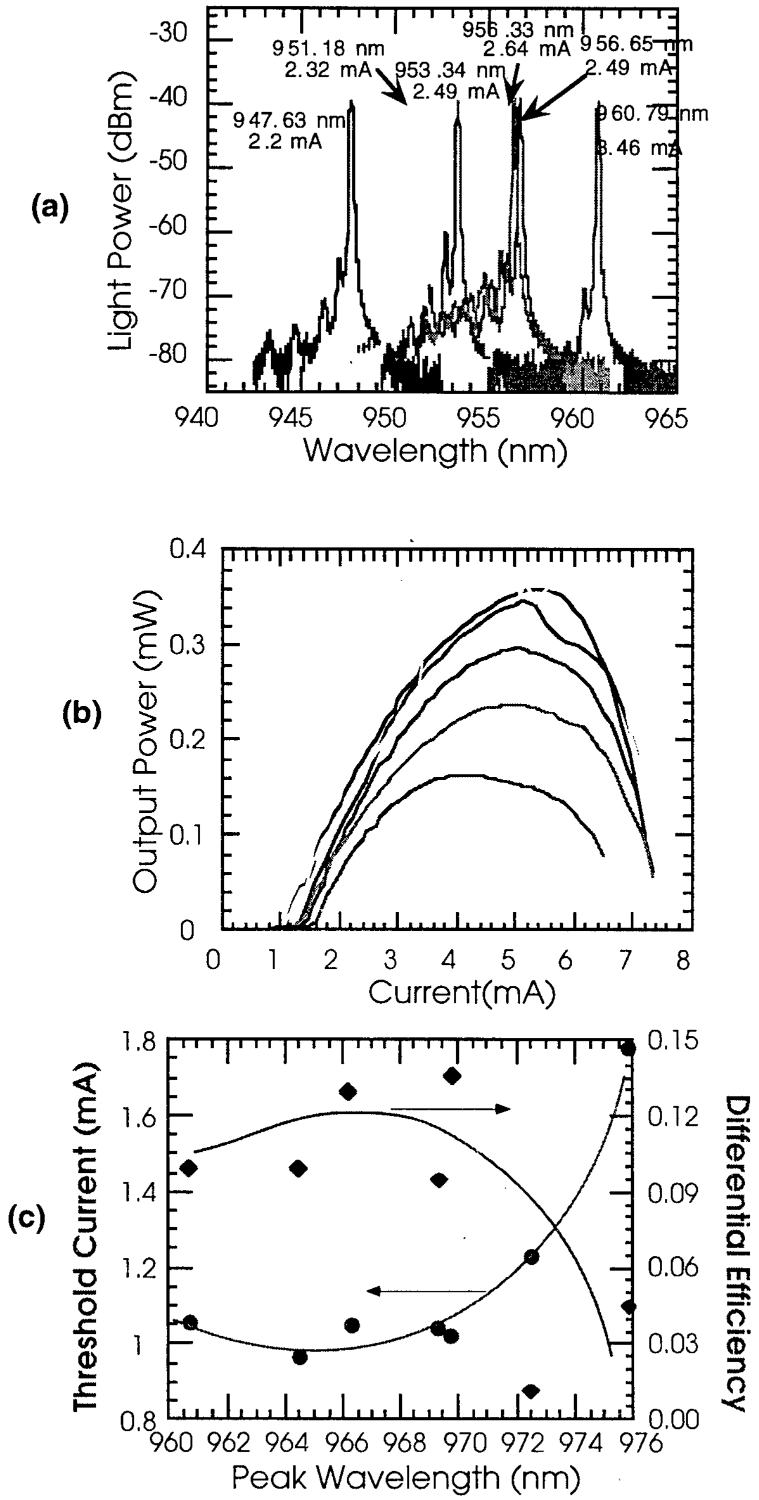

Figure E.1.3: Characteristics of a multiple-wavelength VCL array: (a) Spectra and (b) corresponding light-current characteristics. (c) Spectral dependence of threshold current and differential efficiency for another array.

E.2. VCL ARRAYS WITH MICROLENSES

In many optical systems the laser output beam has to be coupled into a fiber or collimated and directed with the use of passive optical components. These components often have to be externally mounted and actively aligned, and constitute a rather bulky part of the optical system. Monolithic integration of VCLs with microlenses [7] eliminates these issues, resulting in components that can be used directly in systems, without external optics. In this section we present monolithic integration of a closely-spaced array of multiple-wavelength VCLs with a refractive microlens [8-9]. Refractive lenses are much less sensitive to wavelength variations than diffractive lenses hence are very well suited for operation with our multiple-wavelength laser diodes.

The lasers are positioned in 2D arrays on a 30 μm pitch. Refractive microlenses are formed by Cl_2 RIE on the back surface of the unthinned GaAs substrate, across from each laser array. The refractive microlens fabrication process is included before the lasers are fully completed. Fabrication begins with definition of the lasers by deposition and patterning of the top n-type contacts. Next, the ohmic contacts are defined on the back side of the n-type substrate, followed by an anneal. Lenses, aligned to the laser arrays in a infrared mask aligner, are then formed on the back surface. Under typical etching conditions of 2 mT and 350 V bias, we formed microlenses with diameter of 253 μm and radius of curvature ~365 μm, designed for collimation. The back ohmic contact was protected with conventional photoresist during the RIE. The remaining steps of laser fabrication, including pillar definition, are done after lens fabrication.

Figure E.2.1 shows the schematic of the VCL array integrated with a refractive microlens and the device layout. The output beams are well collimated by the lens, with far-field divergence angle as low as 0.8°. Without the lens the beams would diverge at a half-angle of ~ 7°. They cross in the focal region, ~ 145 μm from the wafer, and separate angularly, depending on the radial position of the VCL from the optical axis, at 8°, 17.5°, and 27.7° measured from normal, for VCL positions 21.2, 47.4, and 63.6 μm, respectively. The far-field images of an array of seven lasers, taken with a CCD camera at distances 9 mm, 20 mm, and 30 mm from the wafer, as shown in Fig. E.2.2, illustrate how the beams spatially separate while remaining fairly well collimated. The exception is the somewhat distorted beam from the outermost laser of the array. For comparison, a beam from a device (diameter 18 μm) without a lens is shown. Its axial position does not shift but it diverges at a far-field half-angle ~6°. The angular beam profiles are measured by scanning a single mode fiber (for $\lambda = 980$ nm) on a spherical surface in the far-field. As shown in Fig. E.2.3, beams from devices near the optical axis are well collimated, with a far-field $1/e^2$ divergence half-angle of <0.85°, and exhibit no side lobes. The beams from devices positioned more than 45 μm from the optical axis exhibit side lobes. Though their 3 dB half angle is ~ 1°, the irregular side lobes are believed due to scattering from the defects in the outer region of the microlens. These defects have formed by sputtering of the partially exposed ohmic contact metals during the RIE step of lens fabrication, as shown in Fig. E.2.4.

We have coupled light from four devices in a row, each at different wavelength, simultaneously into a multimode fiber of core diameter 50 μm, as shown in Fig. E.2.5. With the fiber end parallel to the wafer and centered on the optical axis, we observed negligible degradation of the coupling efficiency of the two centermost devices (radial positions 21.2 μm) compared to the coupling optimized for one laser only. Their coupling efficiency went down from 72% (optimized for one laser) to 65% and 69% for the fiber optimized for four lasers in a row. However, the coupling efficiency of two devices positioned 47.4 μm from the axis dropped by more than one order of magnitude. Figure E.2.6 shows spectrally resolved light from the four lasers coupled into a multimode fiber. Potentially four devices with different wvelength, positioned within a radius <25 μm from the optical axis could be used in a WDM multimode fiber system.

In summary, multiple-wavelength VCLs have been fabricated on a single chip with wavelength separation ~3 nm. We have demonstrated monolithic integration of arrays of multiple-wavelength VCLs with a single microlens. With a microlens designed for collimation the output beams had a far-field divergence half-angle of <0.85°. We show that these devices are suitable for wavelength-multiplexed free-space interconnects as well as for coupling into multimode fibers.

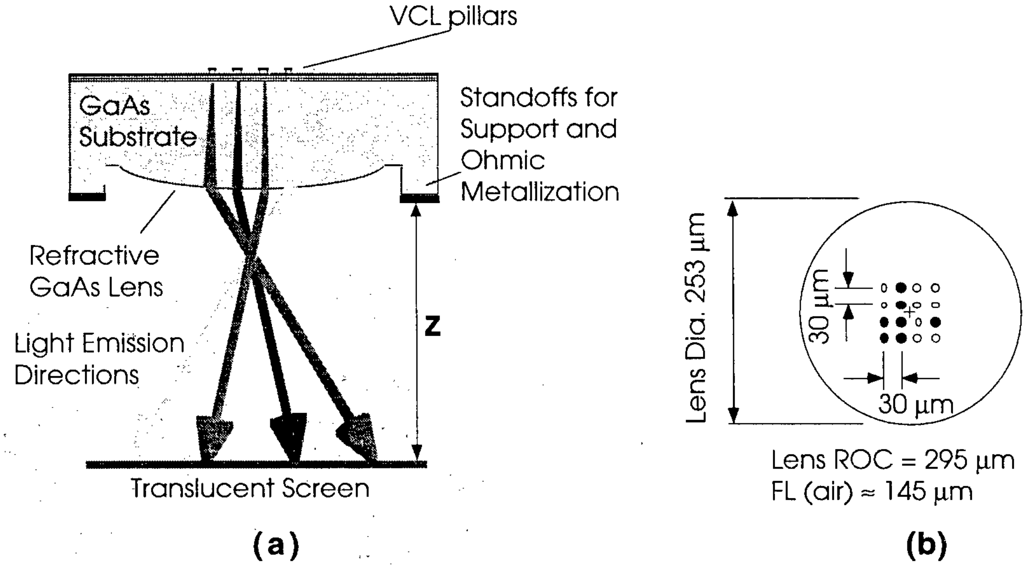

Figure E.2.1: (a) Schematic of the multiple-wavelength VCSEL array integrated with a refractive microlens. (b) Device layout.

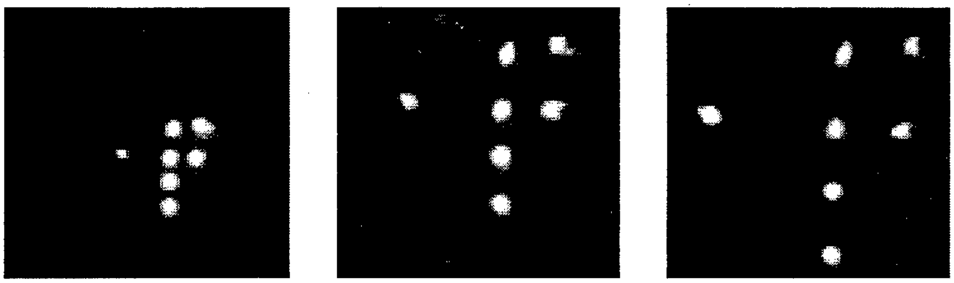
(a) (b) (c)

Figure E.2.2: Far-field CCD images of the seven laser beams taken with the screen at positions (a) 9 mm (b) 20 mm, and (c) 30 mm from the substrate. The grid size if 5 mm x 5 mm.

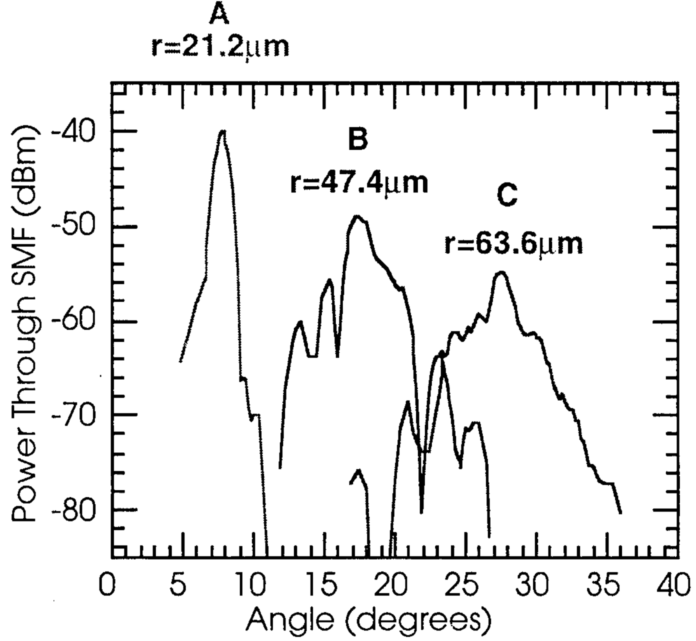

Figure E.2.3: Far-field angular beam profiles of beams originating from VCLs in different positions relative to the optical axis.

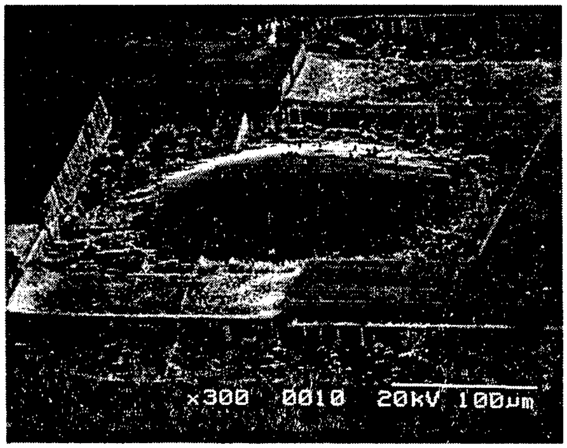

Figure E.2.4: SEM image of a microlens with defects in the perifery due to sputering of metal during RIE.

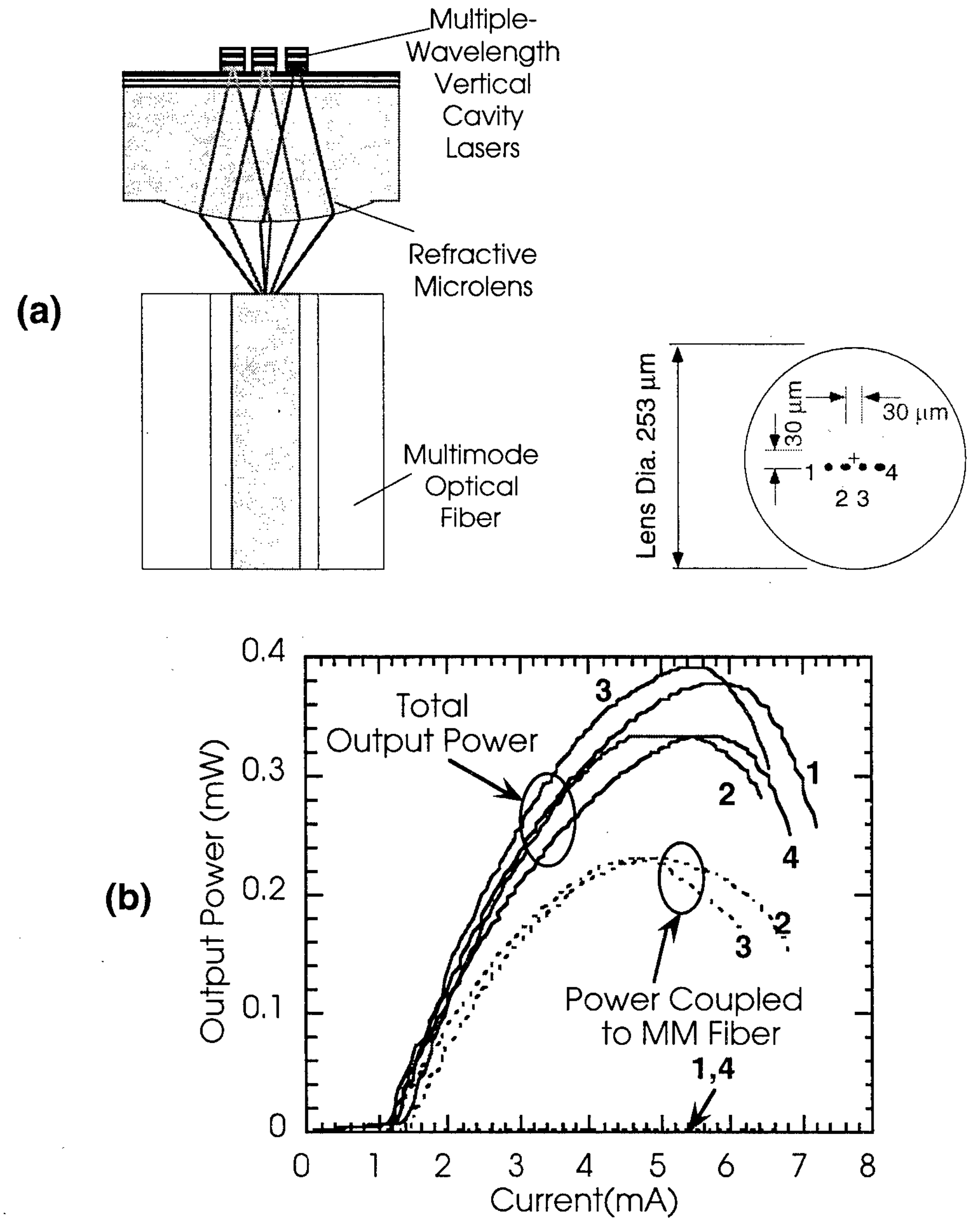

Figure E.2.5: Coupling of a multi-wavelength VCL array into a multimode fiber with an integrated microlens (a) schematic (b) light-current characteristics at the input and output of the fiber.

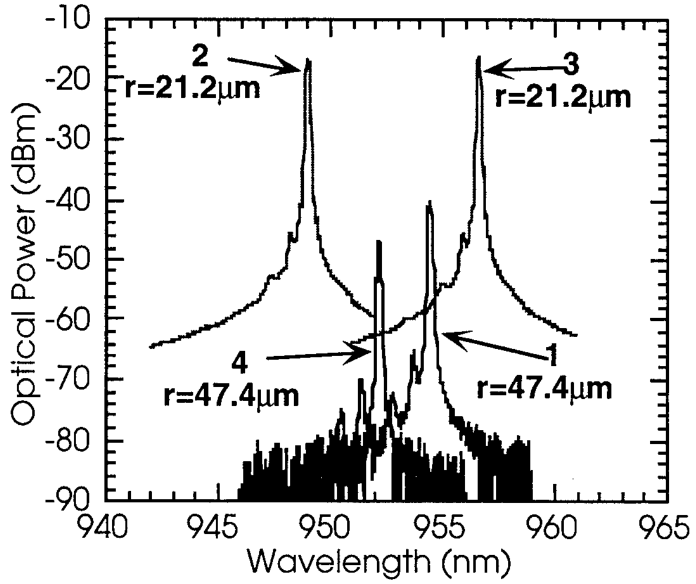

Figure E.2.6: Spectrally resolved light coupled into a multimode fiber.

REFERENCES TO SECTION E

1. T. Wipiejewski, D. B. Young, B. J. Thibeault, and L. A. Coldren, "Thermal crosstalk in 4x4 vertical-cavity surface emitting laser arrays," *IEEE Photon. Technol. Lett.*, 8, pp. 980-982 (1996)
2. W. Yuen, G. S. Li, and C. Chang-Hasnain, "Mulitple-wavelength vertical-cavity surface-emitting laser arrays with a record wavelength span," *IEEE Photon. Technol. Lett.*, 8, pp. 4-6 (1996)
3. T. Wipiejewski, M. G. Peters, E. R. Hegblom, and L. A. Coldren, "Vertical-cavity surface -emitting lase diodes with post-growth wavelength adjustment," *IEEE Photon. Technol. Lett.*, 7, pp. 727-729 (1995)
4. T. Wipiejewski, J. Ko, B. J. Thibeault, and L. A. Coldren, "Molecular beam epitaxy regrowth of top reflectors for multiple wavelength vartical-cavity lasers," CLEO, Anaheim, CA, 1996
5. T. Wipiejewski, J. Ko, B. J. Thibeault, D. B. Young, and L. A. Coldren, "2D Vertical-Cavity Laser Arrays for Free-Space and Multimode Fiber Transmission Systems," presented at 45th ECTC, Orlando, FL, 1995
6. T. Wipiejewski, J. Ko, B. J. Thibeault, and L. A. Coldren, "Multiple-wavelength vertical-cavity laser array employing molecular beam epitaxy regrowth," *Electron. Lett.*, 32, pp. 340-342 (1996)
7. E. M. Strzelecka, G. D. Robinson, M. G. Peters, F. H. Peters, and L. A. Coldren, "Monolithic intrgration of vertical-cavity laser diodes with refractive GaAs microlenses," *Electron. Lett.*, 31, pp. 724-725 (1995)
8. E. M. Strzelecka, T. Wipiejewski, J. Ko, B. J. Thibeault, and L. A. Coldren, "Multiple-wavelength MBE-regrown vertical-cavity laser arrays integrated with refractive microlenses for optical interconnections," paper P5, ISLC, Haifa, Israel, 1996
9. E. M. Strzelecka, T. Wipiejewski, J. Ko, B. J. Thibeault, and L. A. Coldren, "Monolithic integration of an array of multiple-wavelength vertical-cavity laser with a refractive microlens for optical interconnections," LEOS Annual Meeting, Boston, MA, 1996

F. FREE-SPACE INTERCONNECT DESIGN (SINGLE WAVELENGTH)

F.1 DESIGN OUTLINE

The free-space optical link under consideration consists of an array of lensed VCLs in the transmitter board and an array of lensed detectors in the receiver board, as shown in Fig. F.1.1. For board-to-board communication we assume the interconnect length L is 10 mm. Based on a Gaussian approximation we establish the beam width and lens curvature for a given L. The simulations presented below are done with actual beam profiles, not Gaussian beams. Assuming a symmetric system in which we prevent the beam from spreading, we establish "collimated beams" between the boards. As a definition of "collimated beams" we chose to make the interconnect length equal to the confocal region of the Gaussian beam. This relates the beam parameters with the interconnect length:

$$w_{tl} = w_{rl} = \sqrt{2}w_c \qquad\qquad L = \frac{2\pi w_c^2}{\lambda}$$

For $L = 10$ mm the beam waist in the center is $w_c = 40$ μm and the beam radii at the transmitter and receiver lenses are $w_{tl} = w_{rl} = 56$ μm. To minimize diffraction losses and crosstalk and yet maintain a reasonable channel spacing we assume that the array pitch should be on the order of $4w_{tl} \approx 224$ μm. We chose a 250 μm pitch for our simulations as well as for fabrication of devices. This channel spacing also ensures that adjacent devices are thermally isolated.

To obtain a beam of radius of $w_{tl} = w_{rl} = 56$ μm at the back side of the substrate, the beam must diffract quite substantially from the source. This can be optimized with a tradeoff between the VCL beam radius and VCL-lens distance. For VCLs fabricated on standard GaAs substrates of thickness 500 μm, the required laser beam waist is ~0.8 μm. This is difficult, though potentially possible, to achieve, even with the low loss oxide aperture structures. A wider diameter VCL or a index guided VCL without an aperture would require a thicker substrate to obtain the same performance. We analyze interconnect sensitivity assuming such a case, where the VCL diameter is 6 μm, the substrate thicknesses L_1 and L_2 are 1250 μm, and the lens has a radius of curvature R of 860 μm.

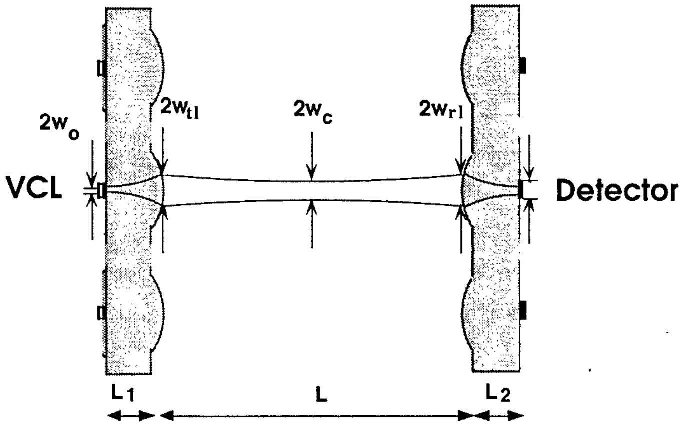

Figure F.1.1: Schematic of the analyzed interconnect link.

F.2 TOLERANCES OF A BOARD-TO-BOARD INTERCONNECT

System sensitivity to misalignment and fabrication variations is analyzed based on the scalar diffraction theory, assuming a fundamental HE_{11} mode emitted by an index guided VCL of diameter 6 μm. A finite lens diameter of 230 μm is assumed. The system is optimize for an interconnect length of 10 mm. We find the power insertion loss and crosstalk fron the nearest neighbors positioned 250 μm away in a linear array. The results are shown in Figs F.2.1 - F2.3.

Relative lateral shifts and angular deviations between the transmitter and receiver boards are the most critical parameters. Both types of misalignments cause the spot focused in the detecor plane to walk off from the detector area. Longitudinal translations from the optimum receiver placement are not very critical since we are dealing with a "collimated" system. The exception is when detector area is small in which case defocusing will spread the beam spot beyond the detector area. We choose as optimum detector diameter of 15 μm. Increasing the diameter beyond this value does not imrpove the insertino loss characteristics while crosstalk increases. This also is a good size to provide large enough bandwidth for our system.

Assuming the system will tolerate up to -3dB insertion loss and -30 dB crosstalk, the lateral misalignment is limited to ±80 μm based on insertion loss and ±90 μm based on crosstalk. Though this value is small in terms of mechanical tolerances, it constitutes a large fraction of the device-to-device spacing. Angular misalignments of ±1.2° in the detector plane and ±0.45° in the VCL plane can be tolerated. Longitudinal placement uncertainty up to 5 mm is allowed. Fabrication uncertainties such as substrate thickness variation and lens curvature variations are shown in Fig. F.2.3. The beam in the substrate is highly divergent, and the collimation of the free-space beam depends on its thickness. Fortunately, semiconductor substrates supplied by most manufacturers are specified within ±25 μm, resulting in tolerable insertion loss and crosstalk levels. The lens radius of curvature R has to be specified within about ±10%. If *R* is too small, the beam waist location shifts toward the transmitter; if R is too large, the beam diverges from the lens without going through a waist. In either case the beam radius at the receiver increases, increasing insertion loss. However, the required lens tolerance can be achieved with the process control techniques described in Section D.

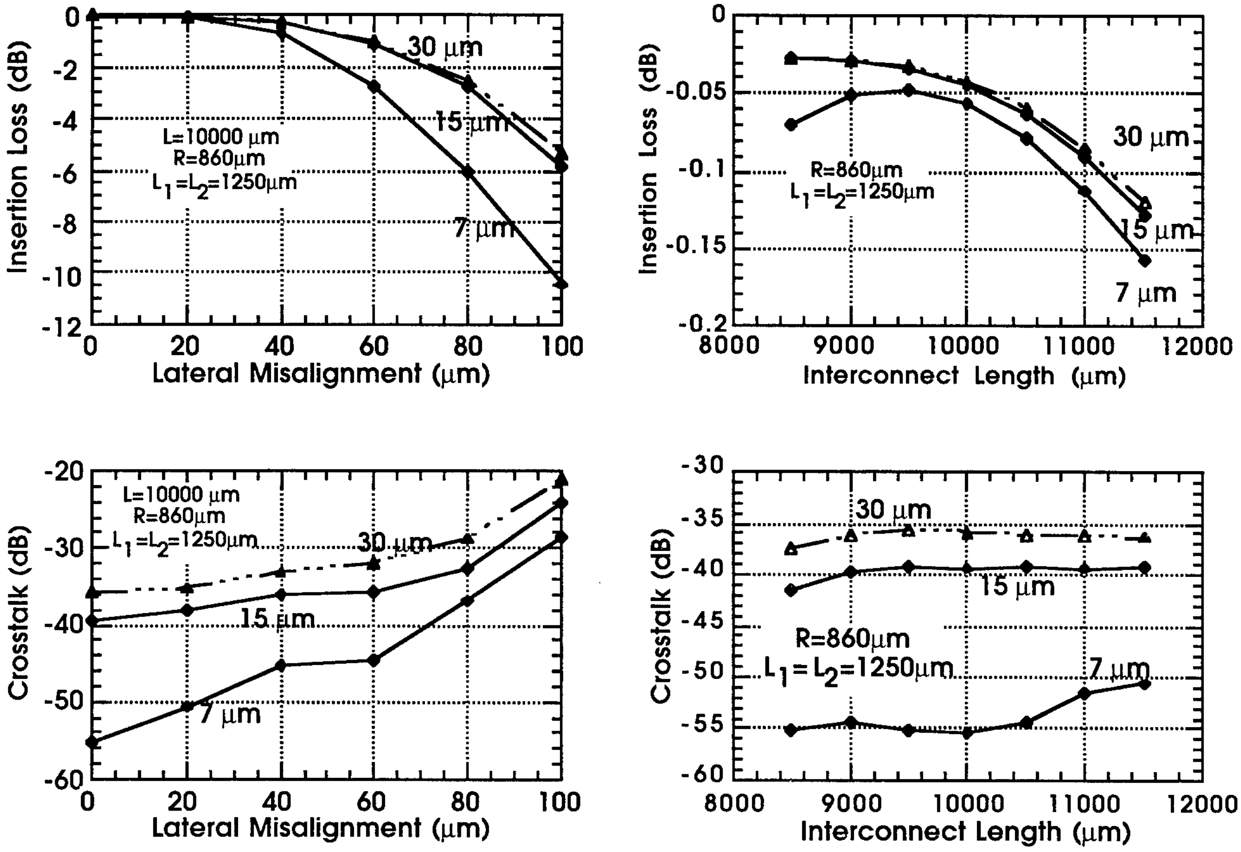

(a) (b)

Figure F.2.1: Insertion loss and crosstalk as a function of (a) lateral and (b) longitudinal misalignments.

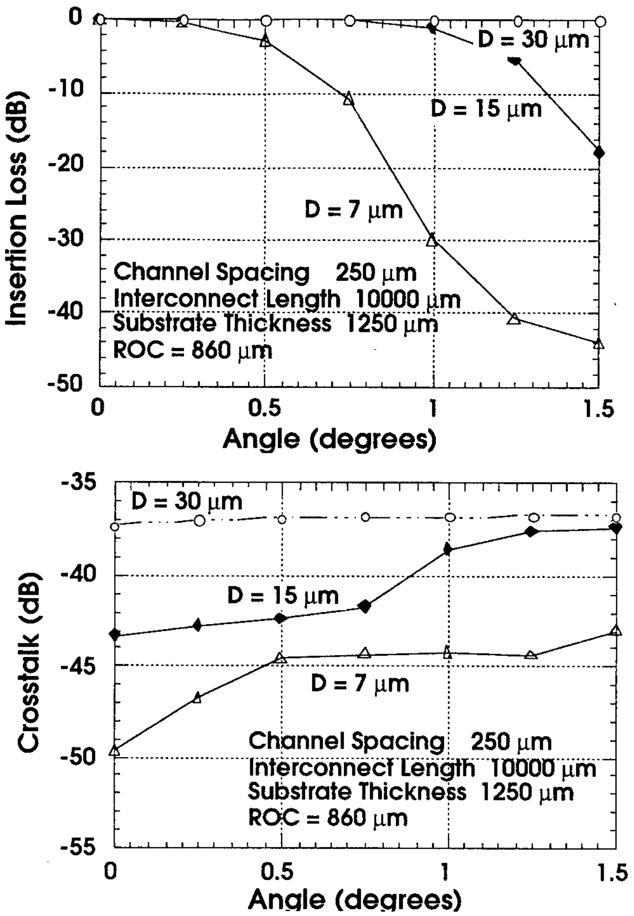

Figure F.2.2: Insertion loss and crosstalk as a function of angular misalignment in the receiver plane.

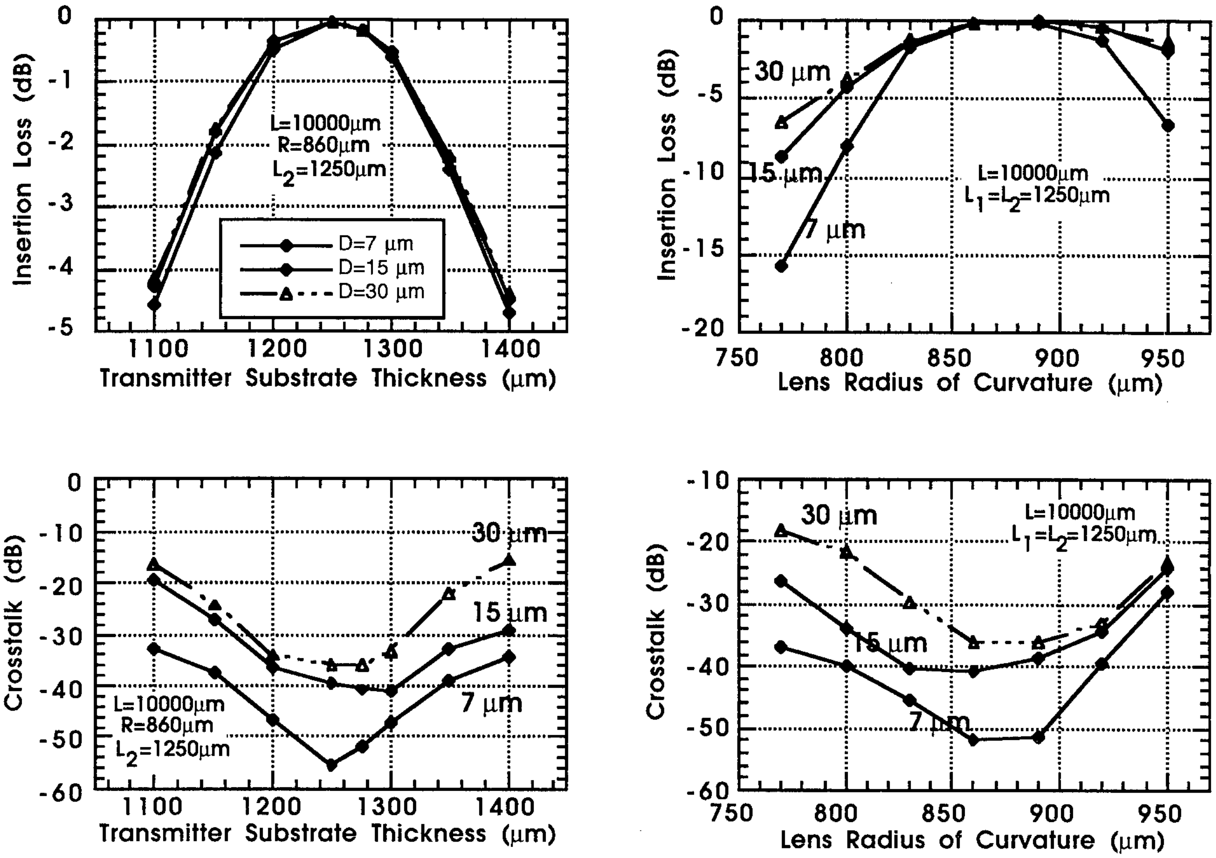

(a) (b)

Figure F.2.3: Insertion loss and crosstalk as a function of (a) substrate thickness and (b) lens curvature.

F.3 SIMULATIONS OF THE EXPERIMENTAL LINK

Our experimental setup has devices baricated on standard 500 μm substrates. Detector diameter is 15 μm. The single mode VCL diameter is 3.1 μm, not small enough to optimize the system for a 10 mm interconnect length. The lens radius of curvature is 295 μm, shorter than required for the "collimated beam" condition (~ 340 μm). As a result, the interconnect length is optimized at 1.7mm, as shown in Fig. F.3.1. However, because of the long confocal region, we can still expect the interconnect to operate well up to at least twice that length. Lateral dependence of the insertion loss is shown in Fig. F.3.2. Tolerance up to ± 70 μm misalignment is expected. However, the experimental results show less than ±30 μm for roughly the same longitudinal placements, as presented in Section J. Finally, the angular misalignment effects with the receiver placed at L = are shown in Fig.F.3.3. For the detector size 15 μm, the system should tolerate a ±2.5° tilt in the receiver plane.

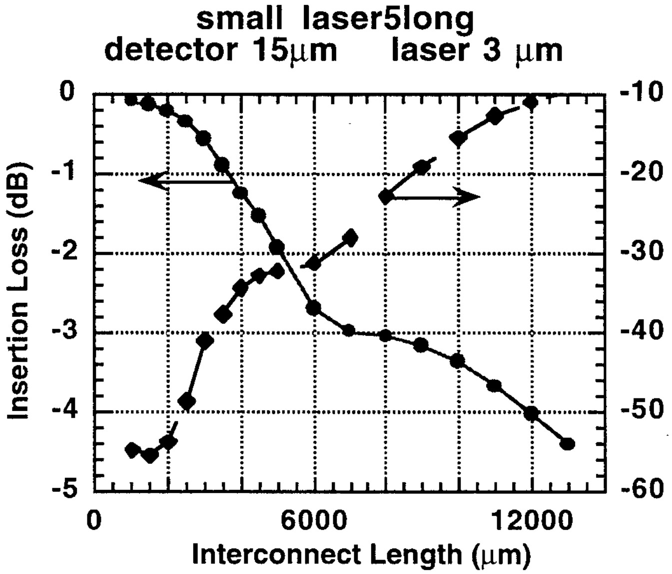

Figure F.3.1: Simulated insertion loss and crosstalk of the experimental setup as a function of longitudinal placement.

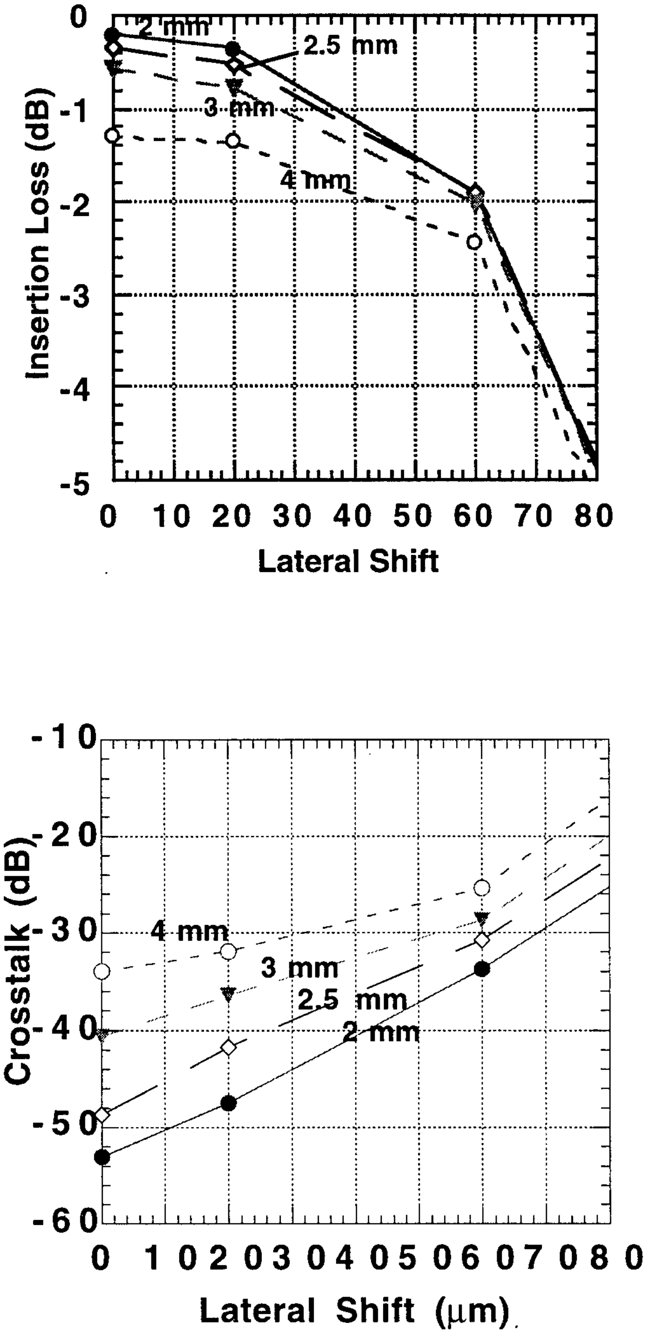

Figure F.3.2: Simulated insertion loss and crtosstalk of the experimental setup as a function of lateral displacement for different longitudinal placements.

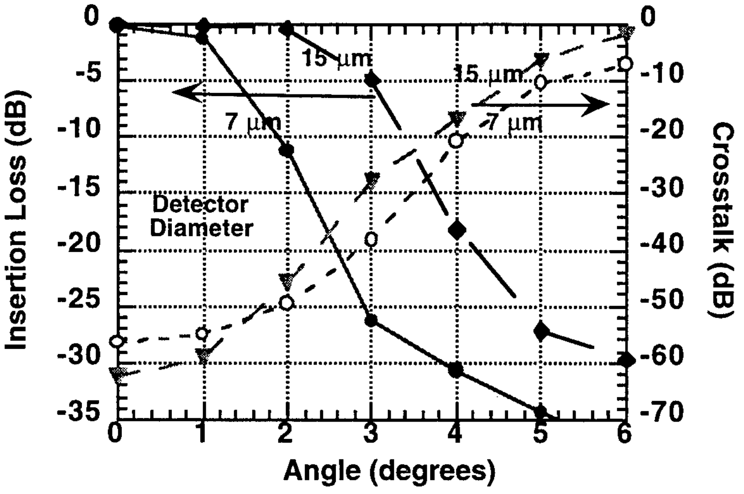

Figure F.3.3: Simulated insertion loss and crosstalk of the experimental setup as a function of tilt angle of the receiver array.

G. FREE-SPACE LINK SIMULATIONS (TIME)

A program was written to simulate optical links. For free-space links, the simulation includes pseudorandom pattern generation, an HSPICE interface allowing accuract simulation of laser driver or receiver circuit, multimode rate equations, optical loss in the free-space system, detector response, and an output filter. The program, including its design and operation, is discussed in more detail in the **APPENDIX**.

The program was used to simulate a free-space link utilizing a three stage CE receiver circuit. This link is the same as the link realized experimentally except for the receiver. The experimental link used a 6 Ghz receiver with an unknown design. The three stage CE receiver circuit should have a similar bandwidth, although the gain will differ from the receiver circuit used in the experiment. The link used a VCL with a threshold current of 270 μA, a resistance of 550 Ω, and a capacitance of 330 fF. The link also used a 15 μm diameter detector and the receiver output was filtered at approximately .7 times the bit rate. Figure G.1 shows the eye diagrams and Figure G.2 shows some of the waveforms from the simulation and experimental measurement of this link at a bit rate of 2.5 Gbit/s.

Comparing the results of the experimental link and those from the link simulation, it can be seen that they are very similar. The measured eye contains noise and has a longer word length, and therefore more traces, than the simulated eye. With noise and a longer word length, it appears that

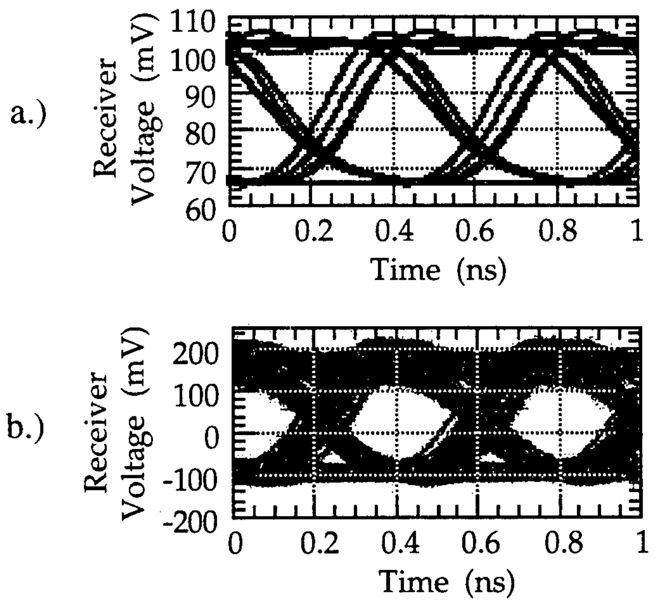

Figure G.1: Eye diagrams of (a) the simulated and (b) the experimental free-space link at 2.5 Gbit/s. The links used 270 μA threshold VCLs and 15 μm diameter detectors. The receiver outputs were filtered at approximately .7 times the bit rate and both receivers had bandwidths of approximately 6 Ghz. The receiver gain was different for the simulation and experiment.

the simulated eye diagram would fill in and look more like the measured eye diagram. Both the measured and simulated eye diagrams exhibit similar pattern dependent effects and relaxation resonances. As can be seen from the simulated laser power in Figure G.2b, a significant overshoot is expected at the beginning of pulses. These optical power overshoots can be observed experimentally by looking at the measured receiver voltage before the filter, Figure G.2d. The measured overshoots in the receiver voltage are not as large as those for the laser power. This is to be expected however since the receiver pre-amp only has a 6 Ghz bandwidth and will therefore filter out higher frequencies in the received pulses. If the waveform from the laser were filtered at 6 Ghz, the overshoots could then be compared quantitatively. The differences between simulated and experimental receiver gains also makes quantitative comparisons difficult.

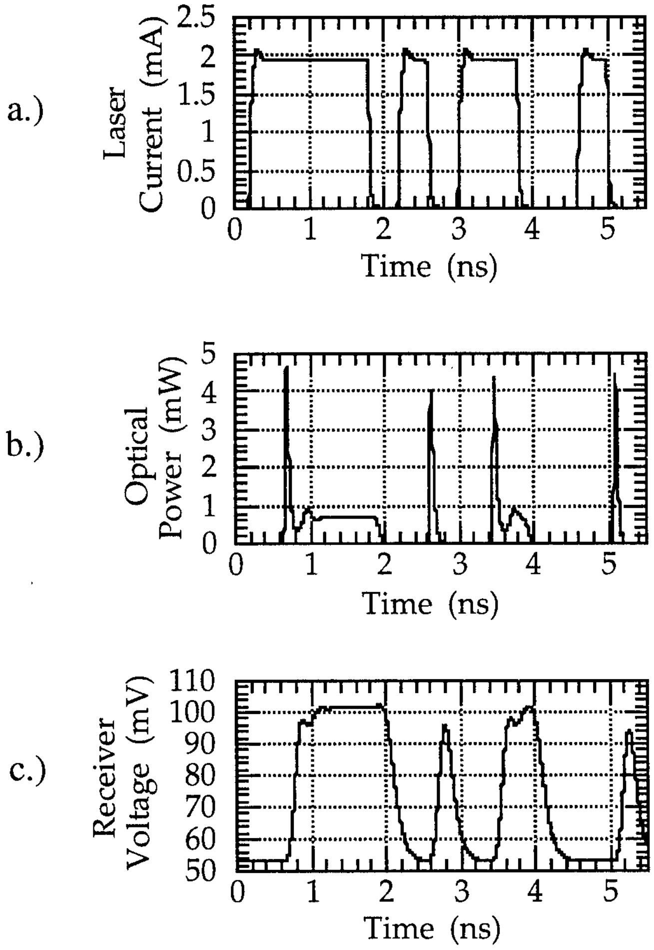

Figure G.2: Waveforms of the a.) laser current, b.) laser optical power, and c.) the filtered receiver voltage of the simulated free-space link at 2.5 Gbit/s. The link used a 270 μA threshold VCL and 15 μm diameter detector. The receiver output was filtered at .7 times the bit rate and the receiver had a bandwidth of approximately 6 GHz.

d.)

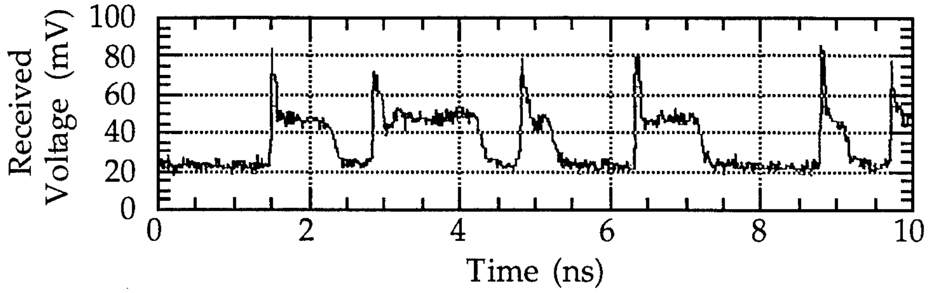

Figure G.2d: Measured waveform of the unfiltered receiver voltage for the experimental free-space interconnect at 2.5 Gbits/s. The link used a 270 μA threshold VCL and 15 μm diameter detector. The receiver output was filtered at .7 times the bit rate and the receiver had a bandwidth of approximately 6 GHz.

H. DRIVE CIRCUITS

With the low drive currents required for current VCLs, the possibility arises to use simple laser driver circuits that have very low power dissipation. These simple circuits dissipate low powers because they contain few transistors and do not bias the VCL at threshold. Instead, the circuits use feedback to bias the lasers somewhere below threshold without additional bias circuitry. Simple laser driver circuits, consisting of 1 to 3 HBTs, were investigated. These circuits hold promise for providing low power laser drivers that can operate in the Gbit/s range. These circuits were simulated driving a 300 μA threshold VCL with a resistance of 50 Ω. The circuits were designed to provide a current gain of 20 A/A corresponding to an on current of 1 mA.

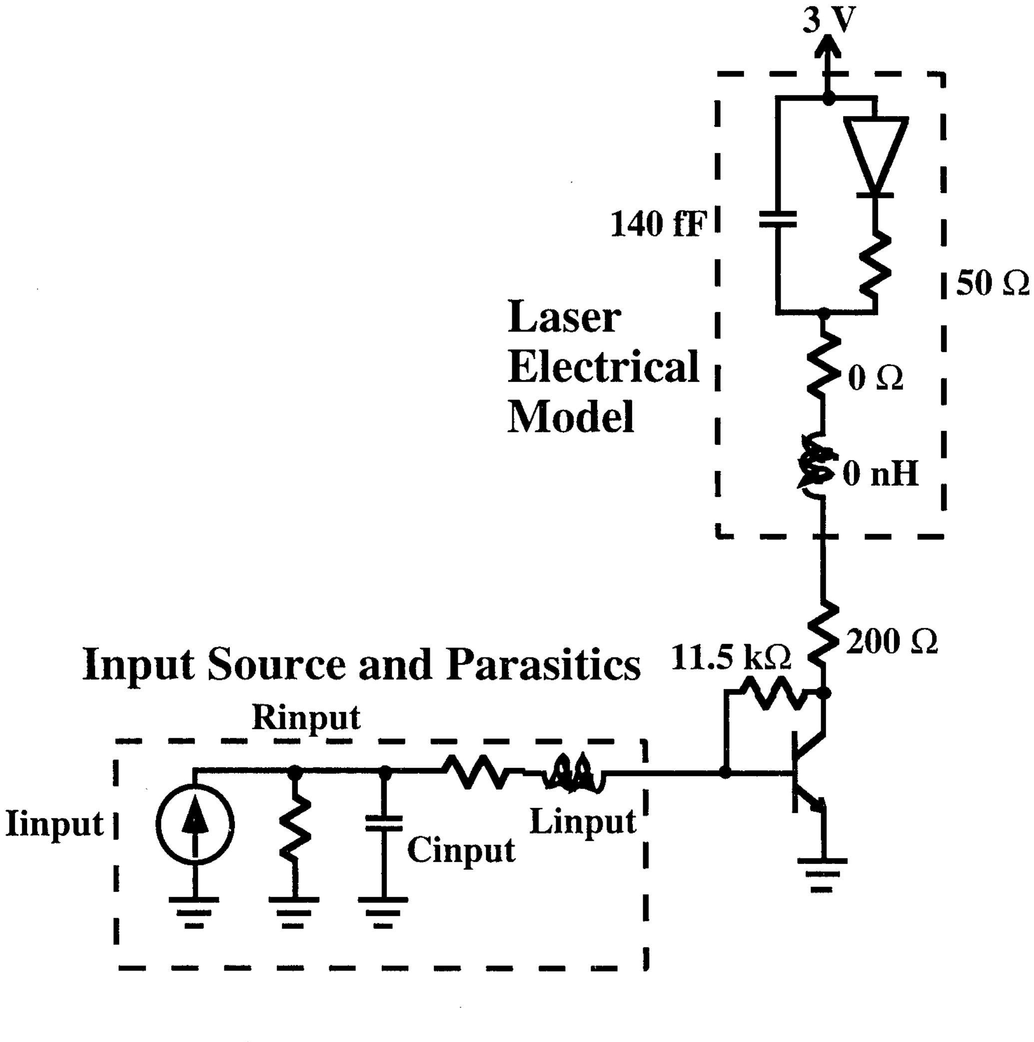

Figure H.1: Circuit diagram of single stage common emitter HBT transimpedance amplifier designed to maximize speed and minimize power while providing a current gain of 20 A/A. The circuit was optimized for a laser threshold current of 300 μA.

A laser driver consisting of a single transistor in a common emitter (CE) configuration is shown in Figure H.1. This circuit was found to have a latency of 123 ps and an average power consumption of 1.6 mW. A two transistor Darlington pair laser driver circuit is shown in Figure H.2. This circuit had an average power consumption of 4.9 mW and a latency of 34 ps. Figure H.3 shows a three stage CE laser driver. This circuit was found to have a latency of 60 ps and an average power consumption of 3.9 mW.

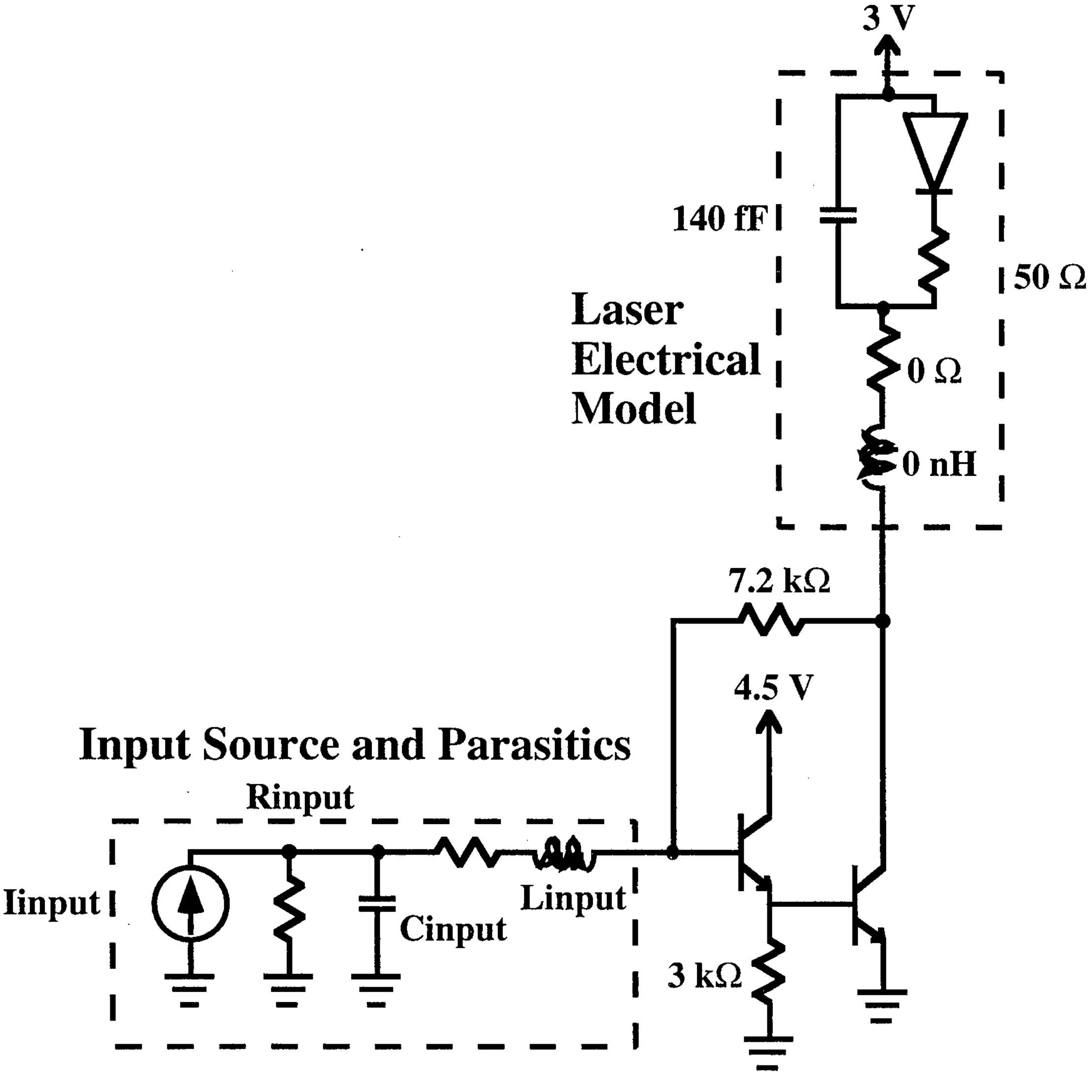

Figure H.2: Circuit diagram of a Darlington pair HBT transimpedance amplifier designed to maximize speed and minimize power while providing a current gain of 20 A/A. The circuit was optimized for a laser threshold current of 300 μA.

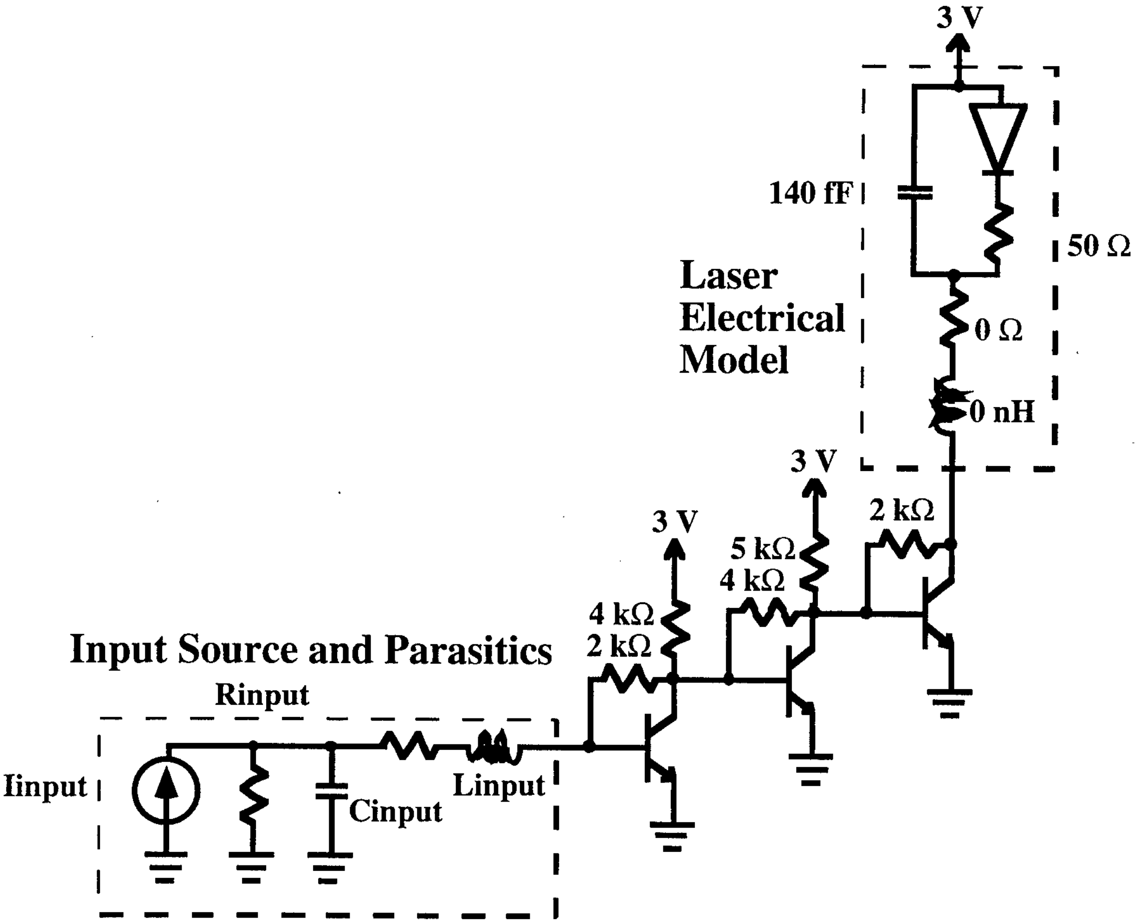

Figure H.3: Circuit diagram of a three stage common emitter HBT transimpedance amplifier designed to maximize speed and minimize power while providing a current gain of 20 A/A. The circuit was optimized for a laser threshold current of 300 µA.

Figure H.4 summarizes the results of these circuit simulations. The Darlington pair had the greatest flexibility of the circuits. The circuit latency can be decreased with an increase in the circuit's power consumption by lowering the value of the bias resistor. The off current bias level can also be adjusted independently. With proper design, it was found that the Darlington pair could have a combined circuit latency and laser turn-on delay of less than 50 ps. For a free-space interconnect with a board to board spacing of 1 cm, the propagation delay from board to board is about 33 ps. This means that the Darlington pair could be used in an interconnect with a total board to board delay of about 80 ps. These results show that a free-space interconnect using a Darlington pair laser driver and a low impedance, sub-milliamp threshold VCL could be operated at 10 Gbit/s. One disadvantage of the Darlington pair is its inability to drive high impedance VCLs without a great reduction in performance. When the resistance of the VCL reaches 200 Ω, the

Darlington pair virtually stops working. For this reason, there may be difficulty employing the Darlington pair for very low threshold devices until the impedances can be reduced.

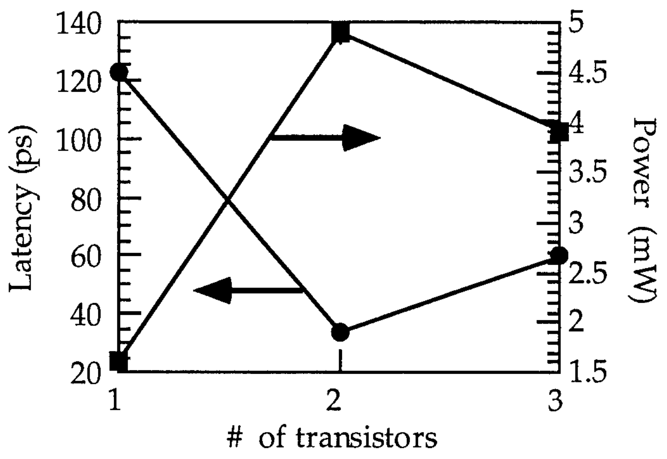

Figure H.4: Summary of the simulation of simple HBT laser driver circuits. The circuits were optimized to minimize power and maximize speed while providing a non-inverting current gain of 20 A/A. The VCL was assumed to have a threshold current of 300 μA.

The one stage and three stage CE laser driver circuits do not experience this same problem with laser resistance. These circuits can be designed to work well for both low and high impedance VCLs. The single stage CE circuit has a more limited current drive capability and is probably best utilized when power is more of an issue than speed. The three stage CE laser driver has much better current drive capability but still exhibits low power dissipation. For higher impedance VCLs (>200 Ω), the three stage CE circuit is the best choice.

I. FLIP-CHIP BONDING AND DEVICE MOUNTING

I.1 FLIP-CHIP BONDING

Flip-chip bonding was used to integrate linear arrays of VCLs onto submounts containing coplanar transmission lines that could be used to either test the devices high-speed or wire bond them for use in a free-space system. The VCLs used were either back-side contacted or double intra-cavity contacted devices with a center to center spacing of 250 μm. The VCLs were integrated with microlenses and were diced into arrays containing 12 devices. For the back-side contacted VCLs, gold was electroplated over the pillars and In bumps were thermally evaporated onto the gold. For the double intra-cavity contacted VCLs, bonding pads were placed on either side of the laser pillar and circular In bumps were thermally evaporated onto these bonding pads. The In bumps were 30 μm in diameter and about 6 μm in height, compared to a VCL pillar height of about 5 μm. Matching In bumps of approximately the same height were put on the submount. The submount consists of Ti/Au evaporated onto SI GaAs to form a coplanar transmission line fan-out pattern for 12 devices. A diagram of the submount is shown in Figure I.1.

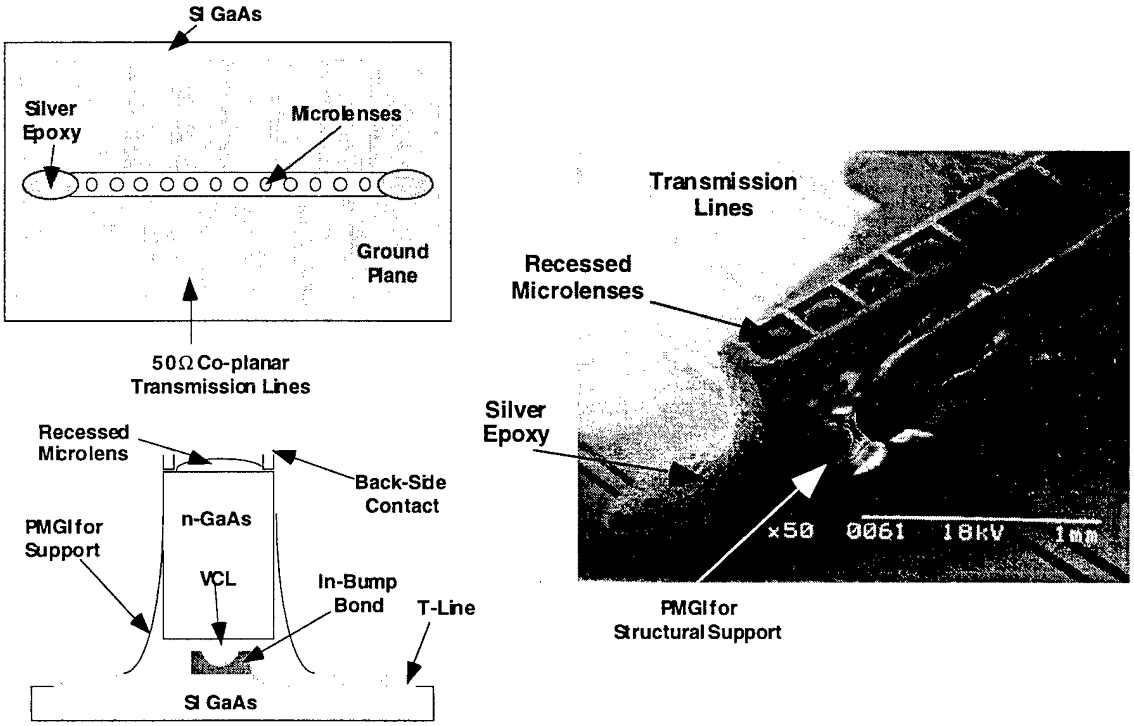

Figure I.1.1: Diagram of the submount consisting of a fan out pattern of 50 Ω coplanar transmission lines on SI GaAs. An array of 12 VCLs were flip-chip bonded to this submount.

The flip-chip bonding was performed using a Research Devices M-8A flip-chip aligner bonder to precisely align the corresponding In bumps on the VCL array and on the submount. The two pieces were then pressed together with a bonding mass of 40 to 50 g, compressing the In bumps. The bonding pressure was maintained for approximately 1 second and no heating was used during the bonding process. After the bonding was completed, PMGI resist was flowed under the laser array and cured to provide mechanical support.

Arrays of VCLs were successfully bonded and continued to have good characteristics. Figure I.2 shows L-I and V-I characteristics of a VCL after flip-chip bonding. The VCL was tested cw at room temperature.

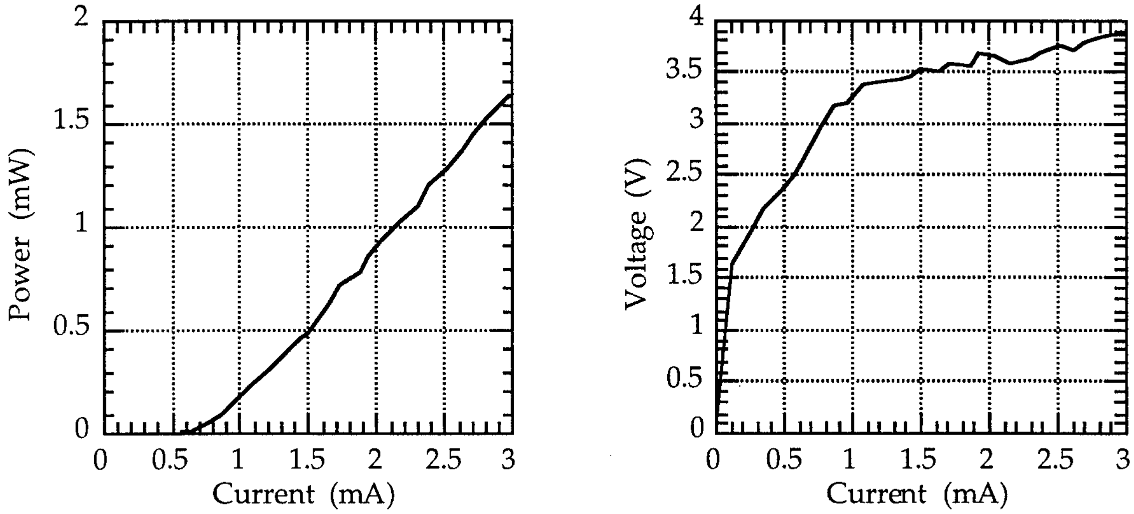

Figure I.1.2: L-I and V-I of a VCL after it has been flip-chip bonded illustrating that the device continues to have good characteristics. This VCL has a diameter of approximately 6 μm.

Arrays of photodetectors with microlenses were also successfully bonded to submounts. The submounts for the detectors had one In bump per device and the bumps were of the same dimensions as the ones used for the VCLs. However, since the detectors were recessed and couldn't be physically damaged during the bonding process, the bonding mass was increased to about 150 g. Otherwise, the bonding process was the same as for the lasers.

I.2 DEVICE MOUNTING FOR FREE-SPACE OPTICAL LINK

The free-space optical link experiment required the ability to move the transmitter and the receiver arrays with respect to each other to study the effects of longitudinal, transverse, and angular misalignments. The devices required a DC bias as well as a high-speed signals interface to test the BER of the link. A side view schematic of the experimantal setup is shown in Fig. I.2.1. The diced chips holding lensed VCLs and detectors are flip-chip bonded on SI-GaAs submounts patterned with coplanar 50 Ω transmission lines. The transmission lines fan out from the device array with devices on 250 μm pitch to the edge of the submount where their width is 75 μm. This is barely wide enough to place a wire bond ball. The submount dimension are 6mmx8mmx0.5mm. The submounts are placed on connectorized mounting fixtures that can be subsequently mounted on xyz translation stages and a set of goniometers and a rotation stage that provide 6 degrees of freedom for machanical misalignment tests.

The mounting fixture is equipped with an alumina board patterned with 50 Ω transmission lines, designed for 10 GHz operation, that fan out from the submount position to the SMA connectors. Its top view design is shown in Fig. I.2.2. The board is narrower in the submount region to test short interconnect lengths while allowing a wide angular misalignment range. The submount is glued to the alumina board. The transmission lines on the submount and the board are connected by Au wire bonds. Six devices in a row can be potentially tested at the same time.

The electrical characteristics of the mounted devices are tested in a network analyzer. Small VCLs have input impedances on the order of 200-250 Ω. This impedance mismatch with the 50 Ω transmission line is compensated by placing a chip resistor in shunt with the device. The single mode oxide aperture VCLs required a 56 Ω resistor.

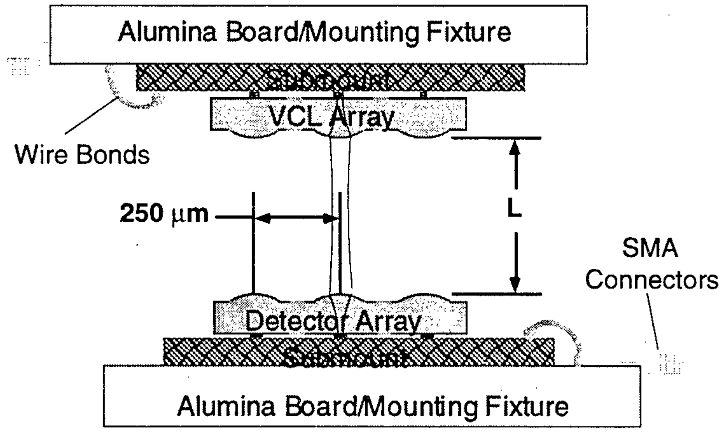

Figure I.2.1: Side view of the test fixtures for the optical interconnect link. Note the absence of external optics.

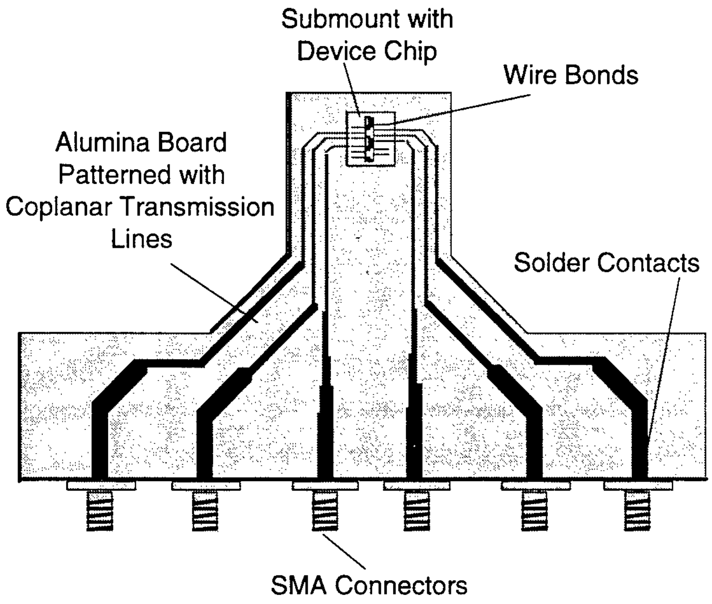

Figure I.2.2: Top view of the alumina board pattern.

J. FREE-SPACE OPTICAL LINK MEASUREMENTS

J.1 MEASUREMENTS OF ALINGMENT TOLERANCES

The beam profile from the lensed VCL with a microlens of focal length 127 μm (in air) and 477 μm (in semiconductor) is expected to have low divergence, with the waist positioned ~1.2 mm from the surface and a confocal region length of ~2.5 mm. The uncertainty of this estimate is due to the uncertainties in evaluating the laser's initial waist and also the wafer thickness and lens curvature. Variation in any of these parameters will vary the position and value of the beam waist in the free-space beam. Assuming the laser's waist 1.5 μm the beam far-field divergence half angle in air is ~12°. With a collimating microlens, allowing for some parameter variation, we expect the far-field half angle to be reduced to between 0.5° and 2.1°.

The angular beam profile of the mounted single mode lensed VCL was measured at several radial positions from the microlens by scanning a single mode fiber (single mode for λ = 980 nm) on an spherical surface. These measurements are shown in Fig. J.1.1. We have experimentally observed that the waist position (maximum coupled intensity for no angular or translational deviation) was somewhere between 2 mm and 2.5 mm from the microlens, which is further than expected from the simulations. The positions of radial scans were beyond that waist position and extended from z = 2.95 mm to 13 mm from the microlens. The half angles ($1/e^2$ of intensity) first increase with increasing z then decrease and saturate at a value ~1° for z > 10 mm. The two measurements furthest from the microlens coincide with each other and can be considered far-field profiles where the beam waist can be approximated as a point source and the fiber traces along the wavefront. From these measurements the waist in air is found to be ~18 μm with the confocal region length of ~2 mm. The increase of width of the measured angular profile is expected near the edge of the confocal region since this is where the beam radius of curvature is smallest. The beam waist has to be considered as an extended source from which the light can couple into the fiber positioned at larger angles. However, this measurement may be inaccurate because the small numerical aperture of the single mode fiber begins to limit the measurement of actual intensity. When the fiber is positioned within the confocal region the angular scans are more difficult to interpret since the fiber position relative to the microlens is not very accurate. Furthermore, the beam's increasing radius of curvature does not match the curvature of the sphere along which the fiber travels (the center of curvature was positioned in the plane of the microlens), and small angular deviations correspond to translations that are large relative to the beam size.

Lateral beam scans at different z positions, are shown in Fig. J.1.2. One curve is near the confocal region (1.45mm from waist, or 2.95mm from lens). The 3dB beam radius in this plane is

31 μm. Assuming a beam waist of 18 μm from the far-field measurement, the beam waist position is $z \approx 1.5$ mm from the microlens, in reasonable agreement with the predicted value.

The far-field angular scan is shown again in Fig. J.1.3 on an expanded scale. It exhibits a somewhat asymmetric profile with a full width at $1/e^2$ of ~ 2°, close to the expected value for the parameters of the VCL, substrate thickness and lens curvature. The beam has some side lobes possibly due to diffraction or due to some local defects in the lens surface. These defects were formed at the perimeter of the lens during the RIE step of lens fabrication, as described in Sections D and E. They are a result of sputtering of exposed back side contact metal that was partly covered with photoresist during the etch. However, the side lobes are down by -25 dB relative to the peak power and should not have a detrimental effect on the system performance.

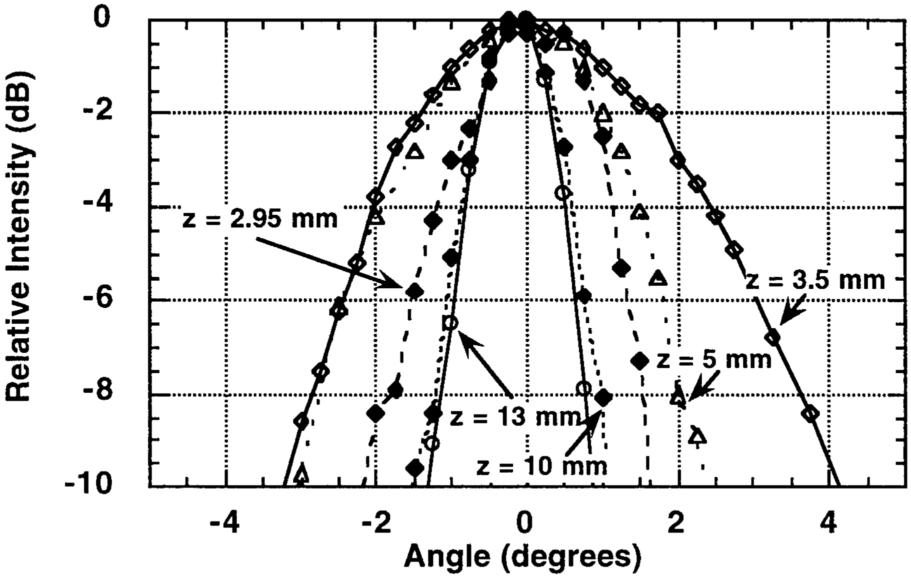

Figure J.1.1: Angular beam profiles of a single mode lensed VCL measured with a single mode fiber at different distances from the microlens. The far-field half angle is 1°.

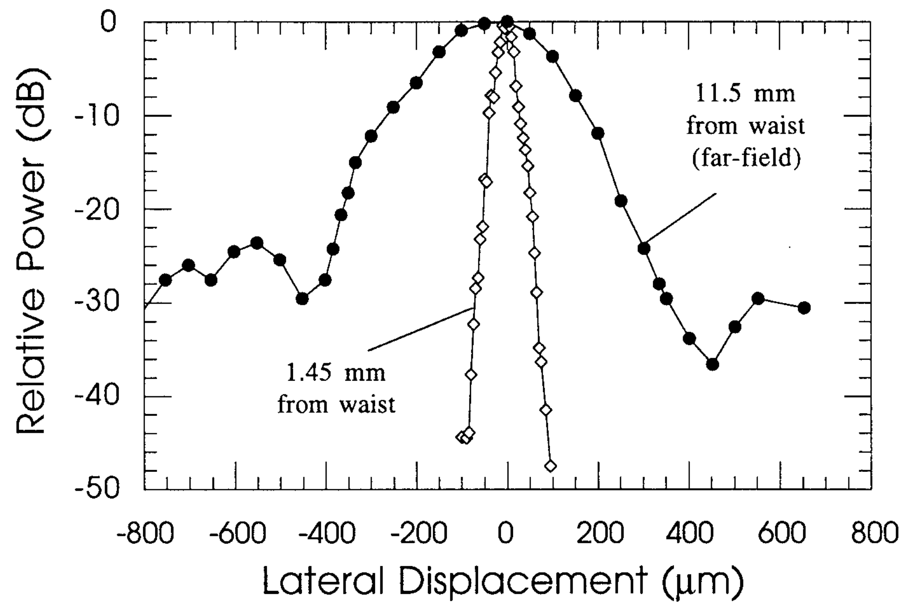

Figure J.1.2: Lateral beam profile of a single mode lensed VCL measured with a single mode fiber. The beam waist is ~1.5mm from the microlens.

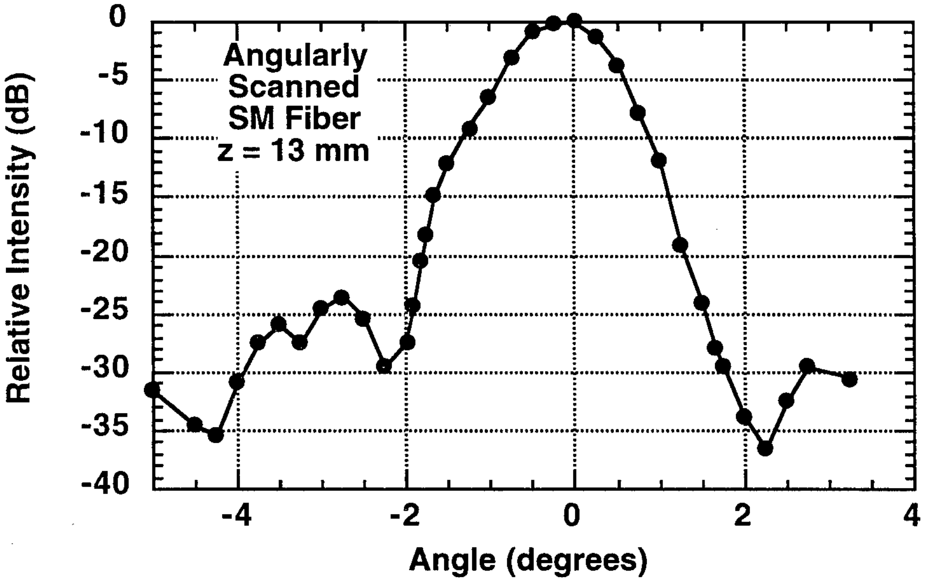

Figure J.1.3: Beam profile of a single mode lensed VCL measured with a single mode fiber.

The experimental setup for testing our free-space optical link is shown in Fig. J.1.4. The mounting of the lensed devices was described in Section I. The connectorized boards are mounted on a system of translation and tilt stages for testing the mechanical misalignment of the system. In most of our measurements the VCLs were biased to operate with square pulses in ON/OFF mode, i.e. with very high extiction ratios. Therefore, the received optical power can be found by measuring the DC photocurrent (after subtracting the dark current). We have measured the extinction ratio by observing the received pulses on a sampling scope.

Figure J.1.5 shows the relative insertion loss as a function of lateral and longitudinal misalignment. The measurement at $z = 2$ mm is believed to be very close to the beam waist. Other scans are within or close to the confocal region. At a given longitudinal placement, the insertion loss drops by 3 dB for lateral misalignments of ±30 μm. This is about half of what was expected from the simulations shown in Section F. The discrepancy could be partially due to an inaccurate assumption of the VCL beam profile and the assumption of a spherical lens surface for the simulations. With longitudinal position changing from $z = 2$ mm to 4 mm the maximum intensity drops by more than 3 dB. The drop is due to the receiver lens being moved beyond the confocal region where the beam begins to spread significantly. However, the rate of the intensity drop with z is twice as high as expected from the simulations.

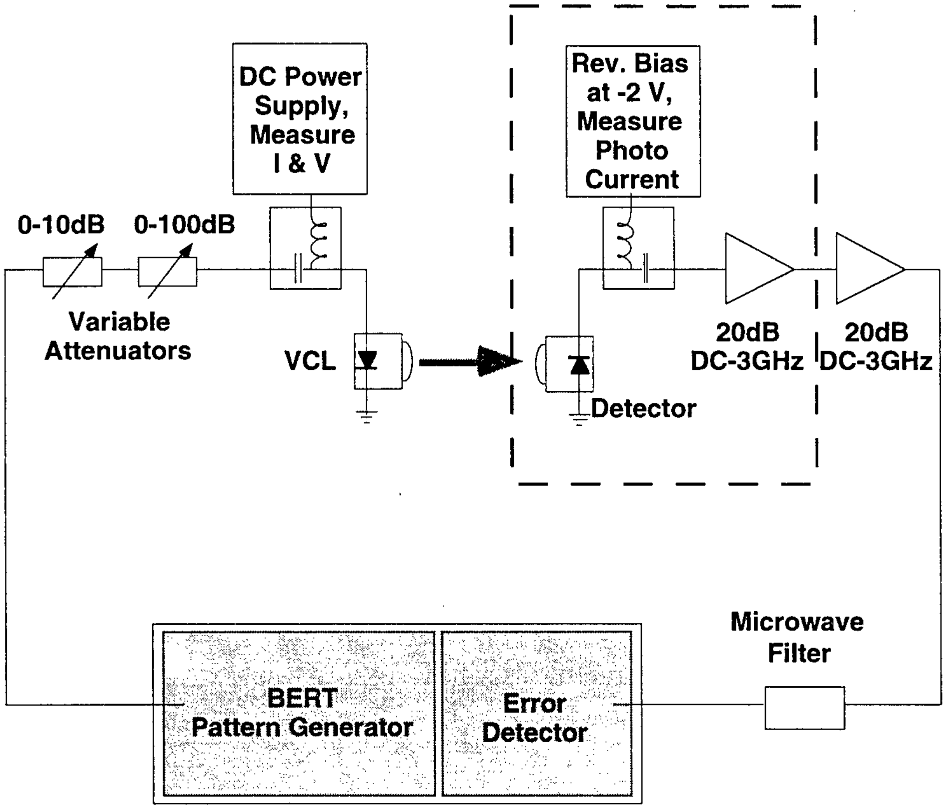

Figure J.1.4: Schematic of test set-up.

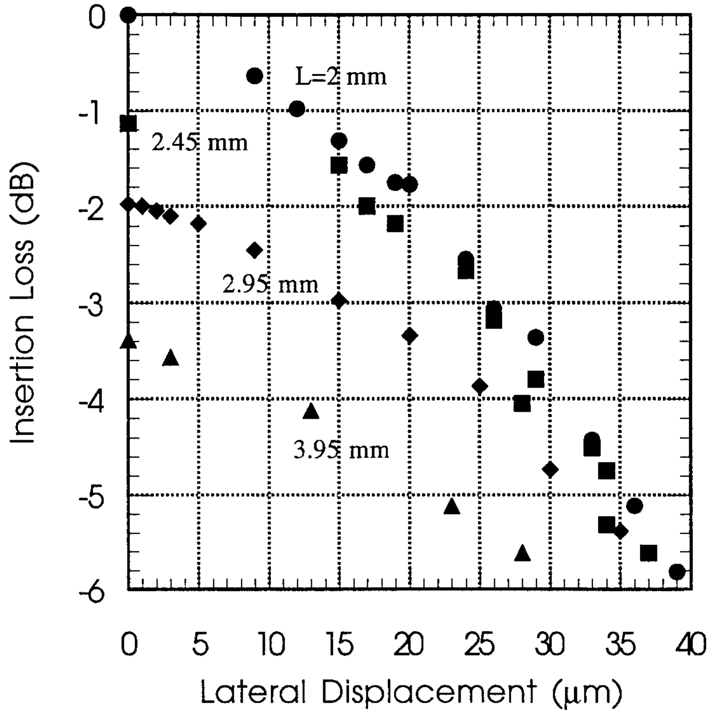

Figure J.1.5: Measured insertion loss vs lateral displacement of the free-space optical link, for different interconnect lengths.

J.2 BER MEASUREMENTS

To demonstrate high speed application of the link we have measured BER as a function of received optical power. The tests of BER as a function of received power were done by misaligning the link laterally at a longitudinal placement of the receiver array of 2.45 mm to maintain constant extinction ratio. We have achieved BER lower than 3×10^{-11} at 3 Gbit/s and a word length 2^{15}-1 for receiver power > 6.7 dBm. This relatively large value of necessary power can be attributed to our photodiodes which were not fully optimized. Fig. J.2.1 shows the BER at 3 Gbit/s as a function of received power. No error floor was detected. The BER degradation for lower powers is due to insertion loss increase only. Figure J.2.2 also demonstrates good open eye patterns of the free-space link at 2 Gbit/s and at 3 Gbit/s. These patterns were measured with a low noise New Focus receiver with 6 GHz bandwidth.

The free-space system's (Fig. J.1.4) high speed performance has also been characterized with respect to mechanical misalignments. The degradation of the BER with lateral and longitudinal misalignment is shown in Fig. J.2.3. As expected, the system is far more sensitive to lateral than to longitudinal displacements. A system with a maximum error rate of 10^{-9} would tolerate ± 18 μm of lateral displacement at z = 2.45 mm, while the longitudinal displacement could be varied by about ± 250 μm. For larger lateral displacements the beam spot focused in the detector plane moves off from the detector area (diameter 15 μm) causing increased insertion loss and consequently increased error rate. In case of longitunal displacement within the confocal region, the insertion loss drops slowly with displacement, as shown in Fig. J.1.5 and in Section F, due to the low divergence beam.

From the insertion loss vs displacements and BER vs power characteristics, we can generate design curves of the free-space optical link, as shown in Fig. J.2.4. In this plot the measured data points were taken at z = 2.45 mm (as in Fig. J.2.3) with maximum receiver power of -6.5 dBm for no lateral displacement. We have observed no error floor below BER = 3×10^{-11}, suggesting that if we simply increase the system's power margin, a larger lateral displacement could be tolerated. For example, with the maximum received power increased by 6 dB, the lateral displacement tolerance could be increased from ±18 μm to ±49 μm for a system a with maximum error rate of 10^{-9}. On the other hand, with the power reduced by 2 dB, the misalignment tolerance becomes only ± 6 μm, unbearably tight for a free-space system design.

In summary, we have demonstrated lensed VCL and photodiode arrays in a free-space optical link applicable to computer board-to-board interconnects. Link operation at 3 Gbit/s with no error floor has beed demonstrated for ON/OFF modulation. The system's mechanical tolerances have been characterized.

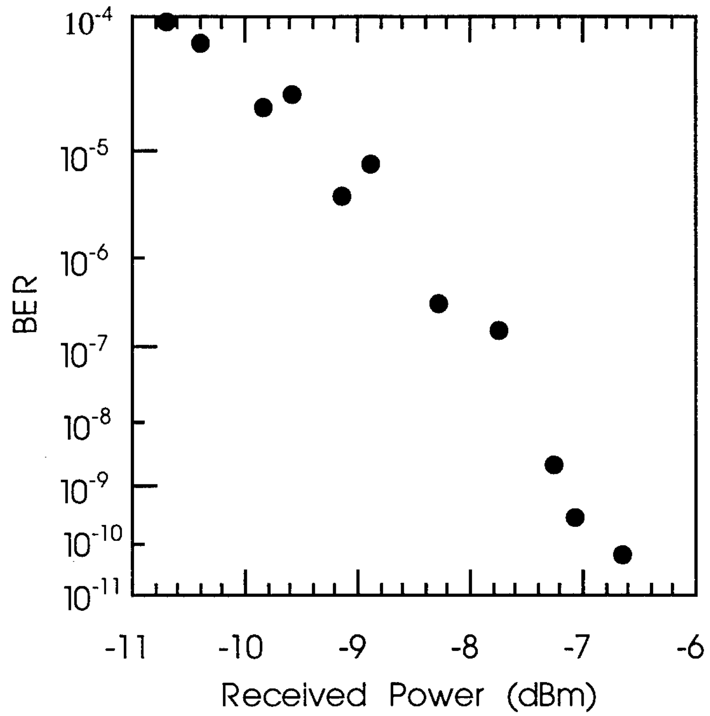

Figure J.2.1: BER vs received power at 3 Gbit/s at longitudinal placement 2.45 mm and no lateral displacement.

a.)

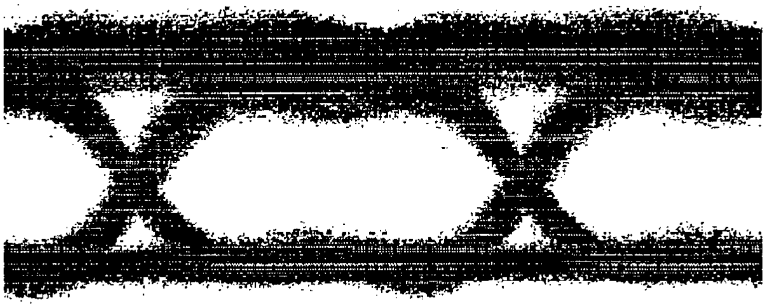

b.)

Figure J.2.2: Eye diagrams of the free-space link at a.) 2 Gbit/s and b.) 3 Gbit/s. Measured with a New Focus receiver with 6 GHz bandwidth.

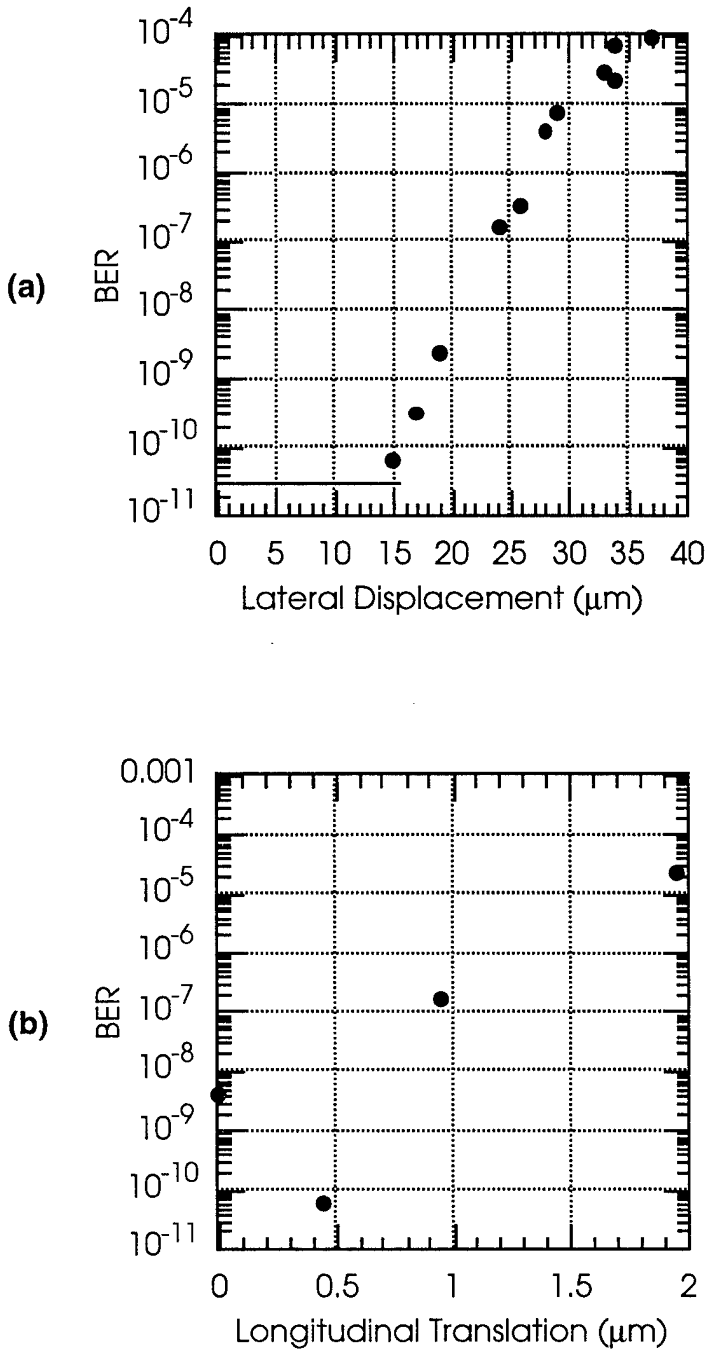

Figure J.2.3: a.) BER at 3 Gbit/s vs lateral displacement at L = 2.45 mm and b.) BER at 3 Gbit/s vs longitudinal displacement with a lateral displacement of 15 μm for relative longitudinal displacements begining from L = 2 mm. The maximum received power without displacement is -6.5 dBm.

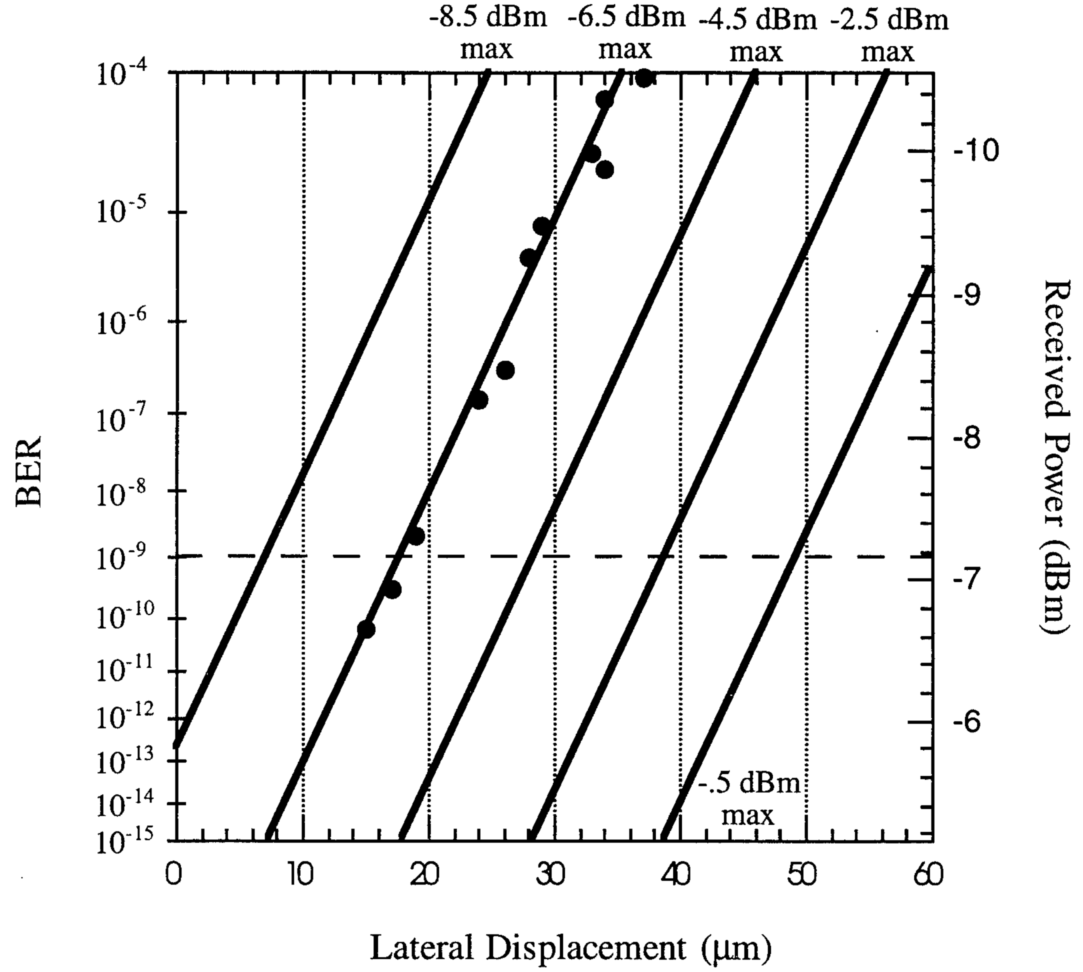

Figure J.2.4: Design curves for a free-space optical link operating at 3 Gbit/s, including experimental data.

APPENDIX. AFOSR FINAL REPORT

APPENDIX.1 INTRODUCTION

This report will review the work completed under AFOSR. The goal of this project has been to develop microlenses on the back-side of Vertical-Cavity Lasers (VCLs) and use them in a free-space link. In the process, it was also realized that a simulation program was necessary to evaluate the link. In this final report we briefly review the microlens work and then focus on detailing the link simulator.

The link simulator program was written in ANSI C, but interfaced with HSPICE, a commercial circuit simulation package, to allow accurate analysis of the laser driver and/or receiver circuit as well as the laser and detector parasitics. Using the program, signals can be traced as they propagate through the link. This not only provides information about the link's performance, but also about link components and their interactions. After describing the program's structure and operation, simulation results will be presented.

Two students were involved in this work - Eva Strzelecka and Duane Louderback. Ms. Strzelecka focused on the microlenses and Mr. Louderback worked on the link simulator. Ms. Strzelecka will be finishing her Ph.D. by early 1997 and Mr. Louderback is in an earlier stage of his Ph.D. work.

APPENDIX.2 Micro-Lensed VCSELs

Wafer-level integration of optoelectronic devices with microlenses will result in components that can be used directly in systems, without external optics. Combinations of vertical-cavity surface-emitting lasers (VCSELs), LEDs, or detectors, with microlenses have applications in optical fiber systems, free-space interconnections, displays, printers, etc. Refractive lenses, etched in the back side of the substrate, have several advantages over diffractive lenses. Besides the simple and manufacturable fabrication technology, the lens optical efficiency is primarily limited by the absorption of the substrate, which is nominally transparent. Furthermore, these lenses are far less sensitive to wavelength variations. We present a process for fabricating refractive microlenses in GaAs and InP with the ability to control the radius of curvature (ROC) within ±10%, suitable for many practical applications.

Our microlens fabrication requires transfer of a lens-like shape of patterned, reflowed photoresist[1] into the semiconductor by anisotropic dry etching. We chose reactive ion etching (RIE) over etching with inert ions to achieve faster etch rates and a controllable ratio of the etch rate in the semiconductor to that in the erodable mask material[2]. The latter allows precise control of the lens shape. The lens ROC is primarily controlled by the shape of the mask material. The initial thickness and diameter are of most importance. The initial thickness of the resist is adjusted by controlled etchback in oxygen RIE, after patterning. The semiconductor in the field is etched to form a pedestal, prior to reflow of the resist, in order to create surface tension that prevents the resist from spreading in subsequent reflow, and to preserve the lithographically defined diameter. The polyimide PMGI, used as an erodable mask, forms a nearly-spherical shape after reflow. Finally, the lens shape is transferred to a GaAs substrate in Cl_2 RIE. The final lens shape strongly depends on the ratio of etch rate in the GaAs to that in the PMGI. Two *in-situ* optical monitors in our RIE reactor allow us to control the etch rate ratio thereby achieving a desired curvature and correcting for aberrations. The etch rate of GaAs increases with pressure, due to the increasing chemical nature of the process, whereas the PMGI etch rate remains fairly constant (Fig. APP.2.1). The bias voltage proportionately increases the etch rate of both materials. The etch rate of GaAs is about 1.5 to 3 times faster than PMGI. Under typical conditions (2 mT and 350 V bias), the etch rates of GaAs and PMGI are 220, and 110 nm/min, respectively. The initial resist mask is usually thinner than the final GaAs lens, as determined by profilometer scans (Fig. APP.2.2). A similar process for InP microlenses in BCl_3/Cl_2 chemistry has been also developed.

For integration with devices, the lens is recessed into the wafer (Fig. APP.2.3) for lens surface protection and contact metallization. Integration of GaAs lenses with single mode VCSELs has resulted in reducing the laser's far-field divergence half-angle of ~14° to less than 1.1°.

REFERENCES TO APPENDIX.2

[1] Z. D. Popovic, R. A. Sprague, and G. A. N. Connel, *Appl. Opt.*, 21, pp. 1281-1284 (1988)

[2] E. M. Strzelecka, G. D. Robinson, M. G. Peters, F. H. Peters, and L. A. Coldren, *Electron. Lett.*, 31, pp. 724-725 (1995)

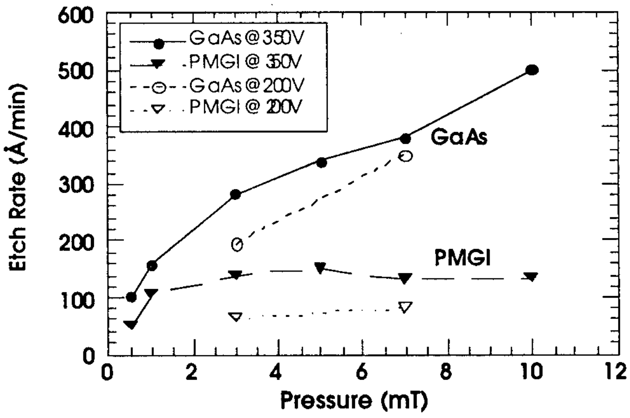

Figure APP.2.1: Etch rates of GaAs and PMGI as a function of pressure and bias voltage in CL_2 RIE.

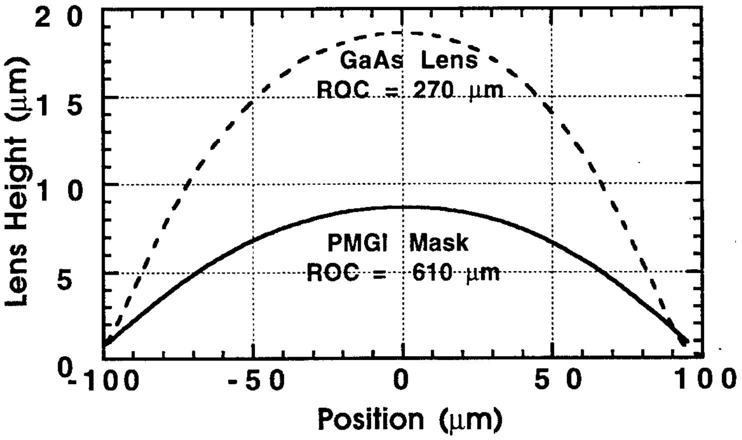

Figure APP.2.2: Surface profilometer scans of the lens-shaped mask before RIE and the GaAs lens after RIE.

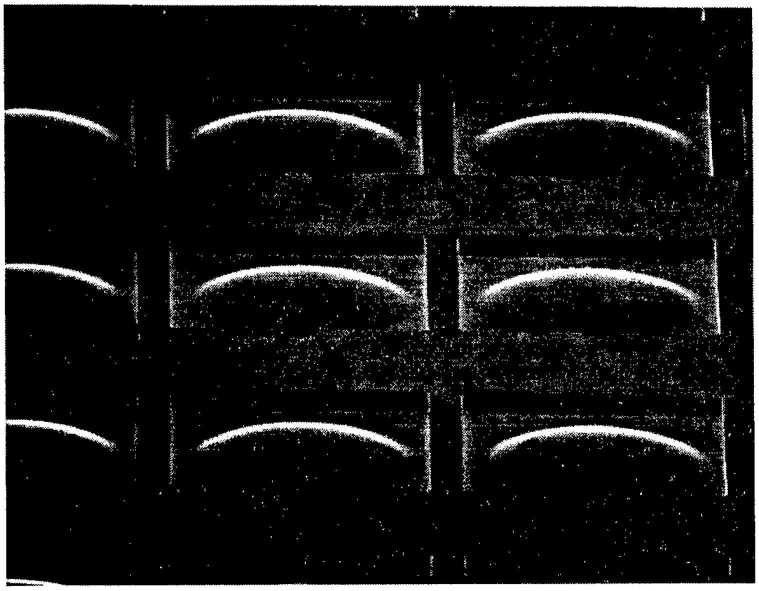

Figure APP.2.3: Scanning electron microscope image of a GaAs lens array recessed in the substrate.

APPENDIX.3 LINK SIMULATOR PROGRAM STRUCTURE

The basic structure of the link simulator is illustrated in Figure APP.3.1. As the block diagram shows, the program starts by creating a pseudorandom input of current pulses. This current waveform is the input signal to either the laser driver circuit or the laser itself if the circuit is included on the receiver end of the system. This part of the simulation is performed by HSPICE and yields the laser voltage and current waveforms. The laser multimode rate equations are then solved under the constraint of the laser current waveform found previously. The rate equations determine the carrier density, optical power, and chirp waveforms. The program then propagates the signal through either free-space or fiber. For a free-space link, only insertion loss is introduced, but for a fiber link, coupling losses, absorption, and dispersion are included. The detector response, excluding the RC response, is then calculated. HSPICE is invoked to perform the simulation of the RC response of the detector as well as the receiver circuit, if there is one. Finally, the receiver current waveform is filtered. An eye diagram is formed and the results are stored in an output file for graphing.

The pseudorandom pattern generator creates a waveform of supergaussian current pulses and stores it in a file for HSPICE and the subsequent electrical part of the simulation. The pulse magnitude, bit rate, word length, and pulse rise times can be specified by the user in an input file.

If a laser driver circuit is included in the link, an HSPICE description of the circuit is stored in an input file. This input file also contains model files for all devices used in the laser driver circuit. Another input file contains laser parameters including those necessary for an electrical model. The electrical model used for the laser, shown in Figure APP.3.2, is composed of a diode with a resistor, capacitor, and inductor included to account for parasitics. The program combines the laser driver circuit description and laser electrical model into an HSPICE input file. The program then runs HSPICE on the input file and retrieves the resulting laser current and voltage waveforms.

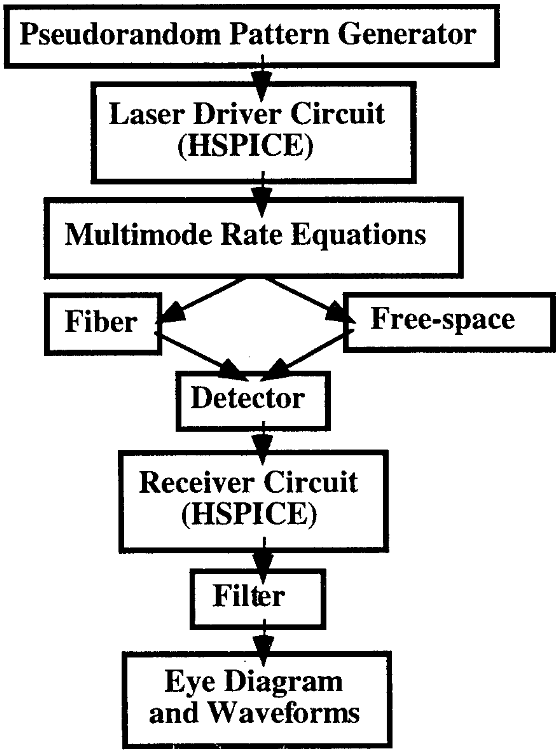

Figure APP.3.1: Block diagram of the link simulator.

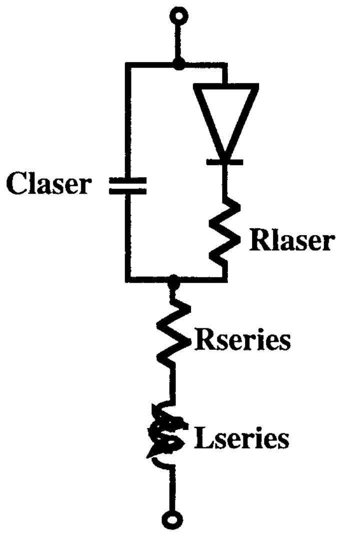

Figure APP.3.2: Electrical model of the laser used in the link simulator.

The laser's multimode rate equations must be solved, consistent with the laser's current waveform, to ascertain the optical power, carrier density, and chirp waveforms. All required laser parameters are contained in an input file. The multimode rate equations are

$$\frac{dN(t)}{dt} = \frac{\eta_i I(t)}{qV} - AN(t) - BN(t)^2 - CN(t)^3 - \sum_m v_{gm} g_m N_{pm}(t)$$

$$\frac{dN_{pm}(t)}{dt} = \left[\Gamma_m v_{gm} g_m - \frac{1}{\tau_{pm}}\right] N_{pm}(t) + \Gamma_m \beta_{sp} BN(t)^2$$

$$\frac{d\phi_m(t)}{dt} = \frac{\alpha}{2}\Gamma_m v_{gm} a \bullet [dN(t)]$$

$$g_m = \frac{1}{\left(1+\left(\frac{\Delta m}{M}\right)^2\right)} \bullet \frac{g_o}{1+\varepsilon N_p(t)} \bullet \ln\left(\frac{N(t)+N_s}{N_{tr}+N_s}\right)$$

where I(t) is the laser current, N(t) is the carrier density, $N_{pm}(t)$ is the photon density in the mth mode, and $\phi_m(t)$ is the phase of the mth mode. $N_p(t)$ is the total photon density summed over all modes. The gain spectrum is approximated by a Lorentzian where m=0 is the mode with the highest gain and M is the mode number where the gain has fallen to half of its peak value [1].

To solve the rate equations, the program begins by calculating the threshold conditions and initial values for the carrier density and photon densities. Then the differential equations are stepped through, point by point, to solve for the variables' values at each point in time. This method of solving these differential equations requires that the time step is very small, on the order of a few ps. Although the number of points can get quite large, the solution of the rate equations only takes a few seconds typically.

Once the optical power and chirp waveforms have been determined, the optical signal must be propagated through either free-space or optical fiber to the photodetector. In the case of a free-space interconnect, the program includes the coupling loss between the laser and detector. In the case of a fiber interconnect, the program includes coupling loss, absorption, and both first and second order dispersion. This produces the optical waveform that will be incident on the photodetector.

The detector response, excluding the RC response, is calculated next. The RC response of the detector is found through HSPICE. Excluding the RC response, the detector's frequency response is

$$\frac{i(\omega)}{i(0)} = \left[\frac{1}{1-e^{-\alpha L}}\right]\left[\frac{1-e^{-j\omega\tau_e}e^{-\alpha L}}{j\omega\tau_e+\alpha L} + e^{-\alpha L}\frac{e^{-j\omega\tau_e}-1}{j\omega\tau_e} + \frac{1-e^{-j\omega\tau_h}}{j\omega\tau_h} + e^{-\alpha L}\frac{1-e^{\alpha L}e^{-j\omega\tau_h}}{\alpha L-j\omega\tau_h}\right]$$

where τ_e=L/v_e and τ_h=L/v_h. This frequency response is convoluted in the time domain with the detector's dc response, i(0)=R*P, to get the detector current without parasitics. The effects of resistance, capacitance, and inductance are ascertained using HSPICE. HSPICE is used for this part of the response because it depends upon the load impedance the detector sees. The load may just be a resistance. However, if a receiver circuit is included, the input impedance of the receiver circuit becomes the load impedance of the detector. This completes the detector response and allows the detector current waveform to be accurately determined.

The program allows a laser driver circuit and/or a receiver circuit to be included in the link. If a receiver circuit is included, HSPICE is used to simulate it at the same time as the RC response of the detector. As with a laser driver circuit, the circuit description is contained in an input file. The program reads the circuit description and creates the appropriate input files for the HSPICE simulation.

Finally, a low pass filter is applied to the receiver output. An eye diagram of the output current is formed by successively shifting and superimposing the output current waveform. The eye diagram and relevant waveforms are stored in output files for graphing and further analysis.

REFERENCES TO APPENDIX.3

[1] L. A. Coldren and S. W. Corzine, *Diode Lasers and Photonic Integrated Circuits*, John Wiley & Sons, Inc., 1995, p. 214-217, 235.

APPENDIX.4 SIMULATIONS

To demonstrate the operation of the link simulator, it was used to analyze a short distance fiber link using a 980 nm vertical cavity laser (VCL). The VCL had a threshold current of 270 μA and was driven by a three stage common emitter HBT laser driver circuit as shown in Figure APP.4.1. The link also consisted of 2 km of graded index fiber and a small area pin photodetector. A three stage common emitter receiver circuit was used to drive a 50 Ω load and the receiver output was filtered at .7 times the bit rate. The receiver circuit is the same as the laser driver circuit except for the biasing. The waveforms resulting from the link running at 1 Gbit/s are shown in Figures APP.4.2a and APP.4.2b. It can be seen from the waveforms that if the bit rate were increased, pattern dependent effects would begin to appear. Figure APP.4.3 shows eye diagrams of the link's output at 1, 2, 3, and 4 Gbit/s. At the higher bit rates, pattern dependent effects can be seen in the eye diagrams, resulting in eye closure. From the eye diagrams, it appears that this link could probably be operated at up to 3 Gbit/s while still maintaining a low bit error rate.

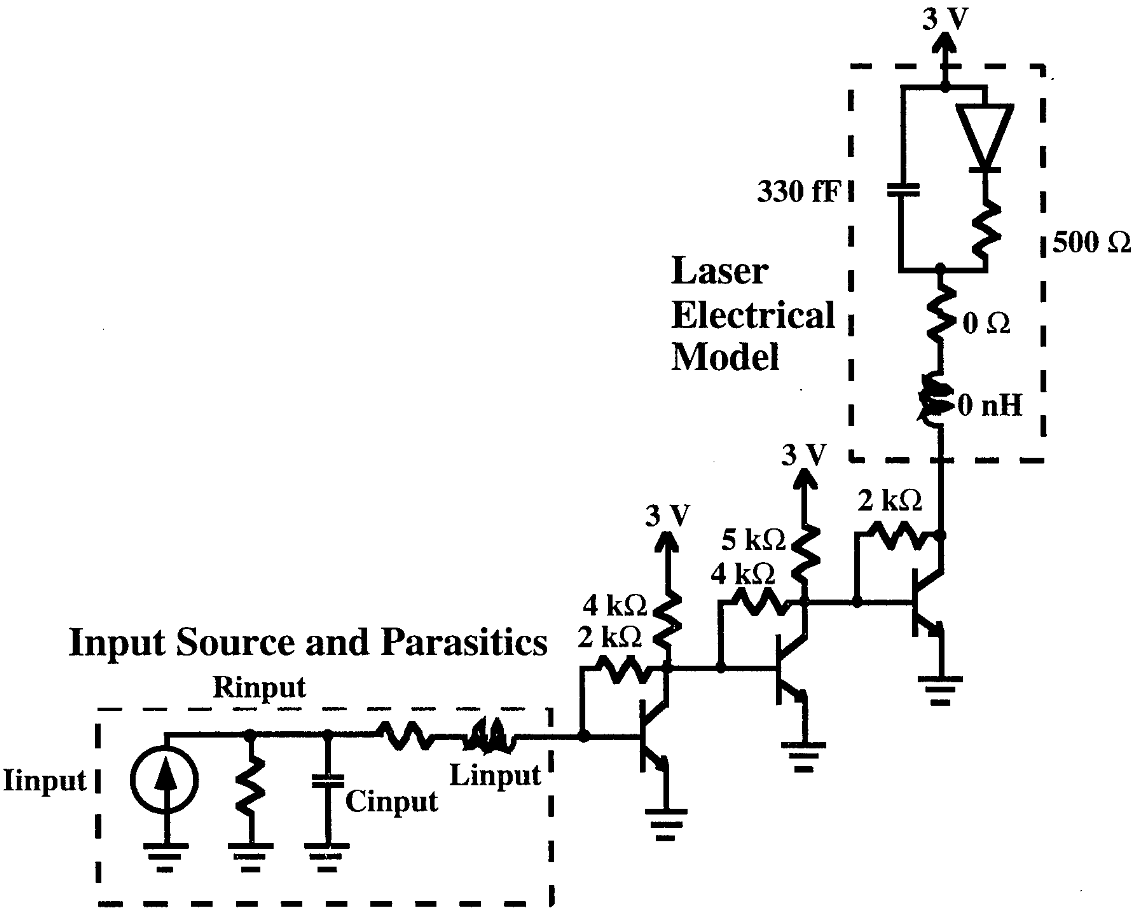

Figure APP.4.1: Three stage common emitter HBT laser driver circuit used in the link simulation. The circuit is used to drive a 270 μA threshold VCL and has a current gain of approximately 20 A/A.

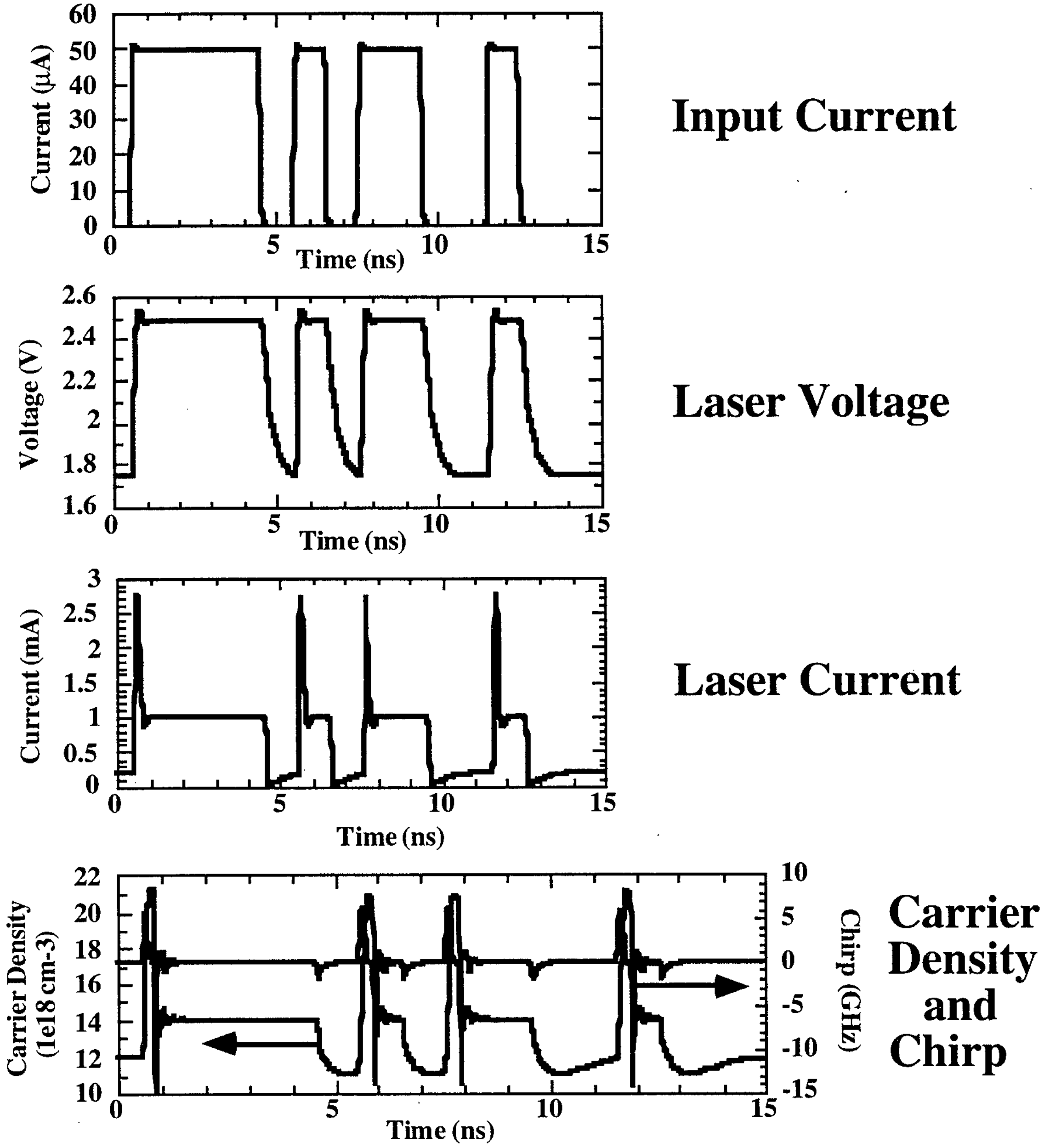

Figure APP.4.2a: Waveforms of the input current, laser current, laser voltage, carrier density, and laser chirp of a fiber link operating at 1 Gbit/s. The link consists of a three stage common emitter HBT laser driver circuit, 270 μA threshold VCL, 2 km of graded index fiber, small area pin photodetector, and receiver filter at .7 times the bit rate.

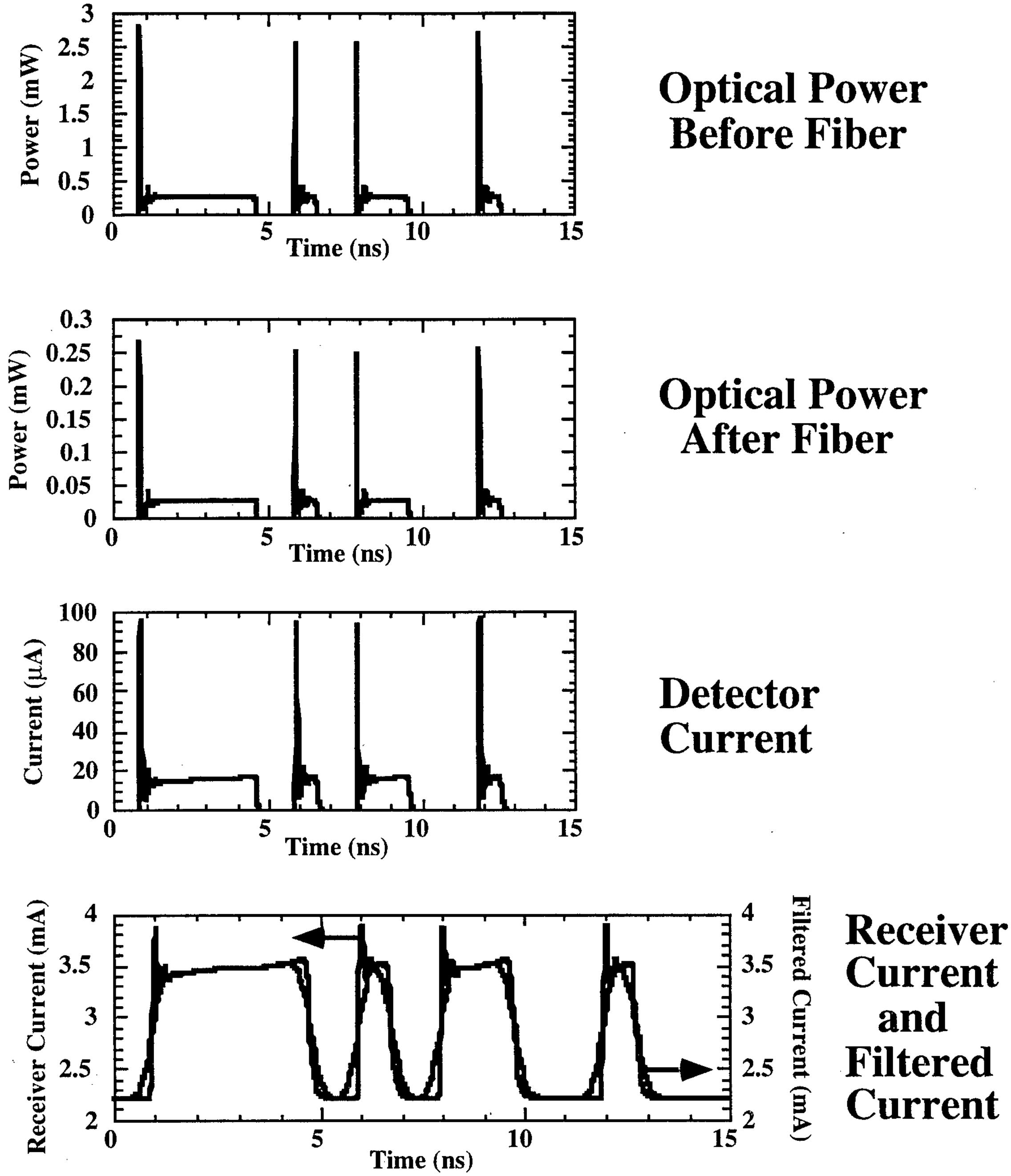

Figure APP.4.2b: Waveforms of the optical power before the fiber, optical power after the fiber, detector current, and filtered current of a fiber link operating at 1 Gbit/s. The link consists of a three stage common emitter HBT laser driver circuit, 270 μA threshold VCL, 1 km of graded index fiber, small area pin photodetector, and receiver filter at .7 times the bit rate.

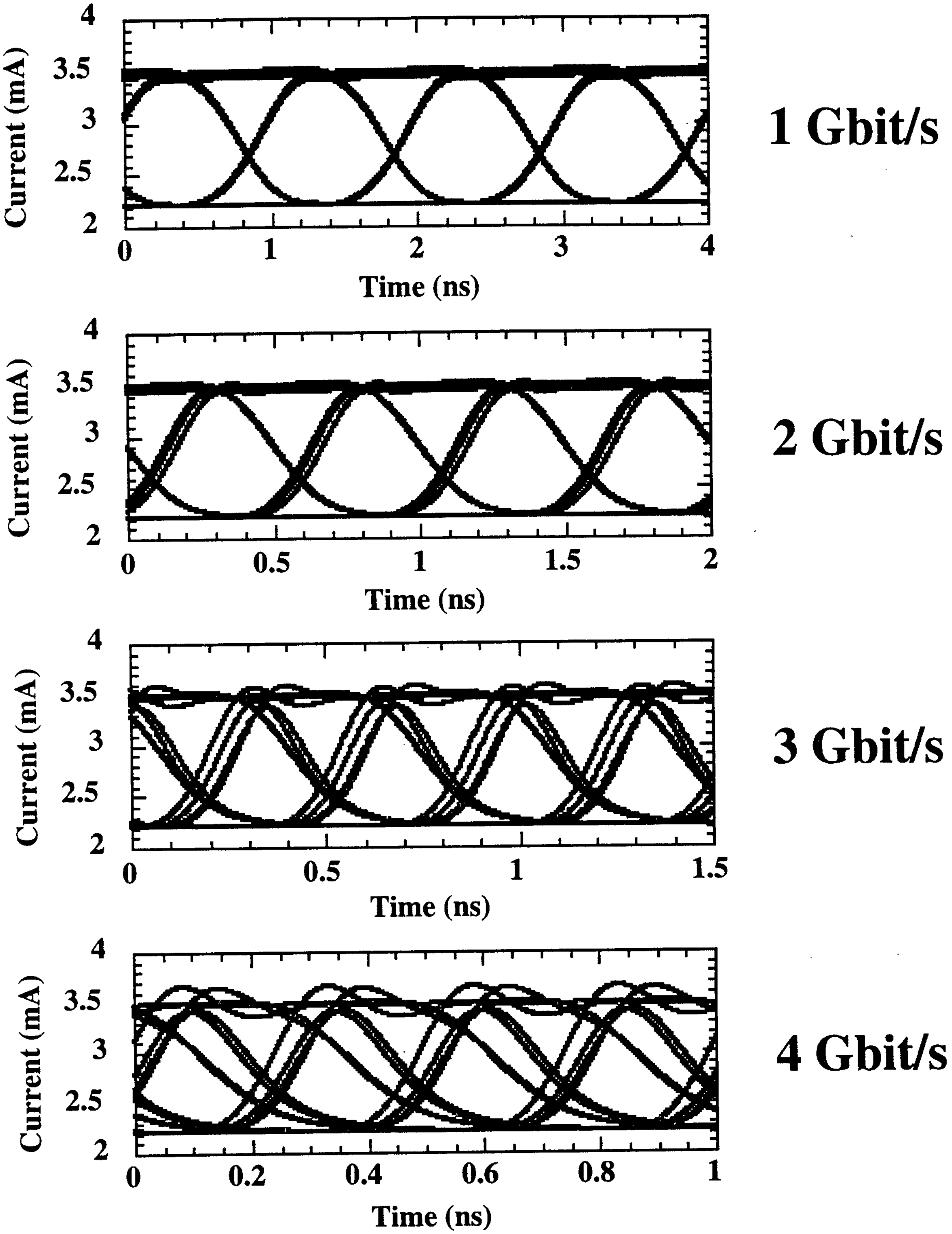

Figure APP.4.3: Eye diagrams of the output at 1, 2, 3, and 4 Gbit/s of a link consisting of three stage common emitter HBT laser driver and receiver circuits, 270 μA threshold VCL, 2 km of graded index fiber, small area pin photodetector, and receiver filter at .7 times the bit rate.

E. List of Publications Partially Supported by AFOSR

1 "Integration of Vertical-cavity Laser Diodes with Refractive Microlenses," . E.M. Strzelecka, G.D. Robinson, M.G. Peters, and LA. Coldren, *CLEO '95*, paper no. CWF14, Baltimore, MD, (May 22-26, 1995).

2. "Monolithic Integration of Vertical-Cavity Laser Diodes with Refractive GaAs Microlenses," E.M. Strzelecka, G.D. Robinson, M.G. Peters, F.H. Peters, and L.A. Coldren, *Electronics Letts.*, **31**, (9), 724-725, (April 27, 1995).

3. "Monolithic Integration of Refractive Lenses with Vertical-Cavity Lasers for Optical Interconnections," E. Strzelecka, G.D. Robinson, M.G. Peters, B.J. Thibeault, G. Thompson, L.A. Coldren, *SPIE Photonics West '96*, paper no. 2691-07, San Jose, CA, (January 27 - February 2, 1996).

4. "Multiple-Wavelength MBE-Regrown Vertical-Cavity Laser Arrays Integrated with Refractive Microlenses for Optical Interconnections," E.M. Strzelecka, T. Wipiejewski, J. Ko, B.J. Thibeault, and L.A. Coldren, *15th IEEE Internat'l Semiconductor Laser Conf.*, paper no. P5, Haifa, Israel (October 13-18, 1996).

5. "Monolithic Integration of an Array of Multiple-Wavelength Vertical-Cavity Lasers with a Refractive Microlens for Optical Interconnections," E.M. Strzelecka, T. Wipiejewski, J. Ko, B.J. Thibeault, and L.A. Coldren, *LEOS '96*, paper no. ThA2, Boston, MA, (November 18-21, 1996).

6. "Fabrication of Refractive Microlenses in Semiconductors by Mask Shape Transfer in Reactive Ion Etching," E.M. Strzelecka, G.D. Robinson, L.A. Coldren and E.L. Hu, *MNE '96*, Glasgow, Scotland, (September 23 - 25, 1996).